UNIVERSITÉ DE MONTRÉAL

HETEROJUNCTIONS OF CARBON NANOTUBES AND SILVER NANOCLUSTERS : A FIRST PRINCIPLES STUDY

NICOLAS ANTON DUCHÊNE
DÉPARTEMENT DE GÉNIE PHYSIQUE
ÉCOLE POLYTECHNIQUE DE MONTRÉAL

MÉMOIRE PRÉSENTÉ EN VUE DE L'OBTENTION
DU DIPLÔME DE MAÎTRISE ÈS SCIENCES APPLIQUÉES
MAI 2019

UNIVERSITÉ DE MONTRÉAL

ÉCOLE POLYTECHNIQUE DE MONTRÉAL

Ce mémoire intitulé :

HETEROJUNCTIONS OF CARBON NANOTUBES AND SILVER NANOCLUSTERS : A FIRST PRINCIPLES STUDY

présenté par : DUCHÊNE Nicolas Anton
en vue de l'obtention du diplôme de : Maîtrise ès sciences appliquées
a été dûment accepté par le jury d'examen constitué de :

M. MÉNARD David, Ph. D., président
M. ROCHEFORT Alain, Ph. D., membre et directeur de recherche
M. DESJARDINS Patrick, Ph. D., membre

ACKNOWLEDGMENTS

I would first like to thank my director, Alain Rochefort, for patiently guiding me throughout this process. His good humour, kindness, and well-earned wisdom have, in my mind, helped me become a better scientist. I would also like to thank the SIESTA developers for their program's production and its open-source distribution. The SIESTA user community has also been very helpful. To Daniel Stubbs and Ali Kerrache from ComputeCanada, thank you so much for answering my questions on how to best compile and run my code, and for compiling the versions that eluded me. Finally, many thanks to all of those close to me, family and friends, who helped me deal with the ups and downs of the research process. The support I have received from within, as well as outside, the lab was paramount for the production of this thesis. I've fully appreciated this opportunity, and find it is a privilege to graduate from this wonderful engineering school.

RÉSUMÉ

Les nanotubes de carbone, nanostructures aux propriétés électroniques, mécaniques, et optiques attrayantes, ont été lors de ce dernier quart de siècle le sujet de nombreuses études scientifiques et ont su démontrer des applications plus que variées. En électronique, ils ont été utilisés en outre comme senseurs grâce à leur fonctionnalisation avec des nanoparticules métalliques. Il s'avère que la quantité de particules métalliques se fixant sur la paroi de nanotubes de carbone ait un effet sur les performances des senseurs ainsi fabriqués.

Les questions se posent :
En quoi la taille d'une particule métallique peut changer son interaction avec un nanotube de carbone ? Quels sont les répercussions de la taille de la particule sur le fonctionnement d'un senseur ?

Afin de répondre à ces questions, la présente étude porte sur le calcul *ab initio*, au moyen de la théorie de la fonctionnelle de la densité (DFT), de la structure électronique de complexes composés de nanotubes de carbone (CNT) et de nanoparticules (NC) métalliques. Étant donné que peu d'études portent sur la structure électronique de complexes AgNC/CNT, nous avons choisis de nous concentrer sur ceux-ci. De plus ces particules sont parmi les plus utilisées dans les applications de senseurs à base de CNT. D'autre part, peu de travaux théoriques portent sur l'effet de taille de nanoparticules métalliques sur les propriétés électroniques de leur interface avec un nanotube de carbone. Ces travaux se démarquent d'autant plus de précédentes études par le soin porté dans la paramétrisation des modèles atomiques utilisés. Finalement, afin d'étudier comment les interfaces peuvent être affectées par une perturbation appliquée aux nanoparticules métalliques, nous considérons l'adsorption du monoxyde de carbone sur ces-dernières. Les buts de l'étude sont donc de comprendre les effets de la taille d'une nanoparticule d'argent sur son interaction avec un nanotube de carbone, ainsi que sur l'impact de la présence du CO sur les complexes AgNC/CNT.

Deux types de nanotubes de carbone ont été considérés : un nanotube métallique de chiralité (5,5) et un nanotube semiconducteur de chiralité (10,0). Les effets de taille des nanoparticules d'argent ont été étudiés en considérant des nanoparticules icosahédriques, de haute symétrie, afin de séparer les effets de taille des effets géométriques éventuels. Des particules d'argent de 4, 13, 55, et 147 atomes d'argent ont été considérées, ainsi qu'une surfaces d'argent (111) servant de référence.

L'effet de la taille des nanoparticules se manifeste déjà dans le cas des particules d'argent isolées. La quantité de charge électronique par atome de surface augmente jusqu'à atteindre

un palier pour les nanoparticules de 55 et de 147 atomes d'argent. En ce qui concerne les complexes AgNC/CNT, la taille des cellules unitaires a été optimisée sous la contrainte de maximiser le transfert de charge ayant lieu entre les nanoparticules d'argent et les nanotubes de carbone. La taille nécéssaire de la cellule unitaire pour effectivement isoler une particule métallique de son image périodique s'est avérée nettement plus grande que les tailles considérées dans de précédentes études. Les effets de taille des nanoparticules d'argent ont abordés en observant les variations du transfert de charge électronique, de l'énergie d'adsorption, et d'une description détaillée du charactère chimique de la liaison. Ces effets de taille se traduisent par une transition d'une interaction forte entre les petites particules (Ag_4 et Ag_{13}) et les nanotubes vers une interaction plus faible avec les plus grosses particules (Ag_{55} et Ag_{147}). La quantité de charge électronique en excès sur le nanotube de carbone décroît de façon exponentielle de part et d'autre de l'interface avec la nanoparticule métallique. La portée de l'injection de charge le long du tube est plus courte dans le cas des complexes Ag_{13}/CNT que pour les complexes Ag_{55}/CNT et Ag_{147}/CNT. Des états de gap induits ont été observées dans les systèmes composés de nanotubes semiconducteurs. Les positions énergétiques de ces états induits dans la bande interdite, ainsi que leur portée le long du tube, changent selon la particule adsorbée.

Des effets de taille ont aussi été observés quant à l'adsorption du CO sur les nanoparticules d'argent isolées. Le transfert de charge entre le CO et la particule, ainsi que l'énergie d'adsorption calculée du CO, décroient linéairement en fonction de la taille des nanoparticules. L'adsorption du CO a été étudiée pour les complexes Ag_{13}/CNT et Ag_{55}/CNT. Plusieurs sites d'adsorption ont été considérés sur les particules d'argent. Peu importe le site considéré, l'adsorption de CO entraîne une modification marquée de l'énergie d'adsorption des nanoparticules aux nanotubes, du transfert de charge et du dipôle induit à l'interface. Ces résulats suggèrent que les nanoparticules deviennent plus mobiles sur la surface du nanotube, ce qui contribue à l'agglomération des nanoparticules et donc à la détérioration du senseur par une perte de surface efficace.

En résumé, ces résultats théoriques confirment que la taille des nanoparticules d'argent influence leur interaction avec des nanotubes de carbone. Bien que ces effets restent présents quand de tels complexes sont utilisés en tant que senseur, l'effet de l'adsorption de CO contribue à la déterioration du senseur peu importe la taille de la particule. Ceci motive la recherche de moyens pour mieux fixer les nanoparticules d'argent au nanotube de carbone dans le but de produire des senseurs plus performants.

ABSTRACT

Carbon nanotubes (CNTs) have garnered much interest in the past quarter century due to their excellent electronic, mechanical, and optical properties. Diverse applications have been developped using carbon nanotubes. For example, in electronics, they have been functionalized with metallic nanoclusters to be used as sensors. Interestingly, the performance of such sensors depends on the quantity of nanoclusters that are applied the CNT surface.
This leads us to the following questions:
How does metallic nanocluster size affect their interaction with carbon nanotubes? What are the repercussions of these size effects on the performance of a sensor?

To answer these questions, the present work revolves around the *first-principles* calculation, using density functional theory (DFT), of the electronic structure of carbon nanotube and metallic nanoclusters. Given that few studies exist on the interaction of silver nanoparticles and carbon nanotubes, we have chosen the former as to complete the current scientific literature. Furthermore, to the authors knowledge there are no studies on the size effects of silver nanoclusters on the electronic properties of their interface with CNTs. This work further sets itself apart in the care taken in parametrizing the atomic model parameters used. Finally, as to answer the second question, we have chosen to study the effect of the adsorption of carbon monoxide. The goals of this work are to elucidate the silver nanocluster size effects on their interaction with a carbon nanotube, as well as their impact on the sensitivity of a AgNC/CNT sensing unit to CO.

Two types of carbon nanotubes have been considered: a metallic CNT of chirality (5,5) and a semiconducting CNT of chirality (10,0). The size effects of the silver nanoclusters have been studied by considering icosahedral clusters, as to separate size effects from eventual effects due to cluster geometry. Clusters of 4, 13, 55, and 147 silver atoms have been considered, as well as (111) silver surfaces that have been used as a reference point.

Size effects are already present when observing isolated silver nanlcusters; the quantity of electronic charge per surface atom grows until a plateau is reached for nanoclusters of 55 and 147 silver atoms. to properly isolate the interface of a given nanocluster with a CNT we have optimized the unit cell length under the constraint that the charge transfer between nanocluster and CNT be maximized. The necessary unit cell size was found to be significantly larger than those used in previous works in the literature. Size effects on the complexes electronic structure were studied through the calculated charge transfer, adsorption energy, and chemical bond characteristics defined by cluster-CNT interaction. Size effects translate

to a transition from a strong interaction between system constituents in the case of small nanoclusters (Ag_4 et Ag_{13}) to a weak interaction in the case of large clusters (Ag_{55} et Ag_{147}). The quantity of electronic charge on the CNT exponentially decreases away from its interface with the silver nanocluster. The decay length is shorter in the case of Ag_{13}/CNT complexes than for Ag_{55}/CNT and Ag_{147}/CNT complexes. Metal induced gap states appear in the (10,0)-CNT bandgap. The position of these states in the bandgap, as well as their decay into the nanotube, depend on the nanoclusters' size.

Size effects have also been observed with the adsorption of CO on the isolated clusters. The charge transfer, as well as the adsorption energy, linearly decrease with respect to particle size. The adsorption of CO has been studied in the case of the Ag_{13}/CNT and Ag_{55}/CNT complexes. Many adsorption sites have been considered in both cases. The result, no matter the cluster size, is a clear modification of the adsorption energy, charge transfer, and induced dipole moment at the interface. This leads to nanoparticles being more mobile on the CNT surface, resulting in sensor degradation due to reduced effective surface resulting from silver nanocluster agglomeration.

In summary, these theoretical results confirm that the size of the silver nanoclusters influence their interaction with carbon nanotubes. Even though such effects are still present when these complexes are used as sensors, the effect of CO adsorption contributes to the deterioration of sensor performance for all cluster sizes studied. This justifies further research in methods to better fix metal nanoclusters to CNTs for improved sensing performance.

TABLE OF CONTENTS

LIST OF TABLES

LIST OF FIGURES

LIST OF SYMBOLS AND ABBREVIATIONS

CNT	Carbon NanoTube
AgNC	Ag Nanocluster
DOS	Density Of States
PDOS	Projected Density Of States
FL	Fermi Level
HOMO	Highest Occupied Molecular Orbital
CNL	Charge Neutrality Level
CBM	Conduction Band Minimum

LIST OF APPENDICES

CHAPTER 1 INTRODUCTION

1.1 Research context

We are presently surrounded by an increasing plethora of sensors, activators, computers, and other connected devices. Whether they are consumer-grade, industrial-grade or research-grade, reliable methods to scrutinize our environment are ubiquitous. The miniaturization of computer electronics allow us to cram even more processing capability onto small surface areas or volumes. Carbon nanotubes (CNTs) have kept scientists dreaming about the new frontier of 1D electronics [8]. Due to their interesting thermal, mechanical, electrical, and optical properties, CNTs are found in many applications.

What are CNTs? They are a rolled-up graphene sheet. What is a graphene sheet? It is a mono-atomic layer of carbon atoms arranged into a hexagonal lattice with two sub-lattices, as portrayed in Figure 1.1a. How does one roll up graphene? Figure 1.1b shows one example. Here, the chiral vectors allow us to describe the rolling operation by taking note of the lattice displacement of an atom on the edge of a graphene sheet.

CNTs can now be produced straightforwardly [9], and many methods exist for their fabrication. They have excellent transport properties at low temperatures, are robust, and are chemically stable. They have been used in field effect transistors [10], nano-electromechanical systems [11], transparent conductors [12], sensors [13, 14, 15, 16], spintronics [17], energy storage [18], as well as interconnects for sub-22 nm technology [19, 20, 21]. Most of these applications require CNTs to interface to other components. The use of composites with CNTs spans many applications. CNTs can be mixed into pastes to improve their thermal conductivity, increasing the thermal coupling of microprocessors to their heat-sinks. Mixing CNTs into polymers lead to mixed phase systems with augmented electro-mechanical properties. Thin films of CNT mats combined with metallic nanoparticles lead to flexible electronics that can even be transparent if the density of CNTs in the mat is kept under a certain threshold [22, 23, 12, 24, 25, 26]. CNT-based sensors have been theorized and manufactured. In all cases, the conceptual underpinning of these technologies is the interface: bringing together two well-defined materials to achieve a sum greater than its parts.

The main setback in fabricating sensors with CNTs is one of their advantages: their chemical stability. This robustness means that CNTs interact quite weakly with their environment. To circumvent this issue, it is necessary to combine the CNTs with more reactive elements, such as metallic nanoclusters (MNC). There are many approaches to the fabrication of CNT/NC

composites, which can be separated in two main methodologies where the nanoclusters either directly aggregate on the CNT wall or are selectively deposited on chemically modified CNTs [27]. A major difficulty is to understand how the atomistic details on sensor function scales up to device scale.

1.2 Elements of the problematic

The subject of the present work revolves around the use of CNTs as sensors. Different metals have been used with CNTs to improve their sensitivity and transport performance towards various molecules. Noble metals are particularly interesting because of their stability in small cluster form [2].

Unfortunately, functionalizing a CNT with a metal is very difficult to control [15]. The metal cluster size plays an important role in the properties of the resulting composite, although the CNT diameter may play a rather large role as well [28].

A few theoretical works have been done on the the quantum size effect on the interface between the CNT and NC; only small clusters have been considered. It is of interest to understand the electronic properties of interfaces comprised of larger NCs, because in real systems deposited metal particles will coalesce into larger clusters [15].

Furthermore, most studies reported in the literature are related to interfaces with Au-NCs [29, 16, 30]. In the present study, we will bridge the gap in knowledge by modelling the interface between AgNC and CNT.

1.3 Research objectives

The objectives of the present research are to answer whether or not the electronic structure of AgNC/CNT systems is influenced by the size of the AgNC, and to investigate what effect CO's adsorption onto the cluster may have on the complex. To quantify the effect of the AgNC size, we will evaluate:

- charge transfer to the CNT,
- bonding characteristics between the CNT and the cluster,
- charge distribution and rearrangement along the CNT.

A similar analysis will be performed in the case of CO adsorption, as to describe the change in system characteristics between a pristine system and one that is in contact with a CO molecule. The influence of the CO adsorption site will also be considered.

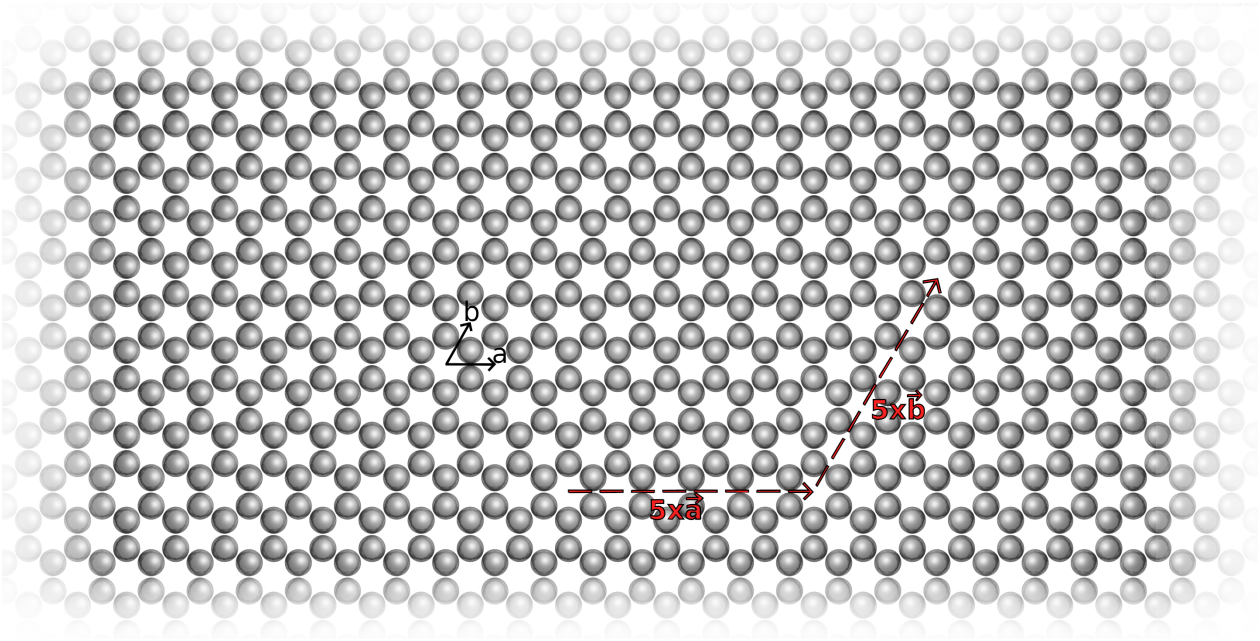

(a)

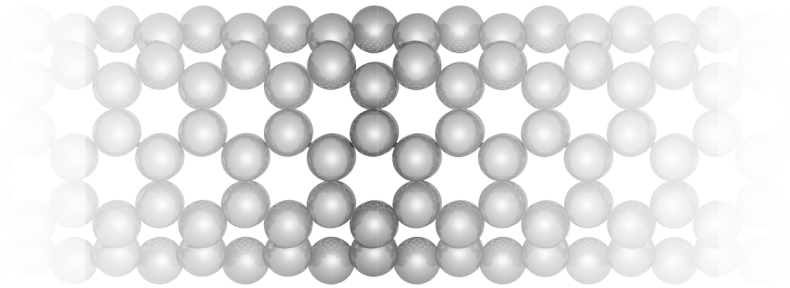

(b)

Figure 1.1 Graphene's geometry (a) and resulting (5,5)-CNT (b) after rolling following dotted red lines

1.4 Proposed methodology

Density functional theory (DFT) is a computational method that relies on the transformation of the many-body electron problem to a one electron theory in an effective medium. Although some many-body effects can not be accounted for with such an approach, simpler properties such as charge density and electronic structure near Fermi level can be precisely simulated. This is due to the method being based on quantum mechanical first principles.

SIESTA is an open-source linear combination of atomic orbitals (LCAO) implementation of DFT. The advantage of such an implementation is that it is computationally less demanding than a plane wave approach. It is however more difficult to properly describe the system from the get go, because the basis set needs to be chosen. Of course SIESTA does provide an automatic way to generate these, but the it is somewhat limited, and the necessary properties need to be converged with respect to the basis set. A poorly chosen basis set results in a limited description of the physics of the system. The particularity of SIESTA is that it is possible to calculate electronic properties of periodic systems, which is generally not the case for standard LCAO methods. This will allow us to avoid finite size effects in the systems that we will study, with the downside that extra input parameters need to be converged with respect to interesting properties. SIESTA has the potential of providing a computationally efficient approach to the questions that motivate the present work, however more work needs to be provided up front due to convergence issues.

We will use this method to look into the atomistic details of the AgNC/CNT interfaces, as well as their modification on adsorption of CO. Given that size effects are the main interest, we will focus on a specific cluster geometry to isolate size effects from those due to shape and structure. AgNCs have been shown to present icosahedral geometries under 300 Ag atoms [2], so we will focus on such a range of cluster sizes since the DFT method rapidly becomes too computationally demanding for large systems.

We will have to properly set up the calculations so that the interesting properties, namely charge transfer and distribution, are properly converged. This means that a first step will be to parametrize the simulation in such a way that proper accuracy is reached without an overwhelming use of computational resources.

1.5 Thesis structure

First, we will survey the scientific literature regarding CNTs, noble metal clusters, and mixtures of the two. This literature review will present state of the art results in this field.

Second, we will detail the specifics of DFT and its implementation in SIESTA within the methodology section. This second section will also present the details of the convergence studies and the parametrization of the systems.

Third, we will present the results and analyze them. We will start with the isolated components, follow with the combined AgNC/CNT systems, and complete the study with the results of the CO/AgNC/CNT systems.

Finally, a conclusion will synthesize the results, present some limitations, and propose possible future works to continue the present study.

CHAPTER 2 LITERATURE REVIEW

The following literature review first spans through some of the properties of carbon nanotubes (CNT) and of metallic nanoclusters (MNC), and ends with the properties of interfaces and their application in gas sensing in hybrid networks of CNTs and MNCs. Due to the extensive existing literature on these matters, a selective but representative sample will be presented.

2.1 Isolated components

2.1.1 The carbon nanotube

The final quarter of the XXth century saw increasing theoretical and experimental inquiries upon 1D physical systems; Iijima *et al.*'s explicit discovery [31] of CNTs was a boon for all, markingly increasing further work on graphitic materials. Since then, carbon nanotubes have been extensively studied, and potential applications outlined for the inclusion of this new wonder-material in many devices. CNTs possess a myriad of valuable properties: mechanical robustness, electronic character flexibility, opto-electronic capacity, field emission behaviour, among others [32]. In the context of this work, however, we will focus on the electronic structure; electronic structure arguably supports all further exotic properties that have been reported.

The electronic structure of a CNT is entirely dependant on its geometry. Once again, a simple way to describe a CNT is to conceptually roll a graphene layer into a cylinder, as seen in Figure 1.1b of the introduction. The chiral vector describes how the sheet is rolled up, and is the only piece of information needed to completely describe a CNT's electronic structure. The classic description of a CNT follows the idea of rolling a graphene sheet: its band diagram is calculated via the zone-folding approximation. It comes down to constraining graphene's dispersion relation $E(\boldsymbol{k})$ to the *k-lines* allowed by the periodic condition along the tube circumference: $\boldsymbol{k} \cdot \boldsymbol{C}_h = 2\pi m$, where m is an integer [4, 33]. As such, each tube's electronic structure samples graphene's with a unique set of k-lines, which is schematically shown in Figure 2.1.

This readily explains the well-known result that a nanotube is metallic if the difference of the chiral indices is a multiple of 3 [34, 3, 4, 32, 33]; considering graphene's K point $\boldsymbol{K} = 1/3(\boldsymbol{k}_1 - \boldsymbol{k}_2)$, one finds that [33]:

$$\boldsymbol{K} \cdot \boldsymbol{C}_h = 2\pi m = \frac{1}{3}(\boldsymbol{b_1} - \boldsymbol{b_2})(n_1\boldsymbol{a_1} + n_2\boldsymbol{a_2}) = \frac{2\pi}{3}(n_1 - n_2)$$

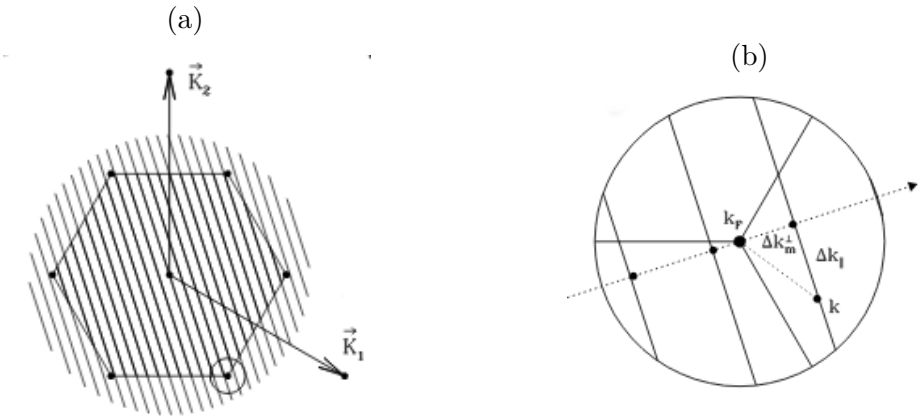

Figure 2.1 (a) The allowed k-lines in the first Brillouin zone of graphene for a (13,6) CNT and (b) expanded depiction near E_F
Reprint with permission from [3]. Copyright (1998) by the American Physical Society

Pristine CNTs

Being one dimensional systems, CNTs of all electronic characters are easily identifiable through their DOS, riddled with sharp van Hove singularities [35, 34, 3]. These "spikes", as seen in Figure 2.2a for a metallic (5,5) CNT, are a manifestation of the confinement properties in directions perpendicular to the tube axis. The position of these singularities can be determined by analyzing the dispersion relations that lead to band diagrams, which is visually apparent as the former coincide with flat portions of the bands along the high symmetry axis $X - \Gamma - X$.

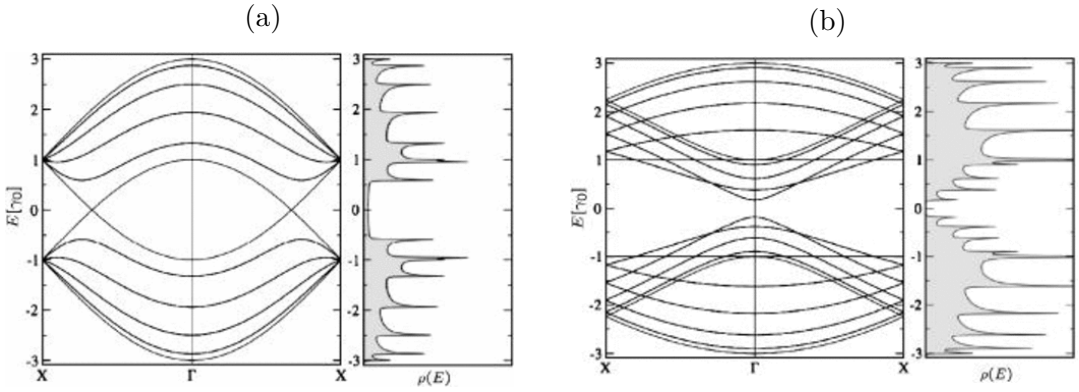

Figure 2.2 Band structure and DOS of (a) (5,5) and (b) (10,10) CNT within the zone-folding approximation. Reprint with permission from [4]. Copyright (2007) by the American Physical Society

Starting with the statistically dominant semiconducting CNT, the band diagram and DOS

show a small bandgap, as seen in the case of the (10,0) zigzag nanotube in Figure 2.2b. The band-gap of semiconducting nanotubes appears to decrease as the inverse of the tube diameter d_t ($d_t = |\boldsymbol{C}_h|/\pi$) [4]. This diameter-dependant relationship has been experimentally confirmed using scanning tunnelling spectroscopy (STS), as has the the approximate 2/3 ratio of the semiconducting type among usual CNT populations [36, 37]. However, this inverse relation relies on the assumption of linear dispersion around the Fermi energy [3]. This approximation fails further from the Fermi level (FL), due to the trigonal warping effect in which the equi-energy contours (in graphene's BZ around a K point) change from a circle to a triangular shape with increasing energy [38]; the trend, however, still exists.

Predictions stemming from the zone folding (ZF) approach prove relatively good for general trends, but failure to take into account the curvature of the tube results in erroneous predictions for CNTs with diameters smaller than 5 Å. For this reason, the (5,0) CNT is a conductor even though $n_1 - n_2$ is not a multiple of 3 [39]. In fact, the zone folding approach only reliably predicts electronic properties for tubes larger than 1 nm, and only near the Fermi energy [4].

These shortcomings can be overcome by using different approaches. For example, Damnjanović *et al.* have proposed a method relying on group theory, effectively capturing some of the effects of CNT curvature on the electronic structure through its line group symmetries. This method is more abstract but is faster, all the while giving more physical insight than the ZF approach [40]. This approach has effectively predicted so-called secondary gaps in metallic chiral CNTs, resulting in only the armchair tubes being correctly predicted as metallic by the ZF approach [41]. The group theoretical approach is efficient when considering the physics of isolated tubes but the interactions of a CNT with its environment renders the method too complex when considering more realistic structures and devices.

The Density Functional Theory (DFT) method, coupled with geometry optimization algorithms have also shown that the electronic structure of a CNT can be greatly affected when considering smaller diameters, while the CNT structure asymptotically approaches that of graphene with increasing diameter [42]. Smaller diameter CNTs are also subject to rehybridization of the σ and π states, which has also been found through early DFT calculations [43, 39]. These effects of dimensionality on the band gap value of CNTs are summarized in Figure 2.3 [5]. It is clear that properties of CNTs with small radii should be considered through DFT simulations [5, 44] or group-theoretical methods [40], while other methods can be used to account for the properties of larger tubes. However, approximate numerical approaches are obviously limited when considering realistic systems; properly understanding the electronic properties of CNTs in such situations is an arduous process, needing the combined efforts of experimentalists and theoreticians.

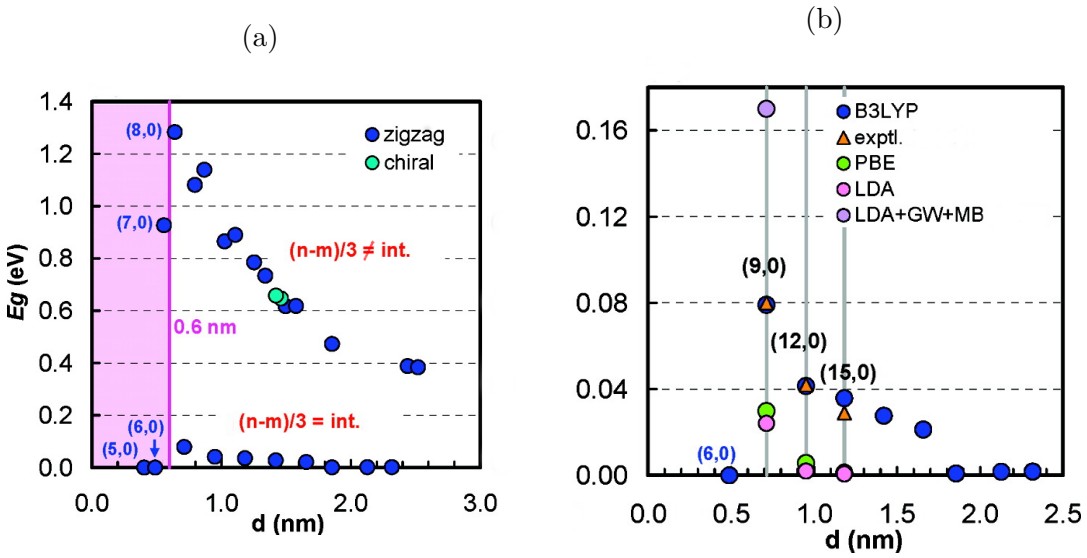

Figure 2.3 Variation of the band gaps of (a) zigzag and chiral SWNTs and (b) metallic zigzag (3m,0) SWNTs as a function of diameter. Adapted with permission from [5]. Copyright © American Chemical Society

2.1.2 Noble metal nanoclusters

In general, the properties of bulk metallic materials can be completely different at the nanoscale; the continuous band dispersion of periodic crystal structures gives way to discrete energy levels for small particles [45, 46, 47]. In fact, thinking about metallic clusters starts by breaking periodicity along one direction with the introduction of surfaces. Cleaving an infinite bulk metal into two semi-infinite parts has been thoroughly studied in the setting of the jellium model; it leads to charge spillage from the surface, as well as standing waves known as Friedel oscillations [48]. Surface energies arise as the concerted contribution of the surface energy in the uniform background model, the electrostatic cleavage energy and the electrostatic energy due to charge spill-out. The work function (Φ) is the minimum energy needed to promote an electron from FL (E_F), at 0 K in the metal, to the vacuum level [49]:

$$\Phi = \Delta\phi - \bar{\mu}$$

where $\Delta\phi$ is the change in electrostatic potential created by the surface dipole layer, and $\bar{\mu}$ is the chemical potential of electrons in the metal. At nanoscopic dimensions, the value of the chemical potential takes the form of [50]:

$$\mu = \left.\frac{\partial E}{\partial N}\right)_v$$

The variation in the energy (E) with respect to the number of electrons (N) is sensitive to the available amount of electrons in the many-body system; removing an electron from a Fermi sea of electrons is quite different than to remove one electron from a molecule. In the context of molecular electronics, the work function (or the electron affinity) of a metal cluster is replaced by the gap between HOMO and LUMO levels. The latter give a first approximation of the ionization potential and the electron affinity of a metal cluster by virtue of Koopman's theorem [51].

Trends for noble MNCs: electronic and structural properties

In the case of metal clusters, simple models to describe their electronic structure built from bottom up have been astoundingly effective to relate experimental data for simple monovalent MNCs [51]. The spherical jellium model is such a simple model. This approach is similar to the uniform potential background used to describe a bulk metal surface, with the difference that it is here a spherical potential well that holds the electrons within the cluster. This approach takes into account the MNC finite size.

Other important considerations are electron-electron interactions and the exchange and correlation energy. Yamaguchi *et al.* included such effects in first-principle DV-Xα calculations concerning icosahedral Ag_{13} and Cu_{13} NCs [52], and showed that effective one-electron calculations like the spherical jellium model hold up well in terms of geometry and electronic structure. The self-consistent DFT formulation of a MNC allows the inclusion of electron-electron interactions as well as exchange and correlation energy approximations.

There are two types molecular orbitals in noble MNCs [52, 53]; the first type is formed by n-d orbitals, with $n = 3$ for Cu, $n = 4$ for Ag, and $n = 5$ for Au. The second type is a hybridization of $n + 1$-s and $n + 1$-p orbitals. The n-d charge is centered around atoms, while the $n + 1$-sp charge extends over the whole cluster. The charge density of electronic states near the Fermi energy is mainly located at the surface of the MNC, with a small contribution from the core atoms of the cluster. These DFT calculations are usually limited to fairly small MNCs, typically below a few hundred atoms. Tight binding models can easily scale up to thousands of atoms in practical times. For much larger clusters, semi-empirical models in conjuction with global optimization can be used to probe the configurational space [54].

Regarding the structure of the NCs, most computational methods consider highly symmetric close packed geometries as starting points in their optimizations. This has been judged in some cases as an oversimplification [55]. Many polyhedral geometries can be constructed with this approach, but we will limit ourselves to the Mackay icosahedron. In this case, the total surface energy and its surface area can be minimized when all the faces are terminated with

(111) planes. It is comprised of 20 triangular faces and of N atoms:

$$N = \frac{1}{3}(10K^3 - 15K^2 + 11K - 3) \tag{2.1}$$

where K is the number of atoms along an edge [51].

Smaller clusters share similar geometries for all three noble metals, up to $N = 5$, while for $N = 6$ results are mixed. Gold is particular in the shapes it takes, as it is the most relativistic element below Fermium. It adopts planar shapes because of the strong contraction of the outer 6s shell and a reduced 5d-4s energy gap. This leads to significant hybridization of the atomic 5d and 6s orbitals and direct d-d bonding effects which favour planar structures [56, 57]. The relativistic nature of Au manifests itself more in the geometry than in the energetics [55]. Silver and copper show features that are reminiscent of the alkali metals [2]. In the case of copper, the 3d orbitals are localized around the atoms, whereas the 4s and 4p electrons extend over the whole cluster. For $N = 13$, the most stable structures seem to be amorphous for all Cu, Ag, and Au [55]. With $N = 55$, the icosahedral geometry is preferred by Cu and Ag [58, 56, 59, 60] whilst a low symmetry structure is adopted by Au [56, 59]. The structural crossover sizes (ie the amount of atoms at which a change in the cluster structure occurs) for Cu, Ag and Au are presented in Table 2.1. The only caveat is that cuboctahedral geometry is slightly more stable than the icosahedral geometry for NCs with 147 Ag atoms [2].

Table 2.1 Crossover sizes for the noble metals [1, 2]

Metal	N(icos→deca)	N(deca→fcc)
Cu	1000	53000
Ag	<300	20000
Au	<100	500

In the following section we will focus more specifically on silver nanoclusters (AgNCs) to describe the size effects on their electronic, optical, and catalytic properties.

Size effects in silver nanoclusters

The average bond length in small noble MNCs ($N \leq 20$) increases linearly with an increasing number of atoms [61]. Fernandez *et al.* also find that the binding energy per atom increases with N, this time in a log-like fashion. The binding energy (ϵ_{at}) of larger AgNCs ($N \geq 100$) has been shown to follow a linear scaling law in [53], which is coherent with melting temperatures

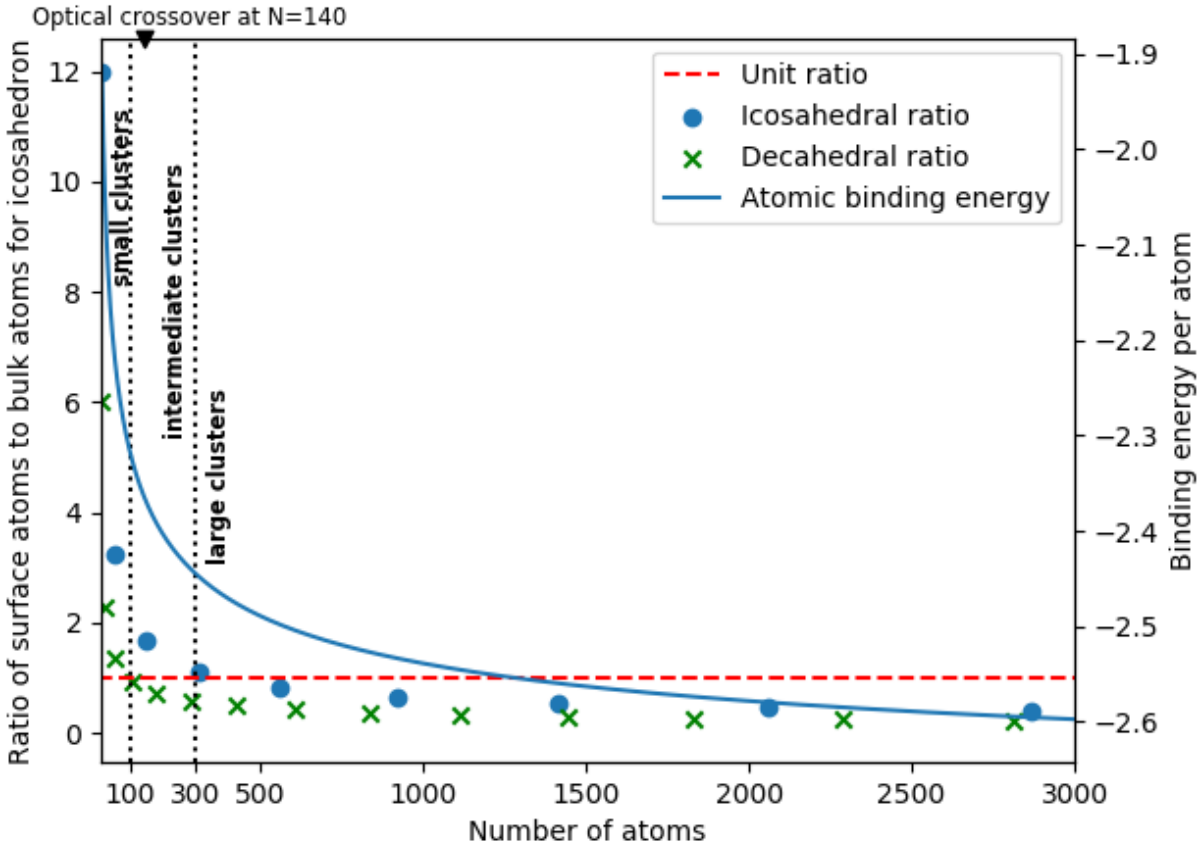

Figure 2.4 Ratio of surface atoms to bulk atoms in icosahedral clusters

growing with cluster size [51]:

$$\epsilon_{at} = a + bN^{-\frac{1}{3}}$$

where $a = -2.73$ eV and $b = 1.91$ eV. a is the constant binding energy per atom that is reached for infinite crystal dimensions, and b is the contribution due to molecular size. These authors consider that the crystal core is not present for AgNCs that are smaller than 100 atoms [53]. This scaling law is presented in Figure 2.4 along with the ratio of surface atoms to core atoms, which are 12-coordinated atoms. Here one can see that this ratio is too high for smaller clusters, as explained by Kiss *et al.*. The icosahedral ratio, represented by blue dots in Figure 2.4, is the ratio of surface atoms to core atoms for icosahedral structures. The decahedral ratio, represented by green crosses in Figure 2.4, is the ratio of surface atoms to core aroms for decahedral structures. The three MNC size ranges suggested by the authors are also shown on the figure. Each range is defined by the rate of variation of the binding energy with respect to the number of atoms in the NC. They suggest AgNCs of 150 atoms correspond to the transition point from small nanoclusters to bulk-like behaviour. This crossover point definition agrees with a suggested transition out of a quantum regime at $N \approx 140$, based on the features of the complex polarizability spectra of AgNCs [62, 63]. The trend in inter-band and intra-band optical transitions of AgNCs calculated by He *et al.* also aligns with these conclusions [64]. Furthermore they find that the size of the MNC affects the optical properties more than the shape of the cluster does.

For catalysis applications, the change in surface structure of MNCs with size (see Table 2.1) influences their reactivity. It is of primary importance to clarify the structure/reactivity relationship. This is fundamentally relevant in the case of catalysis, since the goal of molecular-scale rational design for catalyst systems requires detailed knowledge and understanding of this structure–reactivity relationship [65]. Real extended surfaces usually imply a high occurrence of surface defects and irregularities such as vacancies, adatoms, edges, and terraces that contribute to the catalytic activity [28]. Among experimental techniques to probe the structure of gas-phase clusters we find ion-mobility spectrometry [66, 67], gas-phase electron diffraction [68, 69], photoelectron detachment spectroscopy [70], and infrared multiple photon dissociation (IR-MPD) spectroscopy [65].

Additional challenges arise when MNCs are supported, because the support introduces further geometric constraints and the charge state of the NCs depends on their electronic interactions with the support. Studies on the CO oxidation on positively and negatively charged AgNCs of 13 atoms [71] indeed show that not only is the structure of the nanoclusters affected by the amount of charge added or taken from them, their energetics are changed, affecting subsequent adsorption and reactions.

In the next section, we will further elaborate on CNT-supported MNCs, after providing a theoretical description of the interfaces between different materials.

2.2 Metallic nanoclusters supported on CNTs

The characterization of interfaces has continually been investigated in cutting edge research over the past 50 years. The description of interfaces brings significant challenges, because they come in various sizes, and invariably imply the mixing of two states of matter with different physico-chemical properties. Furthermore, depending on the scope of an investigation, different phenomenological models may be used. One might argue that a selection of such models may be necessary for the complete characterization of an interface. It is thus of interest to survey the most accepted phenomenological models of interfaces involving different materials.

2.2.1 Describing an interface

In this section we will cover the vast subject of interfaces in a broad fashion. In the context of this work, only metal-metal and semiconductor-metal interfaces are involved; we will concentrate on their description. It is logical to start with extended interfaces and the corresponding phenomenological models. Such models may not be suitable for interfaces of reduced size, and so the salient features found in these interfaces will then be discussed from an atomistic perspective.

Extended interfaces

The first interface that we can describe is the one between two metals. As shown in Figure 2.5a, if two surfaces are brought together, an electrostatic interaction appears between the charge spilling out from each component. Once a contact is made, thermodynamic equilibrium requires that the Fermi levels align. Electrons leave the lower work function metal, and they move into the continuum of states of the other metal. This charge rearrangement results in an interfacial dipole created between the materials, seen schematically in Figure 2.5b. The resulting average variation of the potential from the first metal with respect to the second can be described as [72]:

$$e\Delta V_C = e(\phi_{II} - \phi_I) \tag{2.2}$$

where $\phi_I < \phi_{II}$.

This picture is similar to the Schottky-Mott model of metal-semiconductor interfaces where

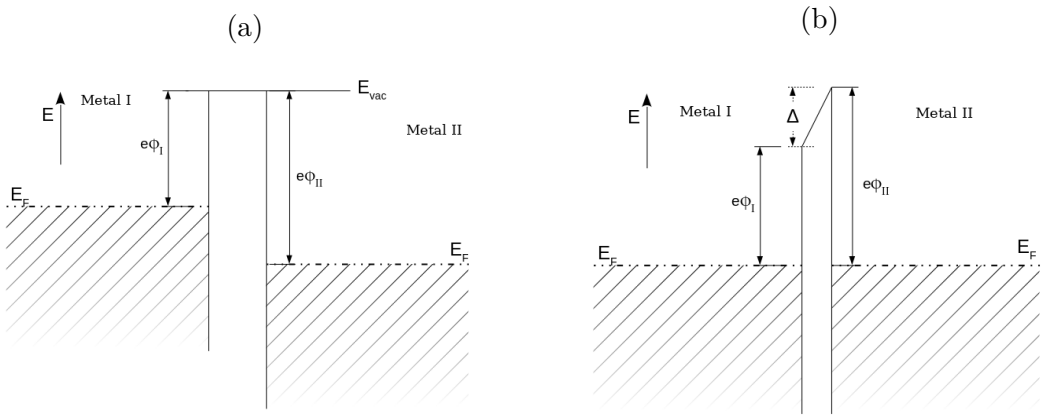

Figure 2.5 Schematic description of a metal-metal interface (a) before contact and (b) after contact

the potential barrier (Ψ_{SB}) is:

$$\Psi_{SB} = \Phi_M - \xi_{SC} \tag{2.3}$$

where Φ_M is the metal work function and ξ_{SC} is the electron affinity of the semiconductor (SC), i.e. the variation between the SC conduction band minimum (CBM) and the vacuum level as seen in Figure 2.6. This model essentially describes how the energy levels of each of the surfaces making up the interface line up, and depends on the superposition principle of electrostatic potentials [73].

The absence of the continuum of states on the SC side changes things drastically; the situation is complicated by the presence of states populating the SC bandgap. These metal induced gap states (MIGS) are metal states that decay into the SC, within the energy range where the metal conduction band overlaps with the SC bandgap [73, 74]. These evanescent states are, in essence, a mixture of SC valence and conduction band states, and the nature of such a state depends on which end of the bandgap it is energetically closest to; the crossover level at which the character of a MIGS is equally attributed to conduction and valence band states corresponds to the charge neutrality level (CNL) [74]. The CNL depends on how electronic states rearrange themselves so that the charge neutrality condition is satisfied near the interface region. Using a more atomistic approach, Tung contends that charges populating the interface region are due to chemical bonding [73].

The need to include this concept of CNL within the band line-up picture was first expressed by Bardeen in 1947, since several measured barrier heights did not apparently depend on the metal used in the junction [75, 76, 77]. The situation is shown in Figure 2.6, where the Fermi level is pinned at the CNL. The Shottky barrier (SB) becomes:

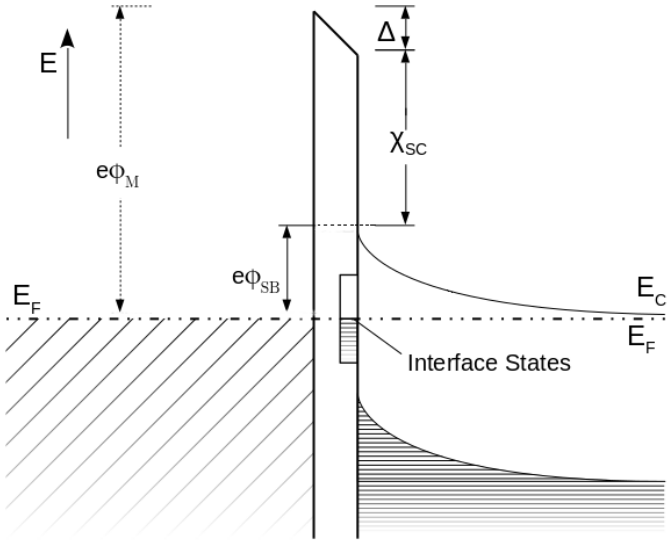

Figure 2.6 Schematic description of a metal semiconductor interface

$$\Psi_{SB}^{n} = E_C - \Phi_{CNL} \tag{2.4}$$

where E_C is the SC CBM and Φ_{CNL} is the CNL. Although Bardeen's approach was a step in the right direction, the Schottky-Mott rule still held value. Following Heine's proposal that intrinsic SC states were being populated by well-matched Bloch states from the metal [78], Cowley and Sze combined both models by introducing an interface parameter γ that depends on the density of states at the interface [79]:

$$\Psi_{SB}^{n} = \gamma(\Phi_M - \xi_{SC}) + (1-\gamma)(E_g - \Phi_{CNL}) - \Delta\Phi_n \tag{2.5}$$

Now the SB height for electrons Ψ_{SB}^{n} depends on a weighted contribution of the difference between the metal work function Φ_M and the SC electron affinity ξ_{SC} with a counter-weighted contribution due to the position of the CNL within the bandgap. $\Delta\Phi_n$ corresponds to an external potential acting on the interface electrons.

It is of interest to consider a more recent atomistic approach to define γ by Tung. Let us now briefly compare Cowley and Sze's interface parameter γ_{GS} with Tung's γ_B :

$$\gamma_{GS} = \left(1 + \frac{e^2 \delta_{gap} D_{GS}}{\epsilon_{int}}\right)^{-1} \quad \gamma_B = 1 - \frac{e^2 N_B d_{MS}}{\epsilon_{it}(E_g + \kappa)},$$

$$\kappa = 4e^2/\epsilon_S d_B - 2e^2/(\epsilon_{it} d_{MS})$$

In both cases there is a distance separating both materials, δ_{gap} and d_{MS}. The difference lies in the first being attributed to an arbitrary interfacial layer (usually of 1 nm) between the two materials, and the second being attributed to the chemical bonding distance between the two. In γ_B, the interface state density D_{GS} is replaced by a number of chemical bonds N_B. The chemical bonds in Tung's model are assumed to form in a square region of dimension $d_B = N_B^{-1/2}$. The most striking difference lies in the denominator, which Tung had developed in the spirit of the electro-chemical potential equalization method to determine the charge transfer between monolayers of the metal and the semiconductor [80]. κ is the sum of the Coulombic terms due to the charge rearrangement caused by the chemical bonds across the interface between the metal and the SC. d_{MS} is the distance between the metal atoms and the SC atoms at the interface, and ϵ_{it} is the permittivity of the interface. Finally, E_g is the gap of the SC. Essentially, one model stems from the band bending picture capturing the extent of the space charge within the SC, while the other is local at the interface.

This comparison sums up the difficulty in describing interfaces properly. There are collective effects that can make their presence felt inside the bulk, however models that consider these effects underestimate the atomic nature of the interface. Tung attempts to remediate the situation, but in doing so limits the scope to the immediate interface. Finally, we have been considering clean interfaces, while realistic interfaces are subject to intermixing of the atomic species, the presence of defects (and defect states), as well as morphological changes. In these more complex cases it is necessary to use more advanced methodologies, such as those based on first-principles.

Atomistic description of interfaces of reduced dimension

Before moving to the subject of CNT-supported MNCs, we give an overview of other relevant interfaces of reduced dimension.

The picture of graphene adsorbed on a metal slab provides a good starting point since it is reminiscent of large diameter CNTs; it would represent a limit to the trends of CNTs adsorbed on metals. Khomyakov *et al.* have theoretically studied the adsorption of graphene on different metal (111) surfaces. The authors used local and semi-local DFT approximations, noting that non-local van der Waals corrections do not significantly affect the charge distribution at the interface [81]. They found that graphene is strongly bonded (chemisorbed) to Co, Pd, and Ti, whereas it is physisorbed on Al, Cu, Ag, Au, and Pt surfaces. Chemisorption leads to

the modification of the dispersion properties of graphene , while physisorption preserves the conical dispersion around the Dirac point [82]. In both cases, oscillations of the metal charge density screen the accumulated charge at the interface from the bulk. To further explain the case of physisorption, Khomyakov *et al.* provide a model tying together the modification of the metal work function ($\Delta W(d)$) to the potential energy change due to charge transfer ($\Delta_{tr}(d)$) and the potential change due to the charge rearrangement ($\Delta_c(d)$):

$$\Delta W(d) = \Delta_{tr}(d) + \Delta_c(d) \tag{2.6}$$

By studying the physisorption of graphene with several metals, they also find that the doping threshold from n-type to p-type doping occurs at $W_M = W_G + \Delta_c(d)$, where W_G is the graphene work-function and $\Delta_c(d) = 0.9$. The charge rearrangement term $\Delta_c(d)$ has also been noted in studies on the adsorption of organic molecules on metal surfaces. For example, Crispin *et al.* show in their work that there are two contributions to the interface dipole: one is bond formation at the interface, and the other is the change in the metal work function introduced by the perturbation of the metal surface electron density due to the presence of the adsorbed organic molecules [83]. This behaviour is obvious when looking at the description of the variation of the metal work function (ΔW):

$$\Delta W = eD_{int} = eD_{chem} + e\Delta D_{met} \tag{2.7}$$

This formulation describes the modification of the interface barrier through the dipole contribution from hybridization and bond formation D_{chem}, as well as by the variation of the metal surface dipole ΔD_{met} due to the presence of the adsorbate. The latter phenomenon has also been described as a pillow effect [84, 85], and seems to be more important in the case of weak interaction between the reactants [86].

2.2.2 The interface between carbon nanotubes and metals

There are two main groups of metal/CNT contacts, side-bonding and end-bonding. A representation of the two cases is shown in Figure 2.7. In the the present work, we will limit our description to side-bonded geometries. There are two types of interface configurations for the side-bonded geometries: either a CNT is adsorbed on a metallic slab-like substrate [6, 44, 87], or it is embedded into the metal [7].

Interaction with bulk metals

The interaction of CNTs with bulk-like metals represents the asymptotic behaviour of the quantum size effects that MNC/CNT interfaces can show. Understanding such interfaces is thus important to position the magnitude of interaction in MNC/CNT systems.

Nishidate and Hasegawa have investigated the interaction of different surface orientations and metals with metallic CNTs [44, 87]. They studied the interaction of a (10,10)-CNT with (111) surfaces of Al, Cu, Ag, Au, Rh, Pd, Ir, and Pt [87]. They find that chemisorption of Rh, Pd, Ir, or Pt modifies the CNT electronic structure. In this case, the hybridization of the metal surface states and the CNT π-bands results in bond formation rather than just a charge transfer. Interestingly, in contrast to the (10,10)-CNT case, the interaction of Pt with graphene was defined as weak [82]. Here is a first manifestation of the difference between CNTs and graphene in their adsorption on metals. This difference is mostly due to the curvature of CNTs that modify the outer π-band with respect to the planar case [39, 43, 44].

On the other hand, physisorption results in a simple translation of the band structure. Following Khomyakov *et al.*'s approach [82], the rigid band principle makes it possible to easily differentiate between charge transfer and charge rearrangement. Nishidate and Hasegawa observed a similar behaviour for the case of physisorbed CNTs on (111) slabs (Al, Cu, Ag, Au). This is because the Fermi level of the CNT is not in the range of the metal d-states, implying that the CNT π-orbitals do not strongly hybridize with metal d states. This weak hybridization preserves the dispersion and DOS properties of the CNT. To describe the FL variation, the authors use the same condition that Khomyakov *et al.* use:

$$W_M = W_{NT} + \Delta V + \Delta E_F = W_{NT} + \Delta V_c + \Delta V_{tr} + \Delta E_F \tag{2.8}$$

As such, the CNT WF (W_{NT}) lines up with the metal WF only if the former is modulated with: the potential shift due to charge rearrangement (ΔV_C), the potential shift due to charge transfer (ΔV_{tr}), and the FL variation in the CNT (ΔE_F). The difference between this method and the method presented by Khomyakov is that for the latter, the potential step functions are explicitly parametrized. In the present case, the relation between the potential step functions is found through an optimization procedure, where ΔV_C is the parameter to be found. The authors solve the optimization problem for ΔV_C using the Lagrange multiplier method with the condition that the total energy is minimized.

The charge transferred to metallic CNTs is uniformly distributed along the tube, due to the uniform DOS near FL and the infinite interface. This is not the case for semiconducting CNTs due to the limited amount of states available near FL. Unlike bulk metal/SC interfaces,

the pinning of the FL in SC CNTs does not necessarily occur deep within the CNT structure [7, 6, 88, 89, 90].

Léonard and Tersoff studied the microscopic electrostatics of bonding of semiconducting CNTs to metal for both side-bonded and end-bonded configurations. The considered geometries are represented in Figure 2.7. Using the density of states given by Mintmire for CNTs [3], they self-consistently solve the charge distribution along the SC-CNT due to a mixture of charge doping f and intrinsic charge distribution within it, which is modulated by the induced electrostatic potential [7]. They describe the charge on the CNT using an approximation consistent with the MIGS picture:

$$\sigma(z) = D_0(E_N - E_F)\mathrm{e}^{-qz} \tag{2.9}$$

where D_0 $(state/(atom \cdot eV))$ is the pinning strength (ie the amplitude of the modification near the interface), E_N the CNL, E_F the FL, and q (nm^{-1}) an effective decay length constant. Both the pinning strength and the CNL depend on the atomic details of the interface, and therefore need appropriate methods to be determined. Here, D_0 and E_N are used to be able to describe an arbitrary interface, allowing the authors to address the electrostatically driven charge distribution in all generality. For planar junctions, high pinning strength leads to low barrier height, that asymptotically approaches $E_C - E_N$ where E_C is the energy of the conduction band edge (see Figure 2.8). The metal effectively causes a SB along the whole CNT. One can see this as a consequence of the extended interface with the slab. In contrast, the barrier height of the end-bonded CNT is only locally modified (see Figure 2.8). That is, the barrier height is modified near the interface, the modification decaying exponentially as in Equation 2.9. In this case FL pinning is said to have no effect on the SB height further within the CNT. Instead, the barrier height is controlled by the metal work function, just as if there were no pinning and no interface dipole. As shown in Figure 2.9, the variation of the charge distribution in the undoped section decreases exponentially.

To incorporate an atomistic description of an interface, it is necessary to use atomically resolved methods, such as DFT. DFT is generally accepted as being an excellent starting point to elucidate the trends that may be encountered while studying the properties of certain systems [80, 73, 88, 89, 90, 82]. Shan and Cho show that the MIGS picture does not fully account for the interface properties of a (8,0)-CNT contacting (111/100)-(Au, Pd, Pt) surfaces [88]: while the dipole moment at the interface depends on the metal and its detailed atomic geometry, it is not directly related to the bonding strength. Even though there is a higher bonding energy with Pd (100) than with the Au (100) surface, the SBH modulation is larger for the Au/CNT system. The dipole formation at the interface also depends on the relative

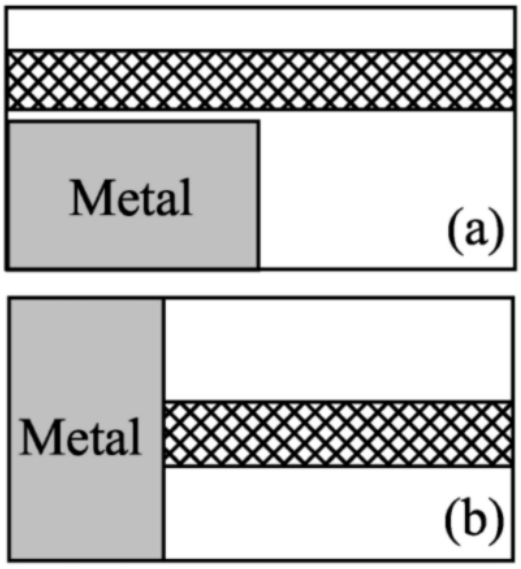

Figure 2.7 Two types of CNT/metal contacts: (a) CNT side-contacted and (b) end-contacted. Reprint with permission from [6]. Copyright (2000) by the American Physical Society

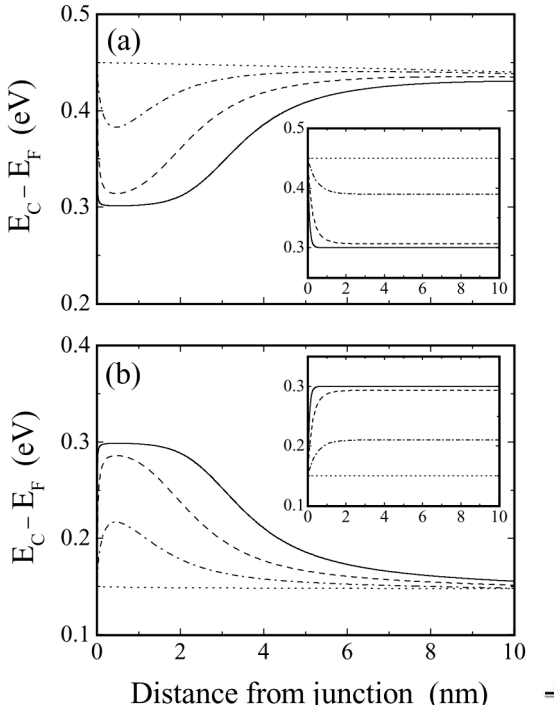

Figure 2.8 Local conduction band-edge for end-contracted CNT versus instance from interface. (a) High work function metal $\phi = 0.3$eV. (b) Low work function metal $\phi = 0.15$ eV. Dotted, dash-dotted, dashed, and solid lines are for $D_0 = 0$, 0.01, 0.1, and 1 state/(atom-eV), respectively. Insets show planar junction for same parameter. Reprint with permission from [6]. Copyright (2000) by the American Physical Society

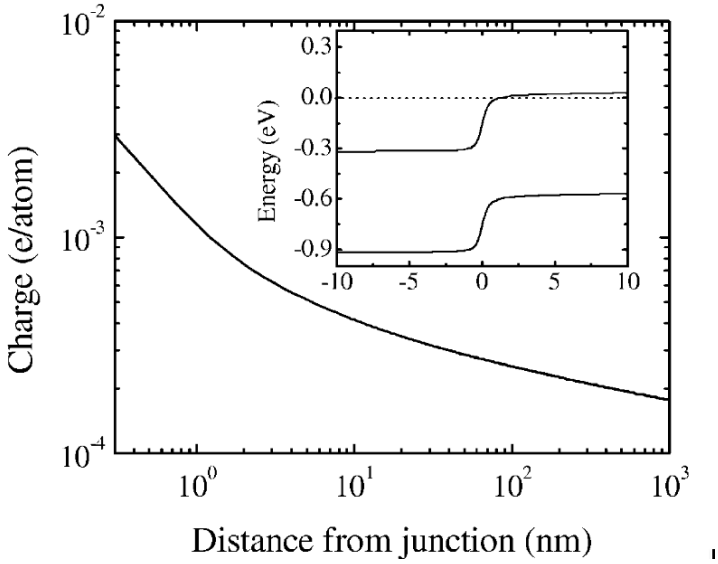

Figure 2.9 Charge per C atom on an undoped SC-CNT section near after an n-doped section. Inset shows corresponding band diagram; dotted line is the Fermi level. Reprint with permission from [7]. Copyright (1999) by the American Physical Society

electronegativity of the species in contact; the atomistic description is thus more subtle than for bulk interfaces [74, 91, 89].

Bridging the behaviour of different scales is a difficult endeavour. The phenomenological models developed for bulk interfaces are not directly applicable, and supplementing them with results obtained with atomistic methods does not generally yield applicable trends or conclusions. Since there is no accepted approach to describe interfaces between metals and CNTs, one finds discrepancies between experimental and theoretical works, as well as a lack of understanding of the details of the formation of a Schottky barrier and the influence of interface dipoles [90]. Theoretical modelling gives various results predicting either no influence of interface states [6, 32], or a high sensitivity to the microscopic bonding configuration and crystal orientation [92, 88], and even that a SC-CNT underneath a contact becomes metallic-like due to the filling of the band gap with interface states [93]. Using a well-known phenomenological model such as MIGS supported by additional observations and conclusions from the use of DFT is the most promising route. Simple models help give simple explanations of systems, and this is how we will approach the interaction of MNCs with CNTs in the following section.

Interfaces with MNCs and their modification

The interface of CNTs with metal surfaces shows some differences with the standard bulk interface picture. It is important to understand the fundamentals of these interfaces in order to progress in the development of applications that are based on these mixed systems. Their uses in applications are quite diverse. For example, they can be used to improve the conductivity of a thin film of intertwined CNTs with the addition of MNCs. Another application is to an enhance detection sensitivity to low concentration gases [94, 9].

An important challenge in using NCs for any application is to keep the size of NCs small and well dispersed to take advantage of their higher effective surface, or active adsorption site geometries. CNTs are a common substrate for MNCs [28, 95, 96], since they allow to control MNC size with the CNT curvature [97], and can provide a porous matrix with which to spatially disperse them.

Another key advantage of CNTs is that their interaction with MNCs depends on the curvature of the CNT. Stakyov *et al.* studied (6,0), (9,0), (12,0), and (18,0)-CNTs with cuboctahedral Au_{13} or Pd_{13} [28]. They find that binding energy decreases as the CNT diameter increases. Higher CNT curvature increases the sp^3 hybridization which contributes to it's affinity to MNCs. The bonding character is of course also modified by the nature of the MNC: Pd_{13} is chemisorbed to the CNTs regardless of the curvature, with adsorption energies of -2.84, -2.24, -1.71, and -1.59 eV for the (6,0), (9,0), (12,0), and (18,0)-CNTs respectively. For the same series of CNTs interacting with Au_{13}s, adsorption energies of -1.88, -1.25, -1.0, and -0.35 eV are found. For Au_{13}/(6,0)-CNT, the bonding involves overlap between the Au d_z^2 orbitals and the C p_z orbitals. The AuNC also tends to merge on lower curvature tubes, whilst staying independent on the tubes with higher curvature.

The difference in bonding energy also affects the charge distribution and charge transfer as observed for the case of CNTs adsorbed on metal surfaces. Theoretical and experimental studies have shown that metal nanoparticles adsorbed on CNTs alter the electron-transport properties of the tubes [47, 16, 15, 94, 9]. To our knowledge there are no theoretical or numerical studies on the size effect of small MNCs on their electronic interaction with CNTs. However, there are some experimental studies dealing with the deposition times of different growth techniques [15, 27].

Gas-sensing is one of the applications of MNC/CNT systems that is the most studied [16, 15, 94, 9, 30, 98, 99, 100]. The understanding of the sensor response is so-far system-dependant. That is, there is no simple generic principle to rely on for the design of a device. A combination of Monte Carlo studies, statistical studies, experimental studies, and atomistic

DFT studies makes up the literature dedicated to this application type. This emphasizes the highly convoluted nature of the following technical problem: how does one scale up what happens at a MNC/CNT interface, when additional molecules intervene, to the performance of a real device? The statistics of a system and the fabrication process are intimately linked, and so far a good amount of work has been done on the effect of CNT distribution and bundle formation in CNT networks [94, 9, 23, 101].

In order to complement such work with the use of MNCs, it is first necessary to acquire a deep understanding of the electronic properties of such systems. It is known that the phenomena guiding the sensitivity of a MNC/CNT hybrid is of course the charge transfer between the MNC and the molecule to detect. However, the high degree of customizability of MNCs poses a formidable challenge, such that the understanding of the interaction between a specific MNC and CNTs requires a full set of characterization, including modelling and experiments. A reproducible testing standard is needed.

When one uses poorly controlled experimental parameters using facile methods, this makes things more complicated. For example Abdelhalim *et al.* fabricate MNC functionalized CNT networks with Au, Pd, and Ag [15]. A low-cost spray deposition process was used to distribute the CNTs and MNCs were then deposited with a thermal evaporation process. Testing the devices with NH_3, CO, and ethanol, the authors find that deposited Pd with a nominal thickness of 1 nm has the best performance out of Au, Pd, and Ag, due to a more uniform distribution of the metal along the tube. The system can be quenched if too long a deposition time is used since a metal film forms around the CNTs, inducing a preferential conduction channel through the metal instead of the CNTs. The AgNC system does not show such high reactivity to the gases used, and it was found that large Ag clusters would form on the CNTs, due to low binding energy to the tubes. In this case, the CNT curvature was not optimized so that the AgNCs stayed small and well dispersed. The more interfaces with AgNCs there are, the more SBs there are, and so the chance that one of these is modulated is higher, which leads to higher sensor sensitivity.

Zanolli *et al.* worked on the fabrication and theoretical characterization of gas sensing interfaces built from MNC/CNT systems [16]. Using (5,5)-CNTs decorated with Au_{13} as a theoretical model, they discuss their results with respect to the sensitivity of CNT-supported AuNCs to NO_2, CO and benzene. When comparing two different amounts of Au applied to the CNT surface (corresponding to 5 or 10 Å), they find that lower deposition times improve the sensitivity. They observed that gold deposition improves the detection of CO and NO_2, whilst it cannot detect benzene. They report that changes in the conductivity are primarily attributed to the adsorption of AuNCs, but also to the adsorption of a gas molecule. The

adsorption of Au suppresses one conduction channel, while the adsorption of NO_2 increases transport by 92%, and the adsorption of CO slightly improves conductivity by 10%.

The change of conductance is attributed to a charge transfer between the adsorbed gas molecule and the CNT, and/or to a modulation of the SB induced by the gas species at the CNT/metal interface [15, 30, 99, 100, 16]. Although the sensing ability of CNTs decorated with MNCs relies on the chemical reactivity of the cluster surface, the whole MNC/CNT system acts as the detection unit of the device. Indeed, the interaction with gas molecules results in an electronic charge transfer between the molecule and the MNC/CNT sensor, which modifies the electronic states around Fermi energy and, hence, the conductivity of the detection unit [16]. Such a conductivity modification can, for instance, be measured by a variation of conductance of a MNC/CNT network. This is mainly controlled by the acceptor/donor character of the interaction of the molecule with the MNC.

When one considers the adsorption of a molecule to a MNC, different phenomenological models can be used to describe the interaction. For example, the adsorption of CO on noble MNCs is well described in terms of the back-donation model due to Blyholder [102, 16, 103]. The mechanism depends strongly on the overlap of the 5σ and $2\pi^*$ orbitals of CO with the d orbitals of the noble MNC, resulting in a mechanism involving electron donation/back-donation. Indeed, CO donates electrons from its σ orbitals to the metal d-σ orbitals while the filled d-π-orbitals of the metal donate electrons back into the empty π^* orbitals of CO. The donation/back-donation balance depends on the metal and the CO adsorption site. This mechanism is usually revealed on noble metal where CO is adsorbed on a high coordination site. For instance, the preferred bonding site for CO on Ag_{55} is the hollow site with greatest coordination, where adsorption energy is 0.47 eV [104].

To conclude on the MNC/CNT interaction as well as the sensing mechanism of such systems, it is important to further analyze atomistic details, all the while keeping in mind the phenomenological explanations to properly present the results that are found. It has been shown that CO affects the charge transferred to a (5,5)-CNT in the case when adsorbed on top of a Au_{13} molecule. The transport properties are slightly modified. Unfortunately this was the only adsorption site that was investigated. To our knowledge, there are no works on the variation of gas sensing sensitivity with respect to the CO adsorption site. Another missing piece is the effect of MNC size on the CO sensitivity of a sensor. To our knowledge, the effect of MNC size on MNC/CNT systems as well as its sensing ability has not yet been explicitly studied in the literature. The present work will attempt to give a clearer picture of this question. Furthermore, no studies on the electronic structure properties of AgNCs on CNTs have been performed. We hope to elucidate the influence of cluster size on the

magnitude of charge transfer and interface dipoles.

CHAPTER 3 METHODOLOGY

The methodology used throughout our work is presented in this chapter. First, the theoretical foundations of the DFT framework are presented. With the fundamentals out of the way, the SIESTA implementation is expounded, as well as the post-processing methods applied to the SIESTA output. Finally, the construction of the models are described and their parametrization is justified.

3.1 Density Functional Theory

DFT is a theoretical framework that enabled the scientific community to algorithmically sidestep the seemingly intractable complexity in large quantum mechanical electron systems. The initial insight can be attributed to the Thomas-Fermi model [105], in which the use of the electron density instead of their wavefunctions was first explored. The theoretical groundwork was then formally layed out by Pierre Hohenberg and Walter Kohn with the theorems named after them [106]. Let us take a look at these fundamental theorems, as well as the approximate implementation first suggested by Walter Kohn and Lu Jeu Sham [107]; this will pave the way the SIESTA implementation that further develops these ideas as to provide an efficient algorithm.

3.1.1 The problem and the Hohenberg-Kohn theorems

Our starting point is the Hamiltonian of a system of nuclei and electrons. The electrons of the system can be separated into core and valence electrons as to simplify notation [108], and so the nuclei together with closely bound core electrons can be considered as ions.

$$\hat{H} = \hat{H}_{ion} + \hat{H}_{el} + \hat{H}_{ion-el} = (\hat{T}_{ion} + \hat{H}_{ion-ion}) + (\hat{T}_{el} + \hat{H}_{el-el}) + \hat{H}_{ion-el}$$

The three components of this Hamiltonian correspond to contributions by the ions, the valence electrons, and the interaction between them. The Born-Oppenheimer approximation is applicable, due to the fact that the electrons are much lighter than the nuclei [105, 108, 109], and so in the electrons time-frame the ions appear fixed. We can thus drop the ionic kinetic energy $\hat{T}_{ion}$.

We consider ions of mass M_μ at positions $\mathbf{R}_\mu$ and of positive charge $eZ_{val,\mu}$, which is the tally of the core electrons and and the Z_μ protons in the μ-*th* nucleus. Electrons are of mass m_e

and are at positions $\mathbf{r_i}$.

$$\hat{H}_{ion-ion} = \sum_{\mu} \left[\frac{1}{2} \frac{e^2}{4\pi\epsilon_0} \sum_{\nu \neq \mu} \frac{Z_{val,\mu} Z_{val,\nu}}{|\mathbf{R}_\mu - \mathbf{R}_\nu|} \right] \quad , \tag{3.1}$$

$$\hat{H}_{el} = \sum_{i} \left[-\frac{\hbar^2}{2m_e} \nabla_i^2 + \frac{1}{2} \frac{1}{4\pi\epsilon_0} \sum_{j \neq i} \frac{e^2}{|\mathbf{r_i} - \mathbf{r_j}|} \right] \quad , \tag{3.2}$$

$$\hat{H}_{ion-el} = -\frac{1}{2} \frac{e^2}{4\pi\epsilon_0} \sum_{\mu} \sum_{i} \frac{Z_{val,\mu}}{|\mathbf{R}_\mu - \mathbf{r_i}|} \tag{3.3}$$

Let us now rearrange the terms of the Hamiltonian for what follows:

$$\hat{H}_0 = \hat{T}_{el} + \hat{H}_{el-el} + \hat{H}_{ext} \tag{3.4}$$

where

$$\hat{H}_{ext} = \hat{H}_{ion-ion} + \hat{H}_{ion-el} = \int d\mathbf{r} v_{ext}(\mathbf{r}) \hat{\rho}(\mathbf{r})$$

includes all ionic contributions, which can be noted as external since they are decoupled from the electrons contributions through the Born-Oppenheimer approximation. $\hat{\rho}(\mathbf{r})$ corresponds here to the charge density operator. The potential associated to these contributions is defined as $v_{ext}(\mathbf{r})$. The total energy functional associated with Equation 3.4 is the following:

$$E[\rho] = \langle \Psi | \hat{H}_0 | \Psi \rangle \tag{3.5}$$

$$= \langle \Psi | \hat{T}_e + \hat{H}_{el-el} | \Psi \rangle + \langle \Psi | \hat{H}_{ext} | \Psi \rangle \tag{3.6}$$

$$= F_{HK}[\rho] + \int d\mathbf{r} v_{ext}(\mathbf{r}) \rho(\mathbf{r}) \tag{3.7}$$

where $\rho(\mathbf{r})$ is now a position dependant scalar instead of an operator. The external contributions are in contrast with $F_{HK}[\rho]$ which is a universal functional shared by all electron systems; the former can be seen as parametrizing the latter, giving rise to the diverse properties found in materials. Instead of solving the many body problem stemming from Equation 3.4 by solving for the wavefunctions, Hohenberg and Kohn proved the following theorems on the grounds that the ground state is non-degenerate and that the external potential is local and spin-independent [108, 109, 105]:

1. There is a bijection between the external potential $v_{ext}(\mathbf{r})$ and the electronic ground state density $\rho(\mathbf{r})$, up to a trivial constant.

2. The minimization of the energy functional $E[\rho(\mathbf{r})]$ by the variational method corresponds

to the true ground state energy.

The first theorem justifies, in principle, that knowing the universal functional $F[\rho(r)]$ would allow material scientists to generate a material's electronic structure and expect it to be the right one. The second theorem hints at a method of calculating the latter using variational numerical methods. The energy functional in Equation 3.7 could be calculated with an initial guess for the charge density, and then minimized using a variational scheme as to recover the correct ground state energy and corresponding ground state charge density.

This is grand, but it does not provide any clues on what the key element, $F[\rho(r)]$, could be. In steps the Kohn-Sham formulation, providing a practical framework with which to approximate the universal functional and thus calculate material ground state properties.

3.1.2 The Kohn Sham formulation

Finding the universal functional to a many-body electron system is a monumental task. So monumental, in fact, that the ruse developed by Kohn and Sham circumvents this by deriving a set of effective one particle equations [105, 109, 110] to replace the many-electron kinetic energy functional. The Kohn Sham formulation uses the Levy and Lieb (LL) formulation of the universal functional: the difference with the previous formulation, as seen in Equation 3.8, is simply to state that one takes $F[\rho]_{LL}$ to be the minimum of $F[\rho]_{HK}$ with respect to the wavefunction approaching a constrained set of solutions in the charge density's functional space.

$$F[\rho]_{LL} = \min_{\Psi\to\rho}\left\{\langle\Psi|\hat{T}+\hat{U}_{ee}|\Psi\rangle\right\} \tag{3.8}$$

where ρ is any non-negative density such that

$$\int \rho(\mathbf{r})\mathrm{d}\mathbf{r} = N \qquad \text{and} \qquad \int |\nabla\rho^{1/2}(\mathbf{r})|^2\mathrm{d}\mathbf{r} < \infty \tag{3.9}$$

This constraint forces the number of electrons to be of N, and dismisses any solution that brings up "unphysical" solutions that diverge to infinity.

Now, the first step to formulating a practical solution to the many-body electron problem is by reformulating Levy and Lieb's universal functional, separating out the classical Coulombic interaction (or Hartree interaction) between electrons [105, 109, 110]:

$$F_{LL}[\rho] = G[\rho] + \frac{1}{2}\frac{e^2}{4\pi\epsilon_0}\sum_{\sigma\sigma'}\int d\mathbf{r}\int d\mathbf{r}'\frac{\rho_\sigma(\mathbf{r})\rho_{\sigma'}(\mathbf{r}')}{|\mathbf{r}-\mathbf{r}'|} \tag{3.10}$$

where $G[\rho] = T[\rho] + W_{xc}[\rho]$ takes into account the kinetic energy functional and the exchange and correlation functional.

By swapping the universal functional in Equation 3.7 with the previous equation we find:

$$E[\rho] = T[\rho] + W_{xc}[\rho] + \frac{1}{2}\frac{e^2}{4\pi\epsilon_0}\sum_{\sigma\sigma'}\int d\mathbf{r}\int d\mathbf{r}'\frac{\rho_\sigma(\mathbf{r}')\rho_{\sigma'}(\mathbf{r}')}{|\mathbf{r}-\mathbf{r}'|} + \int d\mathbf{r} v_{ext}(\mathbf{r})\rho(\mathbf{r}) \tag{3.11}$$

The last hurdle is the kinetic energy functional. This term, in the case of a many-body electron system, depends both on exchange and correlation effects. This is where Kohn and Sham proposed to separate out these undesirable dependencies. To do so, they propose to change the kinetic energy functional $T[\rho]$ of a many-body electron system by that of a fictitious non-interacting electron system, $T_s[\rho]$. It is well known that the wavefunction of such a system is exactly described by an anti-symmetric wave function built using a Slater determinant of one-electron wavefunctions. The kinetic energy of such a system has an analytic solution:

$$T_s = -\frac{\hbar^2}{2m}\sum_i \langle\psi_i|\nabla^2|\psi_i\rangle \tag{3.12}$$

It is necessary to compensate for the correlation effects not taken into account with $T_s[\rho]$, so they are added into the term $W_{xc}[\rho]$ such that [111] :

$$T_s[\rho] + E_{xc}[\rho] = T[\rho] + W_{xc}[\rho]$$

In doing so, we find the Kohn-Sham formulation of the energy functional:

$$E[\rho]^{KS} = T_s[\rho] + \frac{1}{2}\frac{e^2}{4\pi\epsilon_0}\sum_{\sigma\sigma'}\int d\mathbf{r}\int d\mathbf{r}'\frac{\rho_\sigma(\mathbf{r}')\rho_{\sigma'}(\mathbf{r}')}{|\mathbf{r}-\mathbf{r}'|} + \int d\mathbf{r} v_{ext}(\mathbf{r})\rho(\mathbf{r}) + E_{xc}[\rho] \tag{3.13}$$

Finally, applying the variational principle under the fixed density constraint [109]:

$$\frac{\delta T_s[\rho]}{\delta\rho(\mathbf{r})} + v_r = \mu_r \tag{3.14}$$

where μ_r is the chemical potential for the non-interacting system, which should coincide with that of the interacting system μ. The reference potential v_r contains the contributions from the external potential, the Hartree potential and the exchange correlation correction:

$$v_r = v_{ext}(\mathbf{r}) + \int d\mathbf{r}'\frac{\rho(\mathbf{r}')}{|\mathbf{r}-\mathbf{r}'|} + \mu_{xc}[\rho](\mathbf{r}) \tag{3.15}$$

where

$$\mu_{xc}[\rho](\mathbf{r}) = \frac{\delta E_{xc}[\rho]}{\delta \rho(\mathbf{r})} \tag{3.16}$$

$$E_{XC}[\rho] = F_{HK}[\rho] - (T_s[\rho] + E_{Hartree}[\rho]) \tag{3.17}$$

Within this formulation, the unknowns are all jammed into the exchange and correlation term $E_{xc}[\rho]$. Current research deals with building proper approximations for this term, such as the Local Density Approximation (LDA), the Generalized Gradient Approximation (GGA), and hybrid methods.

The Kohn-Sham wavefunctions are built self-consistently using an initial guess for the charge density distribution. The basis set used to generate this starting point along with all subsequent steps of the self-consistent loop depends on the implementation being used. The method stemming from the physics community is the plane-wave method, using summations of plane waves to build the Kohn-Sham wavefunctions. This approach needs little to no parametrization and is excellent for small to medium system sizes. Other methods, generally developed within the chemistry community, are based on the definition of the basis sets as atom-centered functions. These linear combinations of atomic orbitals (LCAO) methods are made up of several subgroups, of which the method implemented in the SIESTA method takes part.

3.2 The SIESTA method

The SIESTA method [112] essentially reformulates the Kohn-Sham one electron hamiltonian, and dresses it in an efficiency-oriented algorithm. The reformulation reflects choices the developers made, and will be further developed in the following subsections.

The algorithm is schematically represented in Figure 3.1. There are three main blocks: the initialization, the main process (containing the self-consistency loop nested in the geometry optimization loop), and the finalization where user requested output is prepared and formatted. The following section will address how different input parameters affect the SIESTA internals as to better grasp the following parametrization and convergence studies.

3.2.1 Initialization

To set up a SIESTA calculation, one must create a text file under the flexible data format (fdf), which is described in the SIESTA users guide. All of the parameters discussed in this section are set in this input file. The most concrete parameters are of course the unit cell and the atomic geometry. The unit cell will be repeated periodically in 3D, and SIESTA will

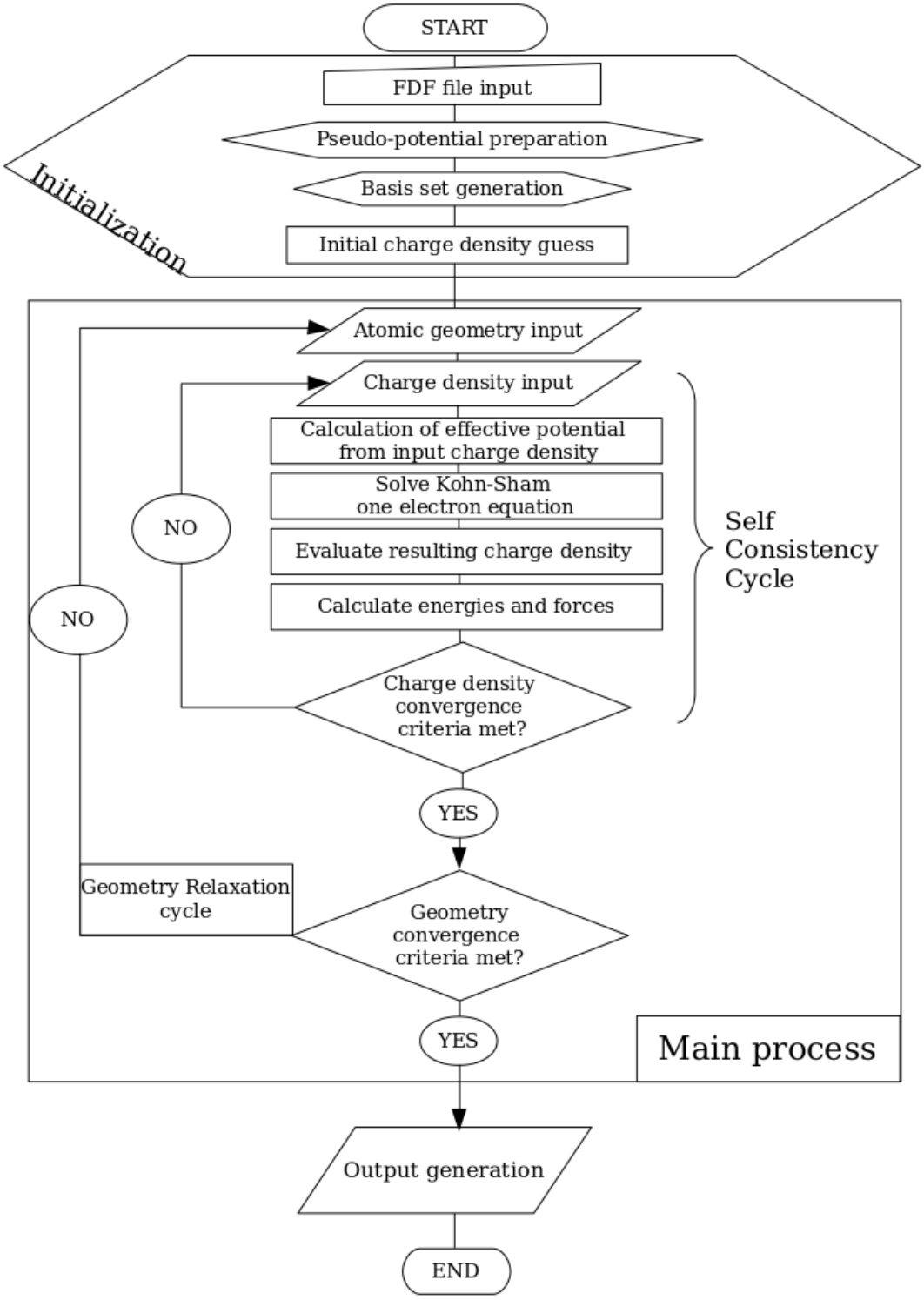

Figure 3.1 Schematic representation of the SIESTA algorithm

recognize whether the atomic geometry is molecule-like, chain-like, slab-like, or crystal-like depending on the amount of padding, or vacuum, as well as where it is positioned in the unit cell.

The initialization of the SIESTA process ends with the construction of the naïve electronic structure (ie basic shell model) as a first guess to start the main process of finding a self-consistent solution to the Kohn-Sham equation. To do this, one needs the pseudopotential files of all atomic species in the system under study, as well as their corresponding atomic orbital basis (AOB) sets. The pseudopotentials (PPs) can be generated using several flavours [109], but in all cases their purpose is to model the core electrons without taking them into account explicitly. In our case, we used relativistic Troullier-Martins norm-conserving semi-local PPs generated with the Atoms package. The AOBs are constructed internally during the SIESTA initialization step, using the input pseudopotentials which are transformed to a fully non-local from proposed by Kleinman and Bylander [112]. The advantage of such a projection is entirely computational: only the local part of the pseudopotential needs to be calculated on the real-space grid, while the fully non-local part can be calculated with two-centre integrals. The input parameters for both the PPs and AOBs were taken from a reference database of PPs and AOBs that were optimized using a simplex algorithm, with the goal of describing bulk crystal lattice parameters as precisely as possible [113].

3.2.2 Main process: Self-consistency and geometry optimization loops

Once the initial charge density guess is derived from the PP/AOB combinations and atomic geometry, the one electron Kohn-Sham equation is solved using the effective potential deduced from the charge density. The Kohn-Sham equation used in the SIESTA method is slightly modified compared to that from Equation 3.13 due to the core states being accounted for with pseudopotentials separated as seen in the previous paragraph:

$$\hat{H} = \hat{T}_s + \sum_i V_i^{KB} + \sum_i V_i^{NA}(\mathbf{r}) + \delta V^H(\mathbf{r}) + V_{XC}(\mathbf{r}) \tag{3.18}$$

where

$$V_i^{NA} = V_i^{local} + V_i^{atom}$$

is the effective ionic potential, and δV^H is the classical electrostatic potential generated by the difference between the self-consistent electron density and the sum of atomic densities. V_i^{local} and V_i^{KB} are the local and non-local parts of the pseudopotential formulation. This formulation is interesting because the first two terms of Equation 3.18 only involve two-centre integrals calculated in reciprocal space and are tabulated as a function of interatomic distance

[112]. The detail of these calculations are controlled by the k-point input chosen by the user.

The other terms are calculated on the real space grid, and so their results are controlled by setting its fineness. This is done using the MeshCutOff parameter, defined as the maximum kinetic energy of the plane waves that can be represented in the grid without aliasing [112]. The correspondence between the real-space grid fineness and the MeshCutOff parameter (E_{mc}) is:

$$\Delta x = \sqrt{\frac{\hbar^2 \pi^2}{2 m_e E_c}} \propto \sqrt{\frac{1}{E_c}} \tag{3.19}$$

The separation of reciprocal space and real-space terms further enables parallelization over either real or reciprocal space, which is also chosen by the user.

Finally, these choices affect the ease with which self-consistent convergence of the charge density is reached, and each system has its own "sweet spot".

To define convergence of the electronic charge density we used the default choice in SIESTA, which is to require a maximal discrepancy between the input density matrix (DM) and the output DM:

$$DM_{ij}^{out} - DM_{ij}^{in} <= 10^{-4} \quad \forall \ i, j \tag{3.20}$$

Instead of only using the output DM as the input DM in the subsequent iteration of the self-consistency cycle, we have used the Broyden mixing scheme [114], which has been shown to speed up convergence at a small cost in memory. We chose to save the DMs of the three previous iterations, that are then mixed to form a new DM input at the top of the loop. The mixing parameter in the case of linear mixing was set to 0.01 and is set to occur at the beginning of the SCF loop, as well as every subsequent 100 SCF iterations.

The charge density coming out of the SIESTA SCF pipeline is the following [112]:

$$\rho(\mathbf{r}) = \sum_i \int_{BZ} n_i(\mathbf{k}) |\psi_i(\mathbf{k}, \mathbf{r})|^2 \mathrm{d}\mathbf{k} = \sum_{\mu', \nu'} \rho_{\nu' \mu'} \phi^*_{\nu'}(\mathbf{r}) \phi_{\mu'}(\mathbf{r}) \tag{3.21}$$

where the sum is over all basis orbitals $\phi_\mu(\mathbf{r})$ in real space, and the density matrix

$$\rho_{\mu\nu} = \sum_i \int_{BZ} c_{\mu i}(\mathbf{k}) n_i(\mathbf{k}) c_{i\nu}(\mathbf{k}) \mathrm{e}^{i\mathbf{k}(\mathbf{R}_\nu - \mathbf{R}_\mu)} \mathrm{d}\mathbf{k} = \sum_i \rho^i_{\mu\nu} \tag{3.22}$$

is real and equivalent by translation of the unit cell vectors.

The Kohn-Sham energy corresponding to this charge density is

$$E^{KS} = \sum_{\mu} \nu(T_{\mu\nu} + V^{KB}_{\mu\nu})\rho_{\mu\nu} + \frac{1}{2}\sum_{IJ} U^{NA}_{IJ}(\mathbf{R_{IJ}}) + \sum_{I<J} \delta U^{local}_{IJ}(R_{IJ}) - \sum_{I} U^{local}_{I} + \int V^{NA}(\mathbf{r})\delta\rho(\mathbf{r})\mathrm{d}\mathbf{r} + \frac{1}{2}\int \delta V^{H}(\mathbf{r})\delta\rho(\mathbf{r})\mathrm{d}\mathbf{r} + \int \epsilon^{xc}(\mathbf{r})\rho(\mathbf{r})\mathrm{d}\mathbf{r} \tag{3.23}$$

Finally, the geometry optimization uses the forces calculated by direct differentiation of eq. 3.23.

3.2.3 Post-Processing

Band structure

Once a self-consistent solution is delimited in the SIESTA method, it is possible to look into the results by investigating the band structure and corresponding DOS. The band structure is built using the Monkhorst and Pack partition of k-points specified in the input. Each k-point supports a family of solutions with different energies. Filling this band-structure from the lowest energy onward leads to the Fermi level being defined as the occupied state of highest energy in the case of metallic systems, and the mid-gap in the case of semiconductors and insulators. Plotting the dispersion relation $E(\mathbf{k})$ against $\mathbf{k}$ constitutes the band structure, giving insight into the availability of different energy states depending on the chosen k-vector.

DOS

The DOS is simply the amount of states available at each energy; it corresponds to the sum of available k-states for one energy. Given that the solutions do not form a perfect continuum due to the discretization of the problem to be solved numerically, a convolution with a Gaussian-like function is used to group states that are close in energy.

$$\mathrm{DOS}(E) = \sum_{i} \int_{BZ} \delta(E - E^{KS}_{i}(\mathbf{k})) \cdot \frac{\mathrm{e}^{-(\frac{E - E^{KS}_{i}(\mathbf{k})}{\sigma})^2}}{\sigma\sqrt{\pi}} \mathrm{d}\mathbf{k} \tag{3.24}$$

The parameter σ controls how much smearing is applied to the DOS. Throughout this work a smearing parameter of 0.02 was used.

PDOS

The Projected or Partial DOS is the projection of the DOS onto a selection of basis set orbitals $\phi_\mu(\mathbf{r})$:

$$\mathrm{PDOS}_\mu(E) = \sum_i \int_{BZ} |c_{\mu i}(\mathbf{k})|^2 \delta(E - E_i^{KS}(\mathbf{k})) \cdot \frac{\mathrm{e}^{-(\frac{E-E_i^{KS}(\mathbf{k})}{\sigma})^2}}{\sigma\sqrt{\pi}} \mathrm{d}\mathbf{k} \tag{3.25}$$

LDOS

The LDOS is the spatial distribution of the Kohn-Sham probability density weighted by the corresponding DOS:

$$\mathrm{LDOS}(\mathbf{r}) = \sum_i \mathrm{DOS}(E_i) \cdot |\psi_i(\mathbf{r})|^2 \tag{3.26}$$

Voronoi charge analysis

The Voronoi charge population analysis accounts for how much charge deformation density flows in and out of a given Voronoi cell surrounding an atomic position. The deformation density corresponds to the difference between the initial charge density guess ($\rho^{in}(\mathbf{r})$) and the self-consistent charge density ($\rho(\mathbf{r})$) at the end of the SCF cycle. An atom's Voronoi cell corresponds to all points in space that are closest to its position. Thus, the Voronoi charge attributes to a given atom is [115]:

$$Q_A^{VDD} = -\int (\rho(\mathbf{r}) - \rho^{in}(\mathbf{r})) \mathrm{d}\mathbf{r} \tag{3.27}$$

The charge population analysis used in the rest of this study thus relies only on geometric properties, and so does not depend on the choice of basis sets used for the various chemical species found in the system.

Work Function

The work function of an infinite periodic system does not correspond directly to its Fermi level within the SIESTA implementation. This is due to the reference zero energy being the average value of the deformation potential δV^H, therefore not coinciding to the vacuum's zero energy. The following method allows one to retrieve this information.

First, one must recuperate the profile of the deformation potential δV^H. To do this, it is necessary to output both the final electrostatic potential and the initial effective ionic potential V^{NA}. Once these two output files are generated, they need to be macroscopically averaged

using the "macroave" utility distributed with the SIESTA package. This averaging step is necessary to properly synthesize the profile of the deformation profile traversing the region from within the slab to vacuum [116]. Once the relative position of the inner slab potential (V_{slab}) is determined with respect to the vacuum's value (V_{vacuum}), one can add the difference between the two to the Fermi level of the system. In doing so, the work function Φ of the surface under study can be defined [117]:

$$\Phi = E_F + \Delta V = E_F + V_{slab} - V_{vacuum} \tag{3.28}$$

3.3 Model dependant parametrization and convergence

The SIESTA method suggests default values of several simulation parameters. However, good practice warrants justified choices regarding these values. Justifications are hard to generalize, as they come down to compromises that are system-dependant. It is important to first optimize the system components independently, following up with a convergence of the resulting joint systems. We will present the parametrization of each sub-system, that is CNTs, AgNCs as well as bulk and slab systems, and the CO molecule. After elucidating these choices, we will approach the convergence of joint systems, with respect to key parameters.

3.3.1 Initial parametrization of isolated systems

Carbon nanotubes

Two CNT archetypes are chosen to study the effects of AgNC adsorption: a metallic armchair (5,5) CNT and a (10,0) zigzag semiconducting CNT. These CNTs have a similar diameter which make the comparison of their interfacial behaviours with various AgNCs more straightforward. Their initial geometries were generated within the Atomic Simulation Environment (ASE) framework [118]. The carbon PP/AOB pair was optimized as to reproduce graphite's unit cell parameters. This pair was also tested with graphene's geometry, and its geometry and band structure were both satisfyingly reproduced [113]. We will see in the following chapter that the carbon nanotubes electronic character is also well reproduced with these choices. Using this combination of pseudopotential and basis orbitals, both CNTs were optimized using a force tolerance of 0.002 eV/Å. The MeshCutOff was set quite high, 400 Ry. The modifications to the C-C bond lengths and representative angles as shown in Figure 3.2 are slight in either case. These slight modifications are in agreement with the work presented in [42, 119].

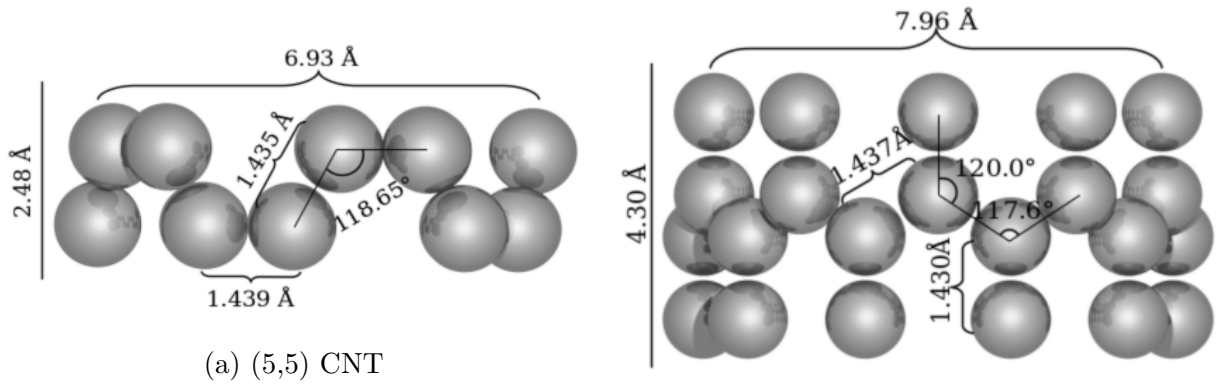

(a) (5,5) CNT

(b) (10,0) CNT

Figure 3.2 CNT optimized geometries

Ag-based systems

The Ag PP/AOB pair was optimized as to reproduce bulk silver's unit cell parameters [113]. In the case of Ag clusters or slabs, it is important to take into account the extension of surface states into the vacuum, and so AOBs were generated as suggested in García-Gil *et al.*'s paper on noble metal surfaces [120], that is with an extra set of diffuse *s* orbitals for Ag surface atoms. Polarization was not taken into account as it has been noted that it does not strongly affect the properties of the AgNC [63].

It is not possible to relax the geometry of a AgNC into an icosahedral structure from any which starting geometry, since there exist other stable structures that could easily be relaxed into [121]. To force the AgNCs to relax into the icosahedral structure, we first find a minimum in the maximum force applied to the set of atoms, as can be seen in Figure 3.3a. In the case of the Ag_{13}, preserving the icosahedral symmetry comes down to applying a similarity operation, scaling the distance between the central atom and those comprising the surface layer, as seen in Figure 3.3b. In the case of Ag_{55}, one cannot talk of a similarity operation since each layer needs to be scaled away from the central atom independently to find a proper starting point; it is equivalent to the Ag_{13} with an additional layer of surface atoms. The same can be said of Ag_{147}, which comprises of 3 layers, or a Ag_{55} with one additional layer. In all cases, once a suitable starting point is found, the structure is relaxed with a tolerance of 0.01 eV/Å. The final systems are presented in Figure 3.4. The average bond lengths for the Ag_{13} is of 2.84 Å, which agrees with Fernandez *et al.*'s result for an amorphous Ag_{13} geometry (13-III) [121]. They did not find an icosahedral geometry for this cluster, perhaps because they did not begin the geometry optimization from the right initial geometry.

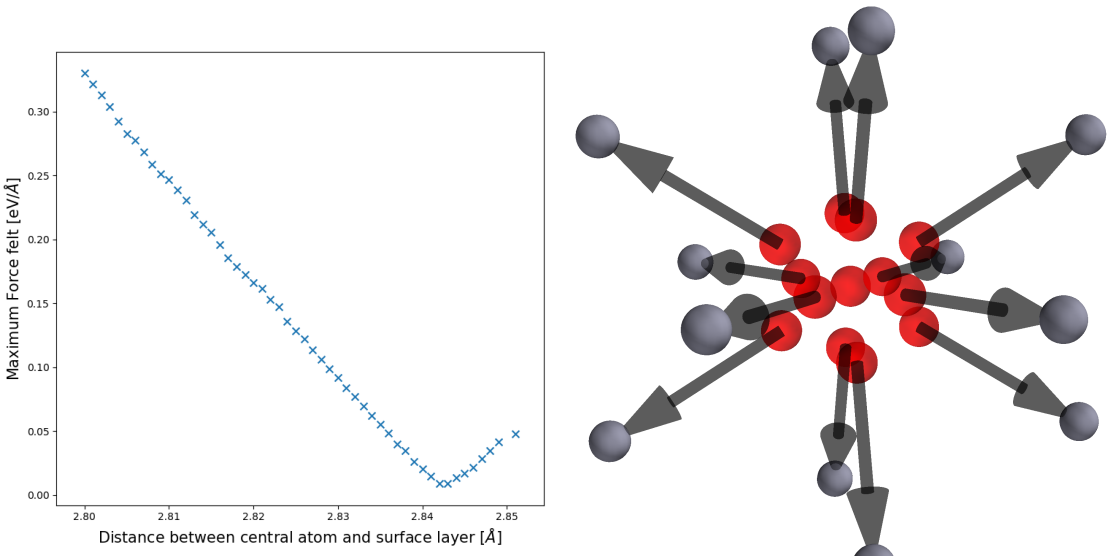

(a) Search for suitable starting point

(b) Similarity operation

Figure 3.3 Method used for relaxing into the icosahedral geometry for the Ag_{13} system

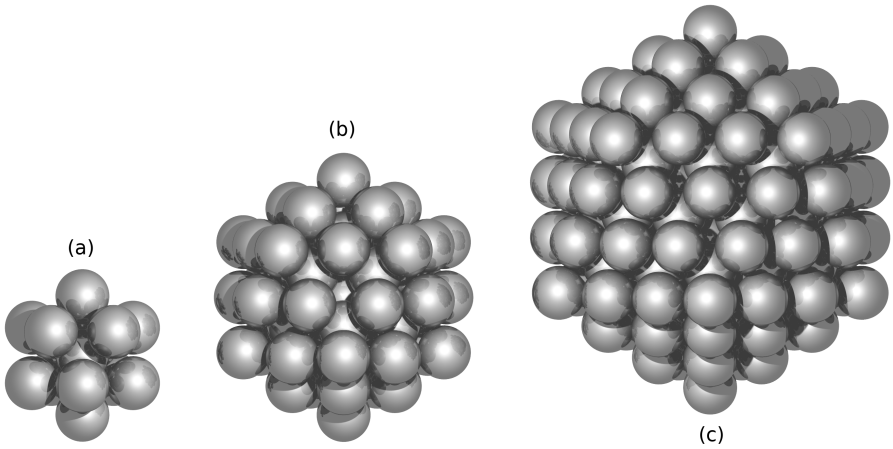

Figure 3.4 Final icosahedral AgNC geometries with (a) 13 Ag atoms (b) 55 Ag atoms and (c) 147 Ag atoms

Table 3.1 Average distance of layers with respect to central atom

Cluster type	First Layer	Second Layer	Third Layer
Ag_{13}	2.84360 ± 0.00007	NA	NA
Ag_{55}	2.835 ± 0.005	4.92 ± 0.02	NA
Ag_{147}	2.8248 ± 0.0007	4.863 ± 0.001	7.3 ± 0.7

Table 3.2 Layer-dependant coordination number

Cluster type	Core [center]	First Layer [vertex]	Second Layer [vertex/edge]	Third Layer [vertex/edge/face]
Ag_{13}	12	6	NA	NA
Ag_{55}	12	12	6/8	NA
Ag_{147}	12	12	12/12	6/8/9

Carbon Monoxide

In the case of the oxygen molecule, the AbInit [122] online repository was used [123] for its PP and the SIESTA split method was used to generate the double zeta polarized (DZP) AOB [112]. The carbon molecule uses the same PP as the C atoms making up the CNTs, but also uses the SIESTA split method to generate a DZP AOB. The energy shift and split norm parameters were sampled as to obtain a CO molecule with an interatomic distance approaching the experimental value of 1.13 Å and a dipole moment approaching 0.122 D, after a geometry optimization with a 0.0001 eV/Å tolerance. We found that generating AOBs with a 0.01 Ry energy shift and a 0.35 split norm provides results that are within 2% of the experimental values [124]: a bond-length of 1.14 Å, and a dipole moment of 0.124 D.

3.3.2 Interface dependant parametrization and convergence

Choosing the PP/AOB pairs for the isolated systems allows us to look into the convergence of the parameters concerning adsorbed systems. Being that the systems under study are periodic along one dimension, it is of interest to choose the size of the supercell to be used in the rest of the study. The supercell consists of n repetitions of the converged CNT unit cell geometries given in Figure 3.2.

Furthermore, the choice of k-point sampling and real space grid fineness must be assessed. To this end, several characteristics of the Ag_{13}/CNT system were studied with respect to k-point sampling and grid fineness: single-point adsorption energy, dipole moment, and max force applied to any atom. One could increase both parameters to very high values, but this would result in calculations taking too much time and memory to complete. This is why it is interesting to look for a calculation performance "sweet-spot", achieving sufficiently precise calculations with minimal computational resources.

Such an example can be found in Figure 3.5a, where the adsorption energy for 13 repetitions of a (5,5) CNT unit cell with Ag_{13} is fitted with a Morse potential. The resulting equilibrium

distances and adsorption energies are given in Figure 3.5b. The MeshCutOff parameter is inversely proportional to the grid size, as seen in Equation 3.19, so higher values lead to finer grids. This work was done for both (5,5) and (10,0) CNTs, with CNT unit cell repetitions ranging from 1 to 20. The results are presented in Table 3.3.

There are two features that can be touched upon. First, the mesh cutoff converges for lower values in the case of the Ag_{55} and Ag_{147} systems, as compared to the Ag_{13} systems. This is not surprising as these larger clusters have a larger equilibrium distance than for the Ag_{13} case. This means that the CNT interacts with a more "diffuse" charge density due to the AgNC. Second, a lower k-point sampling is required for the semiconducting system than for the metallic (5,5) CNT. This is a common occurrence, as metallic systems are known to be more difficult to converge with respect to the k-point sampling than semiconducting systems. The reason for this is that "charge sloshing" is likely in the case of metallic systems around the Fermi level, since the conductance band is partially occupied.

Table 3.3 Converged simulation parameters for all simulated structures

System Type		Supercell size [Å/*rep*]	MeshCutOff [Ry]	k-point sampling
(5,5)	Ag_{13}	39.65 / 16	400	16
	Ag_{55}	39.65 / 16	200	16
	Ag_{147}	49.56 / 20	200	16
(10,0)	Ag_{13}	34.38 / 8	400	12
	Ag_{55}	34.38 / 8	200	12
	Ag_{147}	34.38 / 8	200	12

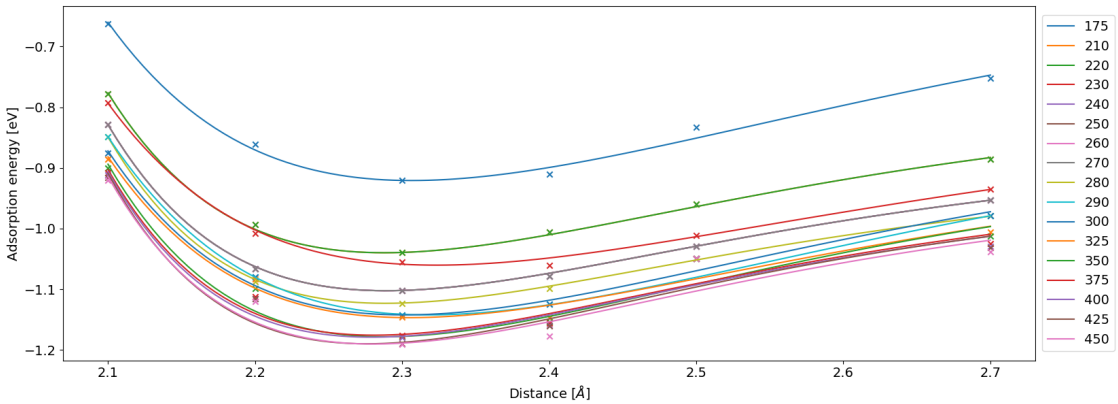

(a) Morse fits for each MeshCutOff values spanning from 175 to 450 Ry

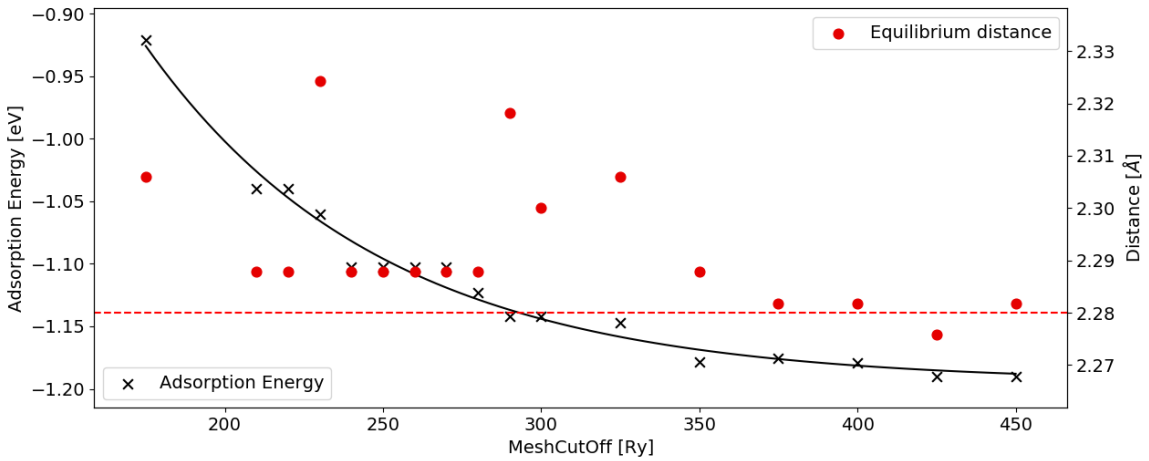

(b) Resulting convergence at 400 Ry

Figure 3.5 Example of the MeshCutOff convergence for 13x(5,5)-CNT+Ag_{13}

Finally, let us look into the convergence of the system characteristics with respect to the supercell size. An illustration of the variation of the supercell size is given in Figure 3.6. The unit cell size defines the distance between a AgNC and its periodic image.

Figure 3.7 shows the variation of the adsorption energy attributed to (5,5)-Ag_{13}/CNT, as well as the charge transferred from the AgNC13 to the (5,5)-CNT, with respect to the amount of (5,5)-CNT unit cell repetitions used. The inset shows the equilibrium distance between the CNT and the AgNC with respect to the latter. Convergence is reached for the adsorption energy and equilibrium distance before it is reached for the charge transfer. It is important to take this into account since we are interested in the charge transfer characteristics of these systems. The supercell size convergence is therefore defined with respect to the charge transfer since we have set out to study an isolated interface.

This aspect has not yet been explicitly mentioned in the literature concerning similar 1D systems. For example, previous work on a CNT/AuNC13 system considered a supercell using 9 (5,5)-CNT unit cell repetitions, leading to a distance of approximately 14.8 Å between the clusters [16]. In our case, we find that a distance of 25 Å is necessary for the charge transfer from the clusters to the CNT to converge. This is due to the long-range effect of the charge distributions tail. These two results are not directly comparable, since the cited work studies the effect of Au and not Ag. It may be that AuNC13 is not as sensitive as its silver counterpart, but the reason for this supercell size is not justified in Zanolli *et al.*'s work [16].

As for the other systems considered here, the supercell sizes converged with respect to charge transfer are presented in Table 3.3, along with other parameters used for the rest of this study. The equilibrium distances between the CNTs and various Ag systems are presented in Figure 3.8.

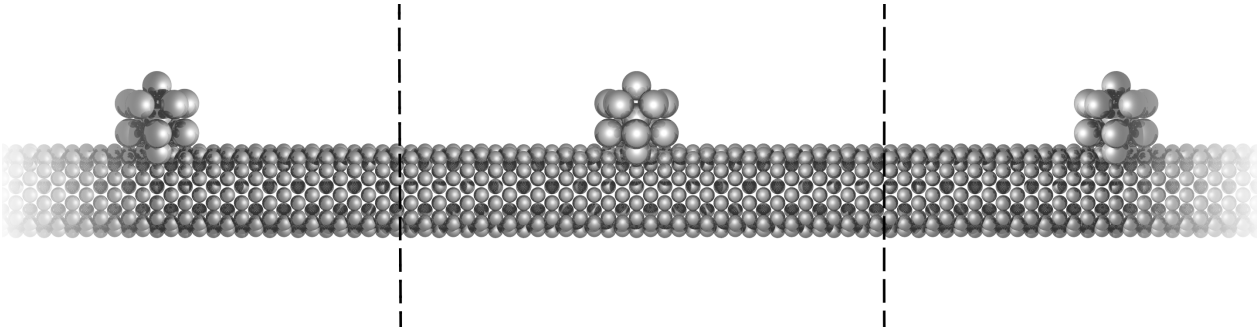

Figure 3.6 Illustration of the supercell and the periodic images of the AgNC. Dashed lines represent the unit cell borders along z.

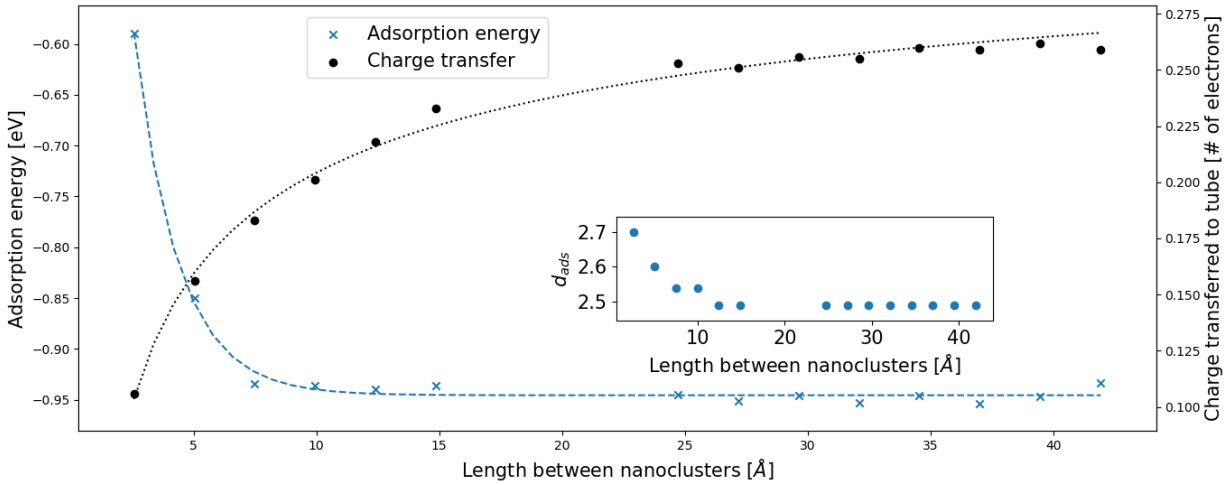

Figure 3.7 Supercell convergence for the (5,5)-CNT+Ag_{13} system

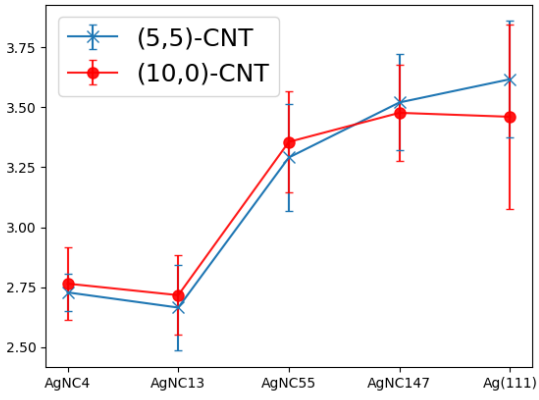

Figure 3.8 Equilibrium distances between CNTs and AgNCs

CHAPTER 4 RESULTS AND DISCUSSION

The present chapter deals with the quantum size effects of both isolated and joint systems. First the electronic and structural properties of the isolated converged constituents (CNTs, AgNCs, Ag slab) will be analyzed in detail. Second, the interface between AgNCs and CNTs will be investigated and described. Finally, the interaction of CO with AgNCs, followed by the modification of the Ag_{55}/CNT system through CO adsorption will be discussed.

4.1 Electronic and structural properties of isolated systems

Carbon Nanotubes

The calculated DOS and band structure of the (5,5)-CNT is shown in Figure 4.1a. The features are similar to those found with the tight binding approach that was presented in Figure 2.2a. A metallic behaviour can be deduced from the partially filled valence band. The degeneracy of states at the high-symmetry X point is, however, lifted. This is due to the curvature of the CNT that was not taken into account in the tight-binding approach. The curvature of the CNT modifies the interaction between π-orbitals along the CNT axis, which explains why the states of X-point symmetry span away from one another. The length of the periodic unit (2.48 Å) of our (5,5)-CNTs is very close to the optimized unit cell length of 2.46 Å found by Demichelis *et al.*, using DFT with a hybrid B3LYP functional [119]. The optimized tube diameter from our work (6.93 Å) is also close to the value found with the DFT/B3LYP approximation (6.86 Å). Strano *et al.* measured a diameter of 6.88 Å with Raman spectroscopy [125], which is within 1 % of our result.

The (10,0)-CNT electronic structure (Figure 4.1b) is also similar to the tight-binding band structure reported in Figure 2.2b. Our structural results are within 5% error of the values found by Demichelis *et al.*: a unit cell length of 4.30 Å (vs 4.26 Å [119]) and a tube diameter of 7.96 Å (vs 7.90 Å [119]). The tube diameter of (10,0)-CNTs was measured by scanning tunneling microscopy to be 7.8 ± 0.7 Å by Odom *et al.* (see Figure 3 of [37]), hence our structural results agree with experimental results. However, our band gap of 0.76 eV deviates from the experimental value of 1.073 eV, measured by Weisman *et al.* via spectrofluorimetry [126]. Demichelis *et al.* observed a similar underestimation of the bandgap of a (10,0)-CNT, with a value of 0.78 eV calculated with the GGA-PBE functional and a 6-1111G(d) basis set with DFT [119]. To properly account for the bandgap value, a hybrid functional considering a fraction of Hartree Fock exchange (such as B3LYP) is needed, which is not available in the

SIESTA package. For this reason, our overall interpretation is based on the relative variations of the properties, which are less sensitive to the absolute values, and should correctly represent general trends.

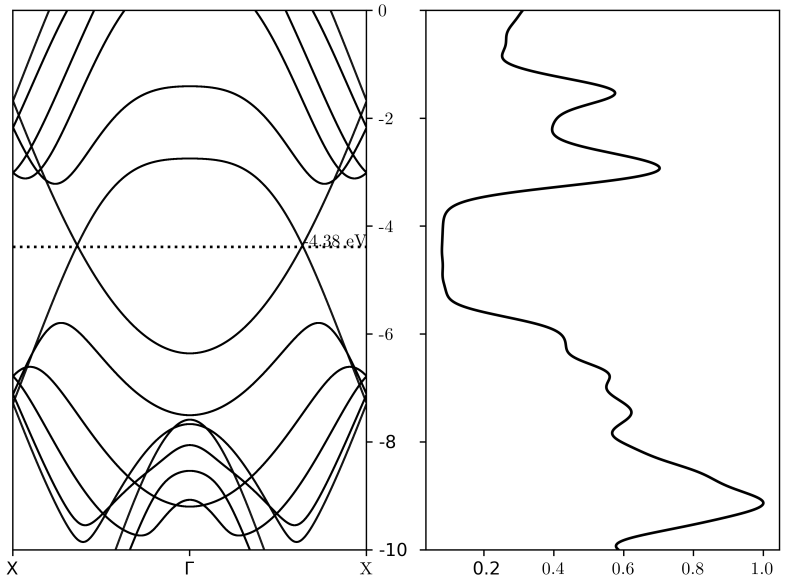

(a) (5,5)-CNT

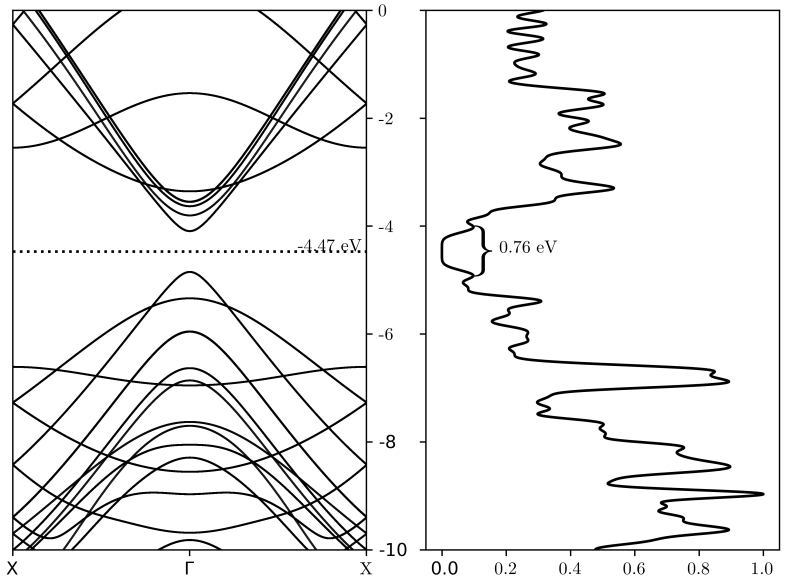

(b) (10,0)-CNT

Figure 4.1 DFT-calculated band structures and DOS of CNTs

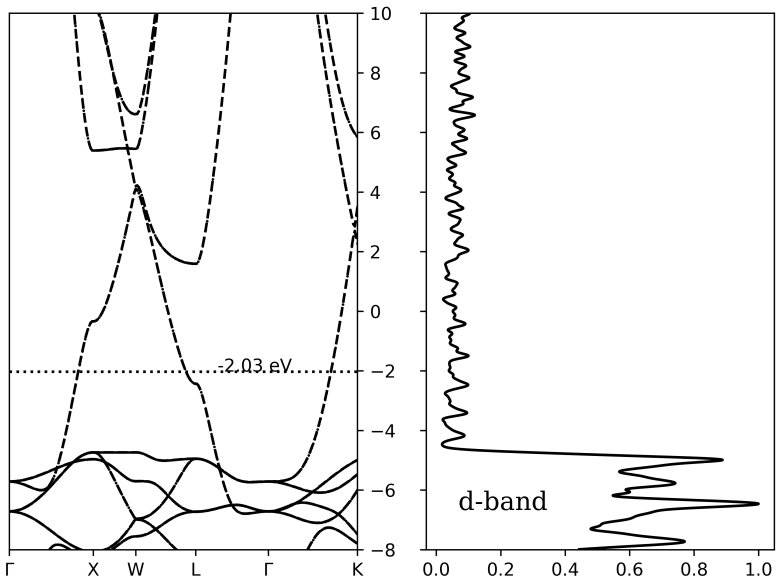

Figure 4.2 DFT-calculated bulk silver band structure and DOS

Silver nanocluster size effects

To study size effects on the AgNCs, we considered clusters with 4, 13, 55, and 147 atoms. The last three models are of icosahedral geometry, and the Ag_4 is a simple tetrahedral model. We also simulated bulk Ag and a Ag(111) slab since the surfaces of the icosahedral particles follow the (111) orientation [51]. The geometry of each icosahedral cluster was optimized within a tolerance of 0.01 eV/Å following the methodology explained in chapter 3. The structure of bulk Ag shows d-band characteristics (see Figure 4.2). Berglund and Spicer measured the presence of such a d-band through photoemission, however they observed the d-band as approximately spanning from 7 to 4 eV below the Fermi level [127]. In our case, the d-band spans from 6 to 3 eV below E_F. A shift of the d-band position has been shown to occur, again by Berglund and Spicer, when calculating the DOS of Ag(111) surfaces using either Hartree (2.2 eV below FL) or Hartree-Fock methods (5.2 eV below FL) [128]. Even though the d-band is fully occupied in the case of silver, it can contribute to the interaction between CNTs and silver. However, since the d-band position does not noticeably shift from one silver system to another (see Figure 4.3a), the error should be systematic for all systems studied. Once again, since our overall interpretation is based on the relative variations of the properties which are less sensitive to the absolute values, the general trends should be preserved.

In addition, the FL of -2.03 eV reported in Figure 4.2 does not correspond to the work function of 4.72 ± 0.02 eV of a Ag(111) surface as measured by Dweydari *et al.* [129]. To

properly take into account the Ag(111) surface work function, it is necessary to shift the FL by taking into account SIESTA's arbitrary positioning of the vacuum electrostatic potential as opposed to the Ag slab. After such a correction, one finds a work function of 4.72 eV for the Ag(111) surface, which corresponds to the experimental value of 4.72 ± 0.02 eV as reported by Dweydari *et al.* [129].

Figure 4.3a shows the PDOS surface atoms for different AgNC sizes in the vicinity of the valence band. As the size of the clusters increases, new peaks appear and broaden the distribution; states are gradually forming electronic bands, the result of which can be seen in the bulk materials surface atom PDOS. The broadening is apparent when observing the amount of states per atom for a given peak diminishing with cluster size. Figure 4.4 shows this variation of occupied states per eV per surface atom (red curve) in the vicinity the FL (HOMO). The number of occupied states per surface atom follows a clear trend towards the bulk surface value; electrons populating the AgNC surface become more energetically diffuse.

However, the trend with respect to cluster size is not trivial regarding the position of the FL and the general DOS characteristics; new surface states appear and former states seem to shift with NC size. With the exception of the Ag_{147}, the FL position seems to follow a general trend similar to the one described above. Furthermore, the work function of 4.72 eV calculated for the Ag(111) slab indicates that the variation of the FL to lower energies would persist until the bulk value; imposing an icosahedral geometry may not be the best choice. Other cluster geometries present different characteristics regarding their chemical potential. In fact, it has been shown that the Ag_{147} cluster tends to relax into a more stable cuboctahedral geometry [2], and naturally presents a higher chemical potential than the icosahedral cluster.

Figure 4.3b shows the PDOS associated with AgNC core atoms, which evolves with a trend similar to the surface atoms: the amount of states per atom diminishes as the AgNC contains more atoms. In addition, the position of the peak below FL moves towards lower energy levels with an increasing number of atoms.

Finally, if one considers the displacement of charges from one layer of atoms to another, it is clear that the charges accumulate on the surface atoms of the cluster (see Table 4.1). The surface layer draws most of its electrons from the adjacent layer. As the AgNC gets bigger, the central core atom becomes less affected, as it is further away from the surface layer. The amount of electron charge per surface atom seems to converge at about 0.036 for silver clusters, however the value for a Ag(111) surface is 0.056 electron charges per atom. The surface layer itself shows a particular charge distribution that depends on the coordination number of the atom. Figure 4.5 shows that the geometrically dominant surface sites hold most of the electron charges. The coloured bars in the histogram plot represent the percentage of

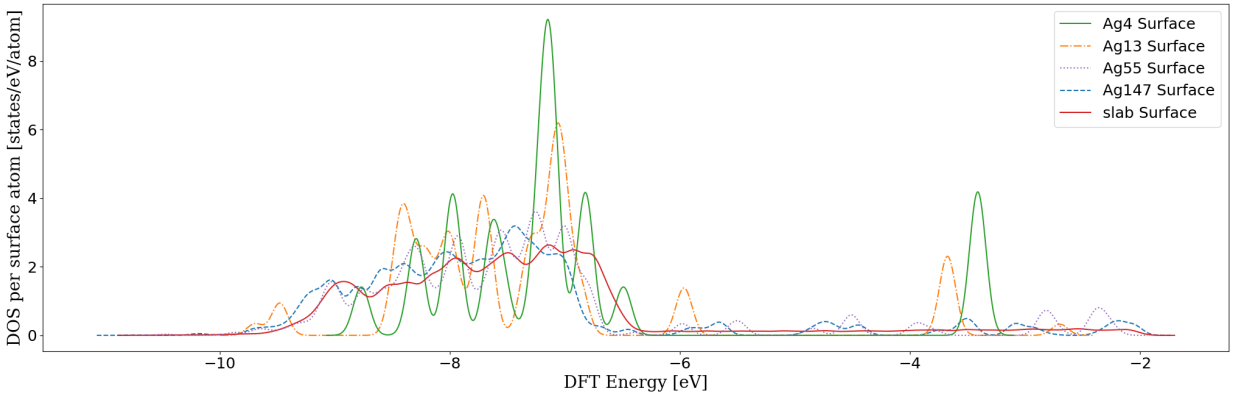

(a) PDOS for surface atoms

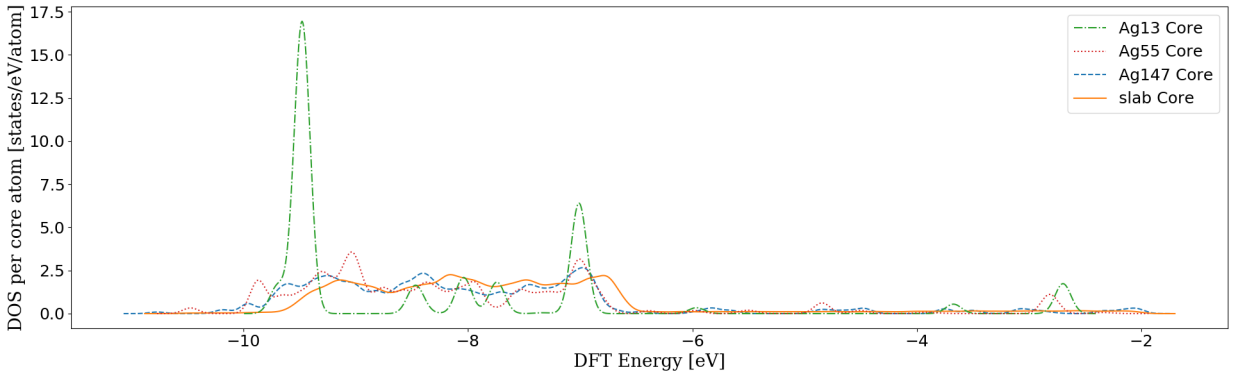

(b) PDOS for core atoms

Figure 4.3 Comparison of the PDOS of core and surface Ag atoms for AgNCs of varying sizes

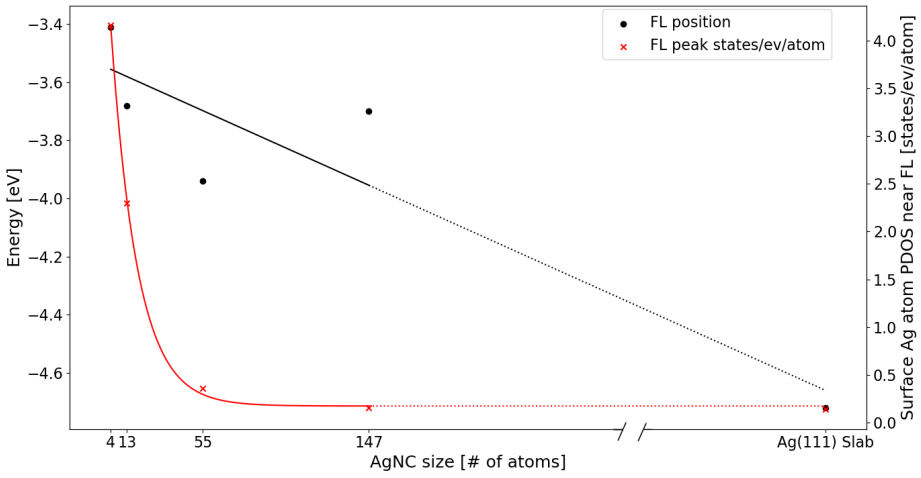

Figure 4.4 Variation of the Fermi level position and of the amount of states near it

charges of the surface layer that is attributed to a group of atoms of a given coordination number. The ball models of the AgNCs present groups of atoms colour-coded depending on their coordination number. The black outlines in the histograms represent the ratio of a certain type of site with respect to the amount of atoms in the surface layer. This shows that the electron charges are uniformly distributed at the surface layer, with small differences that likely arise from its interaction with the adjacent layer.

Table 4.1 Voronoi charge population per cluster layer. Negative (positive) values indicate an electron gain (loss). Values in parentheses are normalized by the amount of atoms considered.

Cluster type	Core Atom	First Layer	Second Layer	Third Layer
Ag_{13}	0.26 (0.26)	-0.26 (-0.022)	NA	NA
Ag_{55}	0.016 (0.016)	1.149 (0.096)	-1.51 (-0.036)	NA
Ag_{147}	0.01 (0.01)	0.07 (0.006)	3.30 (0.079)	-3.38 -(0.037)

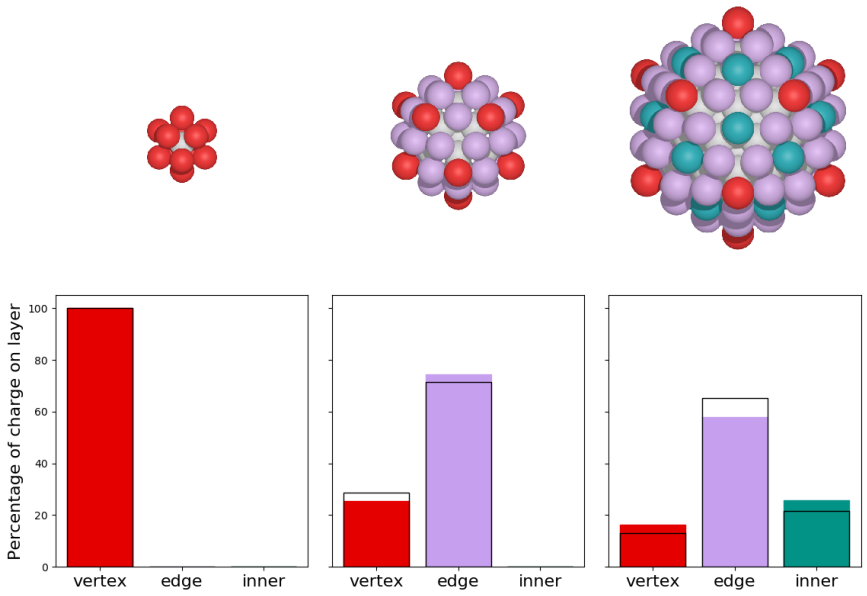

Figure 4.5 Ratio of surface electron charge as a function of the coordination type of surface atoms

4.2 Quantum size effects in the AgNC/CNT system

Regarding the size effect of AgNCs interacting with either a (5,5) or (10,0)-CNT, the most striking difference with isolated cluster electron populations is the loss of a large fraction of

the electron density of the surface atoms. Table 4.2 shows that the inner layers present the same charge migrations as in the isolated case. The only appreciable change occurs at the surface for all AgNC sizes.

Table 4.2 Voronoi charge population per cluster layer for a AgNC/CNT system. Negative (positive) values indicate an electron gain (loss). Values in parentheses are normalized by the amount of atoms considered.

System Type		Core Atom	First Layer	Second Layer	Third Layer
(5,5)	Ag_{13}	0.245 (0.245)	0.016 (0.001)	NA	NA
	Ag_{55}	0.016 (0.016)	1.472 (0.123)	-1.354 (-0.032)	NA
	Ag_{147}	0.012 (0.012)	0.066 (0.006)	3.34 (0.080)	-3.112 (-0.034)
(10,0)	Ag_{13}	0.25 (0.25)	-0.103 (-0.009)	NA	NA
	Ag_{55}	0.017 (0.017)	1.479 (0.123)	-1.52 (-0.036)	NA
	Ag_{147}	0.012 (0.012)	0.067 (0.006)	3.324 (0.079)	-3.317 (-0.036)

Figure 4.6 shows the amount of electrons that migrated to the surface layer sites as defined in Figure 4.5, as well as their distribution. The black outlines in the first row of figures show the amount of electrons attributed to each type of site on the corresponding isolated AgNC. The histogram shows the populations of surface atoms harbouring a change in electrons within regular intervals. The interaction of the Ag_{13} with the (5,5) and (10,0) CNTs is characterized by the loss of electron charges that were previously accumulated on the surface of the cluster. Upon contact with a (5,5)-CNT, the surface electron charge on the Ag_{13} is completely drained and then injected into the CNT. The fluctuation of the surface electron charge density is less pronounced in the case of Ag_{13} in contact with a (10,0)-CNT. The distribution of the electron charges on the surface of the NC goes from a uniform distribution (in the case of isolated Ag_{13}) to a broader and more heterogeneous distribution around 0 (in the case of Ag_{13}/CNT complexes), regardless of the CNT. This charge redistribution becomes apparent with the charge differential isovalue plots used in the 3D visualization of the Ag_{13}/CNT complexes (see Figure 4.7). In these plots, the red colour indicates a gain of electron charges while the blue colour is representative of a loss of electron charges. The cross-sections in the right panels also show a charge accumulation between Ag_{13} and the CNTs, indicating the formation of a bond.

A similar picture can be drawn for larger particles but where the charge redistribution occurs to a lesser extent. The corresponding figures are shown in Appendix A.

To complete this study of the quantum size offects of AgNCs, we compare the adsorption energies of the AgNCs to the CNTs to the magnitude of the charge transfer in Figure 4.8.

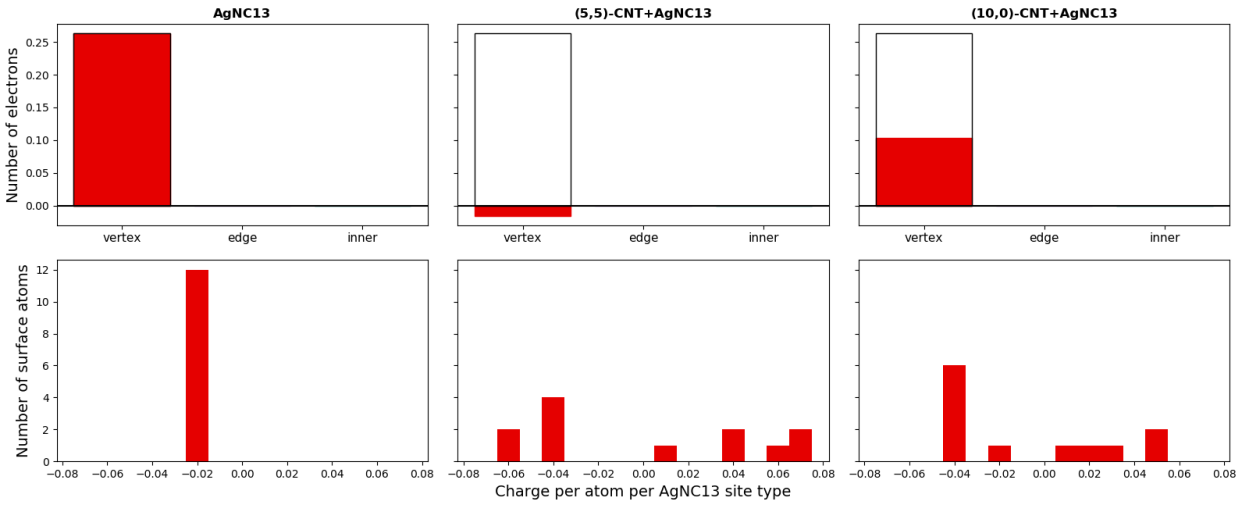

Figure 4.6 Charge transfer populations of Ag_{13} when isolated, when interacting with a (5,5)-CNT, and when interacting with a (10,0)-CNT. The first row shows the charge present on the vertex atoms, and the black outline represents the isolated case. The bottom row shows the how the charge is shared between the atoms of the silver cluster.

Here we consider both the charge transfer (dashed lines) and adsorption energies (solid lines) for AgNCs with 4, 13, 55, and 147 atoms. The results for an infinite interface between CNT and Ag(111) slab are also presented to provide a bulk-like reference. To be able to compare all systems on an equal footing, the values presented in Figure 4.8 are scaled by the amount of Ag surface atoms at the interface.

The trends for both the CNT-type systems are extremely similar. First, charge transfer is more pronounced with the (5,5)-CNT, as described earlier, with the highest values found for the smaller AgNCs. Charge transfer from the Ag_{55} is the lowest: the Ag_{55} donates a small fraction of electrons to the (5,5)-CNT (0.03 electrons per interface atom), while a small donation (0.004 electrons per interface atom) occurs from the (10,0)-CNT to the cluster. Ag_{147} donates a more important amount of electron charge than the Ag_{55} (0.04 and 0.01 electrons per interface atom for (5,5) and (10,0) CNTs). Finally, the charge transfer to the Ag(111) slab is practically null, which is in agreement with previous works on Ag(111)-CNT systems [44, 87].

The trend for adsorption energy per interface Ag atom is similar in that it is the strongest for smaller clusters. The adsorption of AgNCs to the (5,5)-CNT is consistently stronger than to the (10,0)-CNT. The calculated adsorption energy of 0.68 eV for the Ag(111) slab is higher than the value of 0.26 eV previously found for a (10,10)-CNT [44], possibly due to the higher electronic density outside the tube due to the constraints to the π-orbitals and subsequent

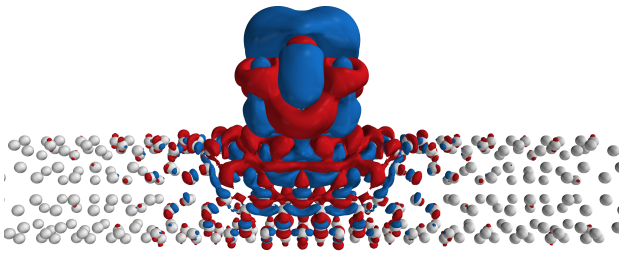

(a) Ag_{13}/(5,5)-CNT

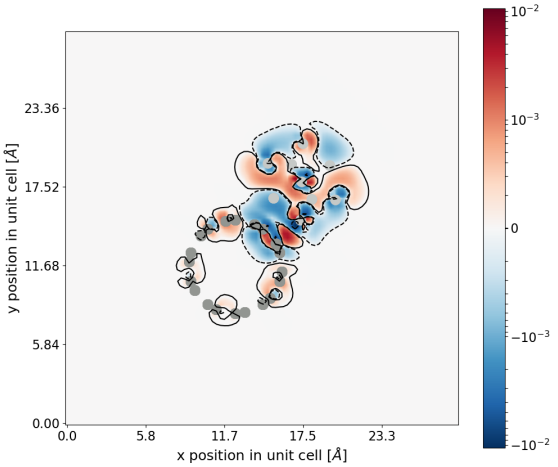

(b) Ag_{13}/(5,5)-CNT cross-section

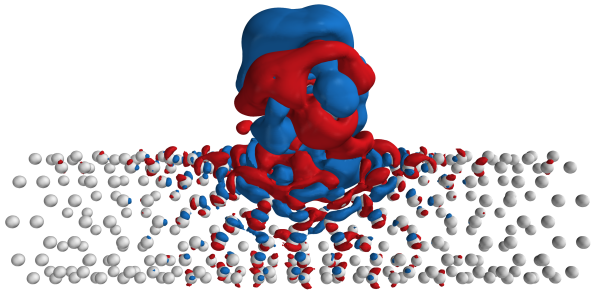

(c) Ag_{13}/(10,0)-CNT

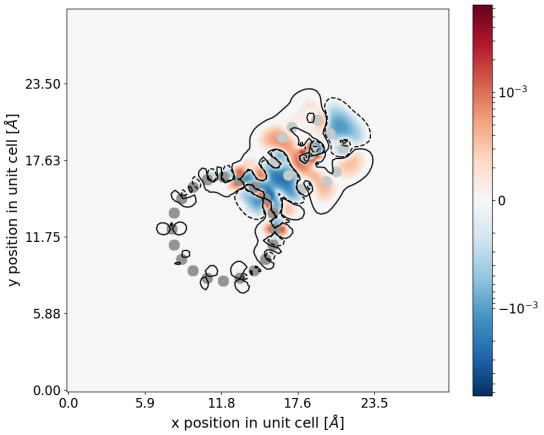

(d) Ag_{13}/(10,0)-CNT cross-section

Figure 4.7 Differential charge density of the Ag_{13}/CNT systems at ± $1.5{\cdot}10^{-5}$ electrons/Å^3 (a,c) and corresponding cross-sections (b,d)

improved sp^3 hybridization imposed by the higher CNT curvature. The high curvature of the (5,5)-CNT would thus explain the higher adsorption energy with respect to the (10,10)-CNT, in agreement with similar results reported in the literature [28].

To summarize, smaller clusters interact more strongly with CNTs: there is more electron charge per interface atom transferred to the CNT than for large AgNCs, and the resulting adsorption energy is higher. Small AgNCs can thus be said to be more reactive; a finding that has been reported in many studies on metallic nanoclusters [51]. The overall magnitude of electron the CNTs is decreasing with the size of the AgNCs, and gradually converges towards the behaviour of the bulk material. The deviation from this general trend has been attributed

to the fact that the shape of the clusters was imposed (icosahedral), and conditioned in this way the distribution of the different surface sites.

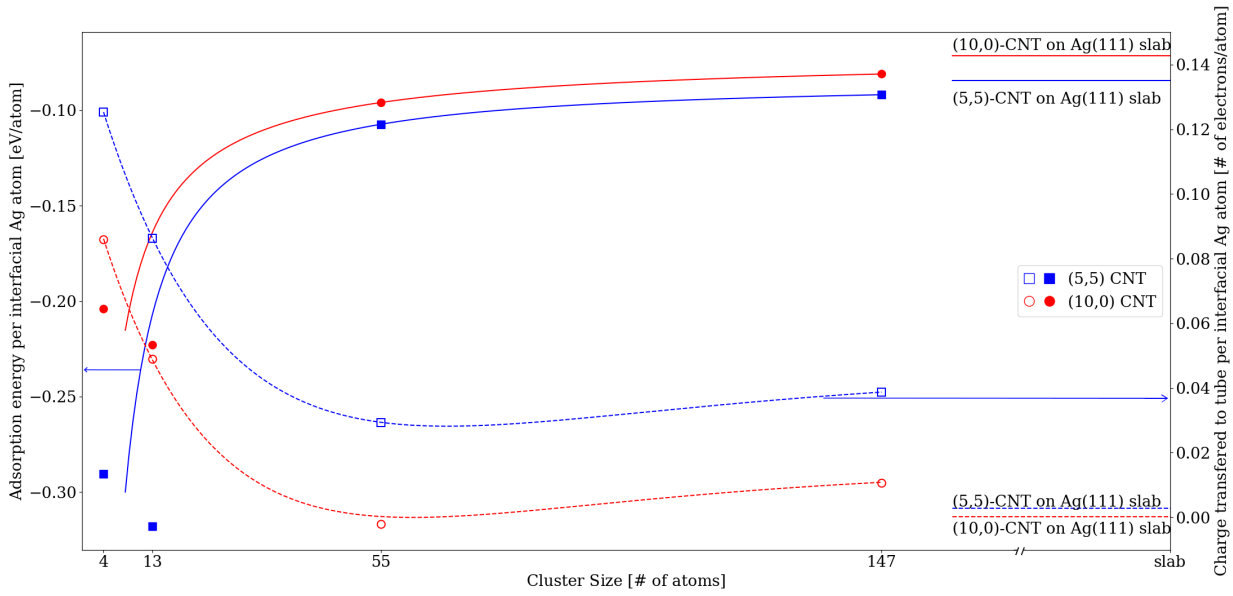

Figure 4.8 Variation of the calculated adsorption energy and charge transfer of AgNCs interacting with either (5,5)- or (10,0)-CNTs versus silver cluster size. Values for the interaction of (5,5)- and (10,0)-CNTs with Ag(111) surfaces are presented as horizontal bars.

Chemical Analysis

To better understand the changes observed in the adsorption and charge transfer characteristics, it is of interest to analyze the effect of AgNC adsorption on the DOS. Figure 4.9 regroups all of the results related to Ag clusters interacting with the (5,5)- and (10,0)-CNTs. Each panel on the left side of the figure compares the DOS of pristine CNTs to PDOS(C) of the AgNC/CNT system. The right side panels superpose the DOS of the surface atoms of isolated AgNCs to the PDOS(Ag) of surface atoms of the cluster when adsorbed on the CNT. The results for the (10,0)-CNT are reported in panels (a), (c), and (f) while the results for the (5,5)-CNT are shown in the panels (b), (d), and (e). All the DOS are scaled in order to represent the correct relative differences in height. The energy scale is centered around the Fermi level of the AgNC/CNT complex, and is set at $E_F = 0$ eV.

The modification of the AgNC surface states depends on the size of the cluster :

– The Ag_{13} surface states near E_F for the isolated Ag_{13} (HOMO) split into two populations. A fraction is pinned at the FL of the Ag_{13}/CNT complex, while the remaining fraction

is very little modified from their initial energy position.

– The large clusters do not present such a splitting of the HOMO. They exhibit a rigid shift in energy positions of those electronic states. It is worth noting that the Ag_{55} states near E_F are not strongly perturbed when the particle is in contact with the (10,0)-CNT. The result is coherent with the little charge transfer previously observed in Figure 4.8.

There is a clear difference in the behaviour of clusters smaller than 20 Ag atoms and larger clusters. The PDOS(Ag) of surface atoms show that small clusters undergo chemisorption whilst larger clusters are physisorbed. Such an effect is generally not taken into account in the classification of particles when observing isolated systems, as seen in other works [53, 62, 63]. We have however shown that the amount of electron charge per surface atom reaches a plateau with clusters of 55 Ag atoms.

The PDOS(C) of AgNC/CNT systems do not give a clear indication of size effects as it was the case for the PDOS(Ag) of surface atoms of the same systems. In all cases there is an injection of electrons near the FL. In the (10,0)-CNT case, all interactions with AgNCs seem somewhat similar, with states populated in the conduction band edge. The (10,0)-CNT/Ag_{55} system presents a populated conduction band-edge without charge transfer to the CNT, showcasing the complex nature of the interaction between CNTs and AgNCs. The interaction between AgNC and (10,0)-CNT is accompanied in all cases by the appearance of MIGS, as we will see in the following section.

The variation of the FL for all systems are presented in Figure 4.10. The shifts are calculated as follows:

$$\Delta(E_F)^{component} = E_F^{joint\ \ system} - E_F^{isolated\ \ component} \tag{4.1}$$

Positive values of ΔE_F are reminiscent of an electron gain, while negative values are associated with an electron loss. As it can be seen in Figure 4.10, this would suggest that all CNTs are acceptors, which is not totally consistent with our previous charge transfer analysis. The main issue arises for the (10,0)-CNT/Ag_{55} complex. For this system we observed a small electron charge donation from the (10,0)-CNT to the Ag_{55}. Another inconsistency is that the FL shifts for the (10,0)-CNT are greater than for the (5,5)-CNT. To remedy this, we can modify Equation 4.1 for the semiconducting nanotubes. We need to correct the position of E_F that is arbitrarily defined at midgap in the SIESTA software. The CNL is not necessarily placed at midgap for semiconductors [73, 74]. Given that the Ag_{55}/(10,0)-CNT accommodates states near the conduction band minimum (CBM), without any strong interaction, it is appropriate to set E_F for pristine (10,0)-CNTs near the CBM. With this correction, one finds a general

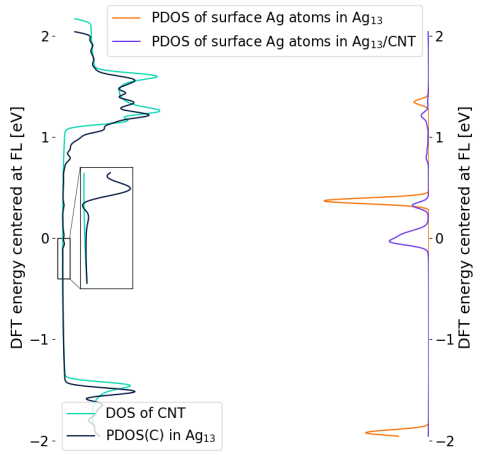

(a) Ag_{13}/(5,5)-CNT

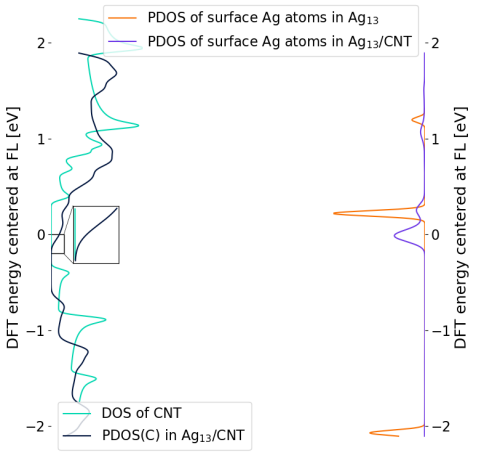

(b) Ag_{13}/(10,0)-CNT

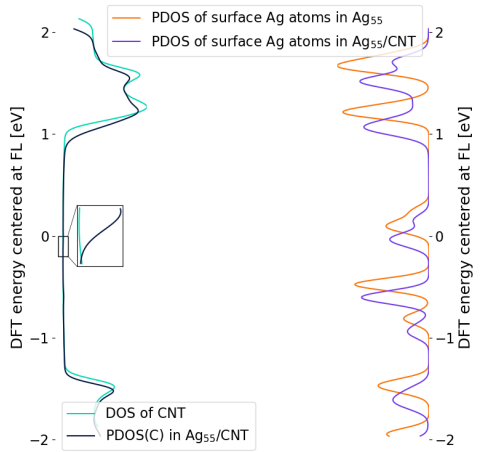

(c) Ag_{55}/(5,5)-CNT

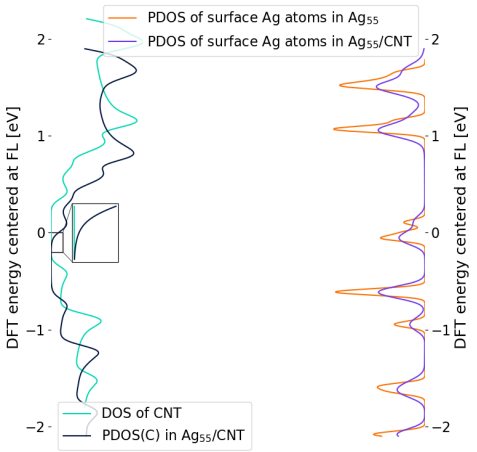

(d) Ag_{55}/(10,0)-CNT

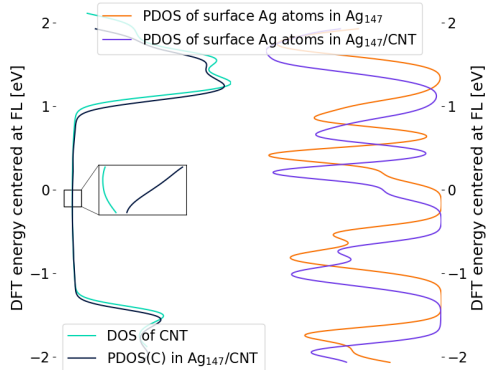

(e) Ag_{147}/(5,5)-CNT

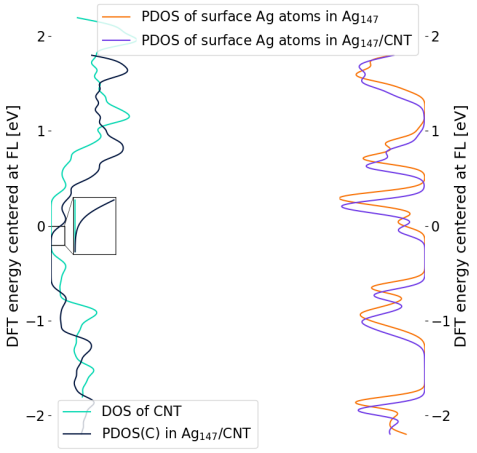

(f) Ag_{147}/(10,0)-CNT

Figure 4.9 Comparison between the DOS of isolated system components with their PDOS when in contact. The Fermi level of the complexes is set at 0 eV for all subfigures. The insets shows a close-up of the states near Fermi level.

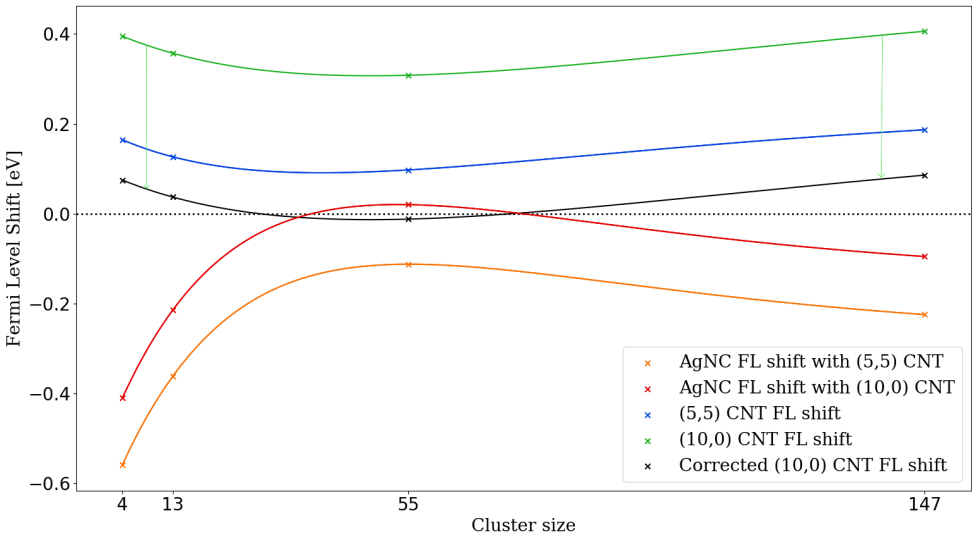

Figure 4.10 Fermi level shift for the AgNCs and the CNTs. The green arrows represent the correction due to setting the CNL near CBM.

trend in the FL shift trend for (10,0)-CNT/AgNC systems that is represented by the black line in Figure 4.10, and the behaviour described in the charge transfer analysis is now fully respected.

To describe the variation of the Fermi energy of a system, for example to evaluate the variation of the work function of a metal slab on which a CNT [87] or a graphene sheet [82] is adsorbed, descriptive models tend to start from the band line-up picture and build from there. In the current case, we are considering AgNCs adsorbed on CNTs, so the variation that we will monitor is directly related to the CNT. Using the CNTs as a reference, the simple band line-up model is:

$$\Delta E_F^{CNT} = E_F^{CNT} - E_F^{AgNC} + \Delta V \tag{4.2}$$

For the (5,5)-CNT we directly used the FL obtained from SIESTA, and we modified E_F for the (10,0)-CNT as described above, by setting the Fermi energy at the CBM. Here, ΔV corresponds to the electrostatically-driven energy variations, which can be attributed to variations due to charge transfer (ΔV_{tr}) and charge rearrangement (ΔV_C) [87, 82]:

$$\Delta V = \Delta V_{tr} + \Delta V_C$$

It is difficult to separate the contribution of charge rearrangement from the charge transfer for

localized interfaces of CNT/AgNCs. Simple system geometries provide obvious approximations that can be used to describe the electrostatic contribution of the charge transfer. For example, with graphene adsorbed on a metal surface, a plane capacitor model has been shown to be a good approximation for ΔV_{tr}, allowing for a fitted parametrized model to capture the charge rearrangement contribution [82]. In the case of infinite contacts between CNTs and metal surfaces, a Lagrangian optimization technique has also been used to separate the electrostatic contributions [87].

Given the complex interface geometries that need to be captured in our models, we will simply verify whether a model following Equation 4.2 is applicable to our systems. To this end, we defined ΔV by using the position dependant electrostatic potential of the system. We chose to sample the electrostatic potential along segments parallel to the CNT-axis. On a given segment, we define ΔV_{SIESTA} as the difference between the absolute extrema in the electrostatic potential along a segment, under the constraint that the positions that are sampled are occupied by a minimum amount of charge density:

$$\begin{cases} \Delta V_{SIESTA} & = \max\{V(\mathbf{r})\}_{complex} - \min\{V(\mathbf{r})\}_{complex} \\ \rho(\mathbf{r}) & > 10^{-5}\text{electrons} \cdot \text{Å}^{-3} \end{cases} \tag{4.3}$$

We have taken care in including the neutral atom contributions as to side-step the arbitrary vacuum energy positioning in SIESTA calculations. By doing so, we put all electrostatic potential contributions on an equal footing. To compare this idea to the band lineup picture we need a reference, which is calculated combining Equation 4.2 and Equation 4.1:

$$\begin{aligned} \Delta V &= \Delta E_F^{CNT} - (E_F^{CNT} - E_F^{AgNC}) \\ &= E_F^{joint\ \ system} - E_F^{CNT} - (E_F^{CNT} - E_F^{AgNC}) \\ &= E_F^{joint\ \ system} - 2E_F^{CNT} + E_F^{AgNC} \end{aligned}$$

We can now define a relative error between ΔV and ΔV_{SIESTA}:

$$\epsilon = \frac{\Delta V - \Delta V_{SIESTA}}{\Delta V} \tag{4.4}$$

In Figure 4.11, we have plotted the segments along which the error defined by Equation 4.4 is less than 5% for the CNT/Ag_{13} systems. The contours for the other systems are presented in

Appendix B. We found that the applicability of Equation 4.2 is confined to a set of segments forming a contour.

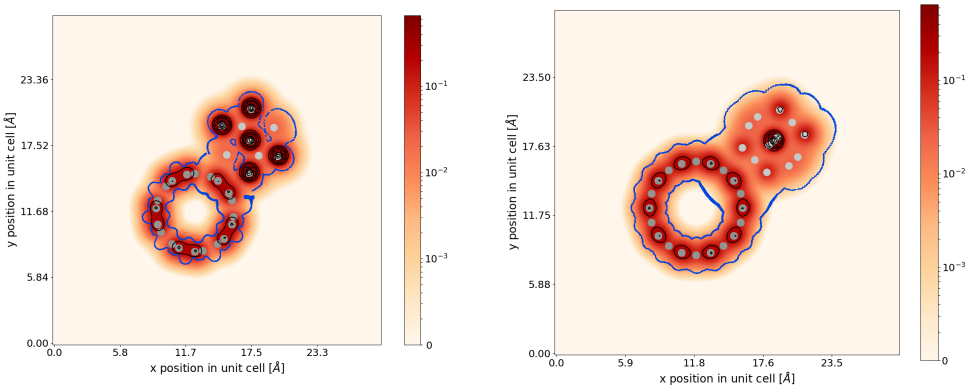

(a) (5,5)-CNT / Ag_{13} (b) (10,0)-CNT / Ag_{13}

Figure 4.11 The charge density and profile of lines (blue) along the CNT-axis that fit within the band line-up picture. The colour map represents the charge density of the system in electron charges/$Å^3$.

How does this information help us understand these systems? We now know that there is a set of segments along which the band line-up picture is applicable. This set of lines defines a contour around the system components. This in turn points to the existence of a potential barrier, or a Schottky barrier in the case of the semiconducting CNT, that can be spatially defined between the cluster and the CNT. Archambault and Rochefort have used a similar method, although sampling with a plane, to find the electrostatic term in the band line-up description of graphene nanoribbons on different metal surfaces [130]. This provides a good starting point for further quantitative investigations regarding the separation of electrostatic contributions of charge transfer and charge rearrangement. For example, an approximation for ΔV_{tr} along this contour could be proposed to then find the ratio $\Delta V_{tr}/\Delta V_{ch}$, which could be used as a metric to classify CNT/AgNC interactions. In our case, this could also help define an explicit interface between cluster and CNT since the contour is spatially well defined.

Charge rearrangement

Instead of studying the charge rearrangement through its electrostatic contribution to the band line-up picture, we will instead consider its spatial distribution. First, we need to evaluate the variations in charge density ($\Delta\rho$) when a AgNC/CNT complex is formed:

$$\Delta\rho = \rho_{complex} - \rho_{CNT} - \rho_{AgNC} \tag{4.5}$$

To visualize and quantify the extent of the charge distribution along the CNT, we plot the sum of $\Delta\rho$ along a series of disks centered around the tube axis, with radii reaching halfway between the CNT surface and the closest Ag atoms. By sectioning the unit cell this way, we can plot the variation of $\Delta\rho$ along the CNT axis. Figure 4.12 shows the result of such discretisation for all AgNC/CNT complexes. We fit the peaks of the calculated data (black crosses) with the help of a simple exponential function:

$$\exp(z) = D_0 \cdot \exp(-\alpha(z - z_0)) + c \tag{4.6}$$

Here, D_0 is a constant to take into account the initial amplitude of the exponential near the interface. This parameter can be compared to the pinning strength used by Léonard and Tersoff [6], who find that additional charge distribution (e.g. by doping) along semi-conducting CNTs exhibit an exponential decay, with a long tail. z_0 allows us to shift the exponential to start at the right point, and α is the decay rate of the exponential. Decay lengths correspond to the inverse of the decay rate. Finally, c is a baseline constant, that is specifically chosen to match the exponential fits on either side of the interface in order to agree with the periodicity of the unit-cell along the CNT-axis.

The resulting fits are presented in Figure 4.12. At first glance, the systems composed of (5,5)-CNTs present a variation of electron charge distribution that is more symmetric than for (10,0)-CNT based systems. This behaviour is partly due to the underlying geometry of the CNT and how the on-top configuration of the AgNCs differs between armchair and zigzag CNTs. The positions of Ag atoms near the (10,0)-CNT are not homogeneous as for the (5,5)-CNT. For example, in the case of the (10,0)-CNT/Ag_{13} system, one side of the interface has 2 Ag atoms whilst the other side has only one. This can be seen in the representation of interface atom positions as coloured circles in Figure 4.12. An explicit representation of the interface in the case of Ag13 is shown in Figure 4.13. Another reason for this difference in charge redistribution along the CNT is the electronic character of the CNT. For metallic CNTs, the energy dispersion in k-space easily accommodates new electronic energy states in a uniform fashion simply because there are more states around E_F. For (10,0)-CNTs, the band-gap makes things a little more complicated. As shown earlier, MIGS decay exponentially into the (10,0)-CNT [73, 130, 131]. Furthermore, the decay rate depends on the position of the MIGS in the bandgap. This fact could be the reason why the exponential fits for the (10,0)-CNT/AgNC systems are not totally satisfying.

The (5,5)-CNT systems have a shorter decay length for Ag_{13} than for large clusters (Ag_{55}/Ag_{147}). The two last clusters are also further away from the CNT than for the small clusters (see Figure 4.15b). It is important to note that two length scales are at work in the redistribution

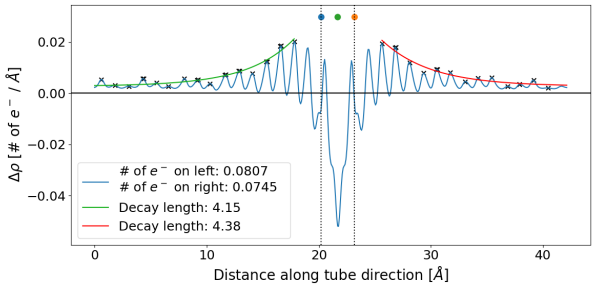

(a) $\Delta\rho$ for Ag_{13} adsorbed on a (5,5)-CNT

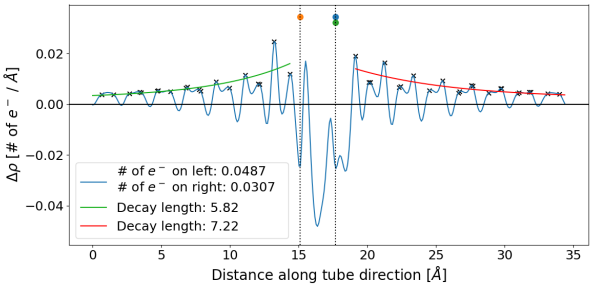

(b) $\Delta\rho$ for Ag_{13} adsorbed on a (10,0)-CNT

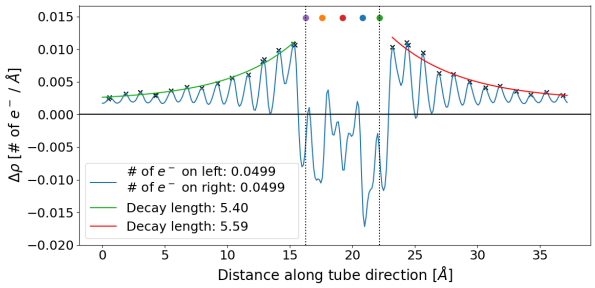

(c) $\Delta\rho$ for Ag_{55} adsorbed on a (5,5)-CNT

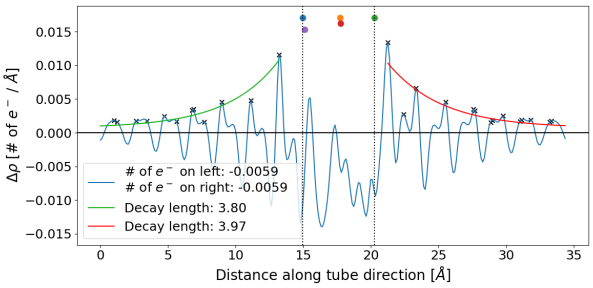

(d) $\Delta\rho$ for Ag_{55} adsorbed on a (10,0)-CNT

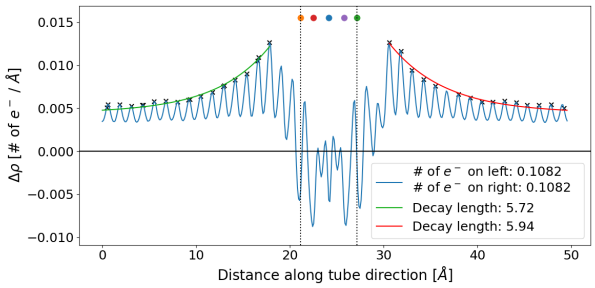

(e) $\Delta\rho$ for Ag_{147} adsorbed on a (5,5)-CNT

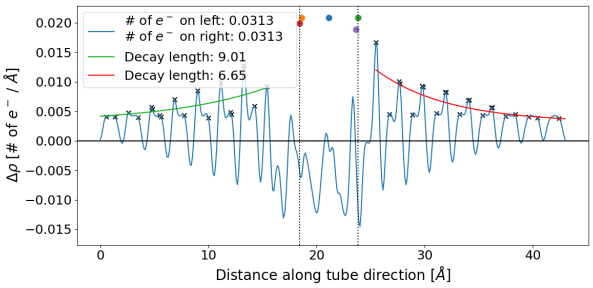

(f) $\Delta\rho$ for Ag_{147} adsorbed on a (10,0)-CNT

Figure 4.12 $\Delta\rho$ along CNT axis for CNT+Ag_{13}/Ag_{55}/Ag_{147} systems. Vertical dotted lines represent the edges of the interfacial Ag atoms. Coloured circles represent interfacial Ag atoms. Black crosses are the points used for the exponential fits.

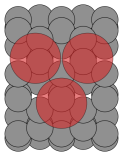

(a) (5,5)-CNT / Ag_{13}

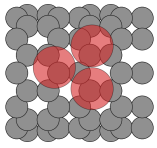

(b) (10,0)-CNT / Ag_{13}

Figure 4.13 The interface of the Ag_{13}/(5,5)|(10,0)-CNT systems

of electronic charge. A short exponential decay of the charge redistribution occurs from the interface, but there also exists a slower decay rate. As we have seen before, the unit cell length was chosen to assure as little influence on the AgNC by its periodic images. This large length scale (25 Å), first discussed by Léonard and Tersoff, has a much slower logarithmic decay tail than the sharp changes near the interface [7].

Now, since the decay rate of states along the (10,0)-CNT depends on their energy range, let us look into the decay rate of LDOS(E) summed over a disk of radius $r = 4.5$ Å along the CNT:

$$\mathrm{LDOS}_{E_1}^{E_2} = \int_0^z \mathrm{d}z (2\pi \int_0^{4.5} \mathrm{d}r) \int_{E_1}^{E_2} \mathrm{d}E \ \mathrm{LDOS}_E(\mathbf{r}) \tag{4.7}$$

Figure 4.14 shows the result of fitting exponential functions such as Equation 4.6 to the integrated LDOS for different energy ranges. The error bars show the error estimated by a Jacobian approximation to the Hessian of the least squares objective function used for the fit [132]. We can see that each case presents very different characteristics.

Starting with the (10,0)-CNT/Ag_{13} system, where we observe practically no states near the valence band edge. This makes sense considering that the exponential decay rate is equal to 0, showing a very uniform spreading of the states. Beyond midgap, one side shows a stronger decay rate than the other; the rapidly decaying side corresponds to the case where there are two interface atoms. Finally, near E_F the decay rate of the states on either side of the cluster is about the same.

In the case of the (10,0)-CNT/Ag_{55} system, MIGS appear near the valence band edge. This also makes sense when considering that the surface atoms of the cluster present a peak of states at that energy range (see Figure 4.9d). The decay rate is about the same on either side of the cluster, and it decreases to about 0.2 $Å^{-1}$ beyond midgap. Finally, for the (10,0)-CNT/Ag_{147} system, there MIGS appear near the valence band edge, however the decay rate is rather low, but reaches about 0.15 $Å^{-1}$ beyond midgap. For all these systems we do observe a distinct shift of exponential decay rate at around midgap. We still do not have a clear explanation for this behaviour. It is however quite striking how the behaviour of Ag_{13} is different from Ag_{55} and Ag_{147}, which could be related to the observation that large clusters are physisorbed, ans small clusters are chemisorbed.

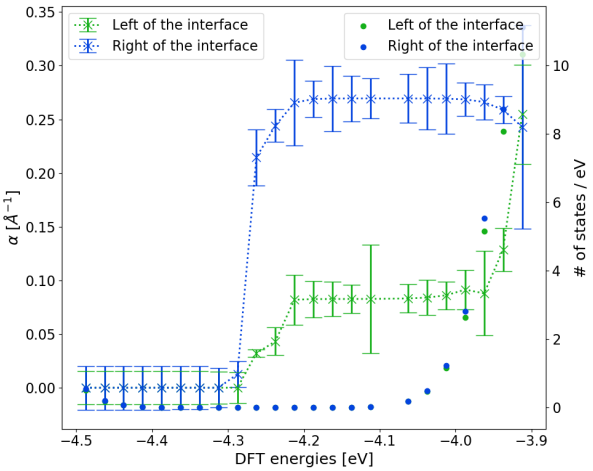

(a) (10,0)-CNT/Ag_{13}

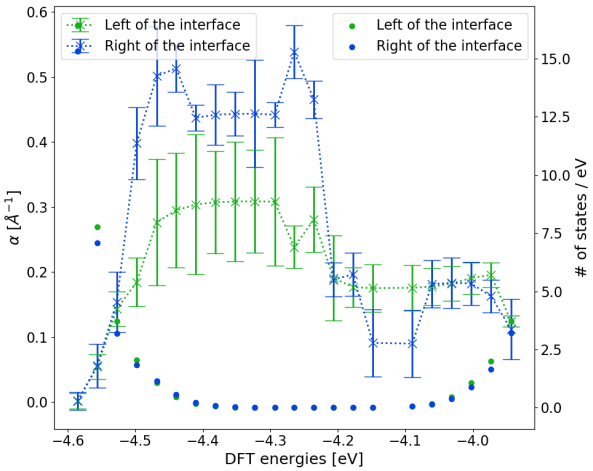

(b) (10,0)-CNT/Ag_{55}

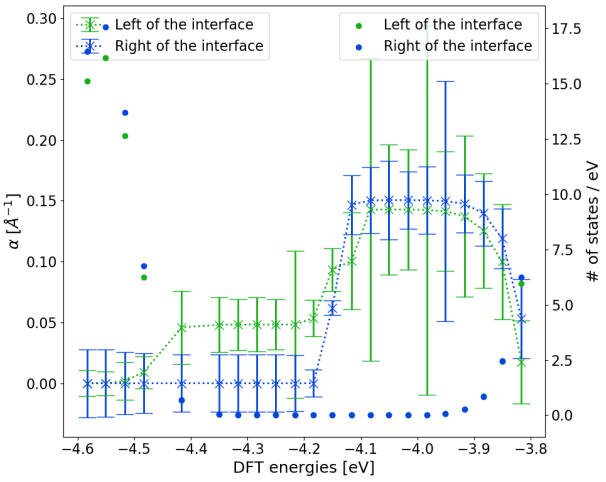

(c) (10,0)-CNT/Ag_{147}

Figure 4.14 DOS and energy-dependant decay rate of $\mathrm{LDOS}_{E_1}^{E_2}$

4.3 Influence of CO adsorption on the AgNC/CNT interface

How does the adsorption of CO on the metallic cluster modify the electronic properties of the AgNC/CNT interface? First, it is known that the most stable adsorption site on the icosahedral cluster is the hollow site [104]. We therefore focus on such high coordination sites for CO adsorption. Figure 4.15 shows (a) the charge transfer and the adsorption energies along with (b) the AgNC-CO and the C-O distance with respect to cluster size. The values corresponding to the interaction of CO with a Ag(111) surface are also included (horizontal lines) for reference. In all quantities studied, we can describe the variations with a simple linear trend with respect to cluster size. With an increasing cluster size we observe that less charge is transferred to CO, and the bonding strength diminishes as well. In turn, the CO-AgNC equilibrium distance becomes larger, and so the back-donation to the CO diminishes which results in a shorter CO bond length. The interaction of the Ag_{55} with CO is the most similar to the interaction between CO and a Ag(111) surface. The stability of the magic-numbered icosahedral Ag_{55} could be the reason for these similarities [56].

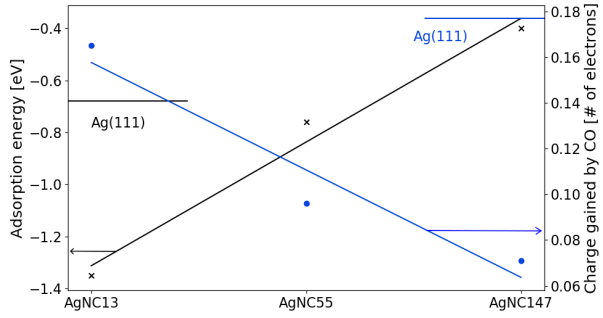

(a) Adsorption energy and charge transfer

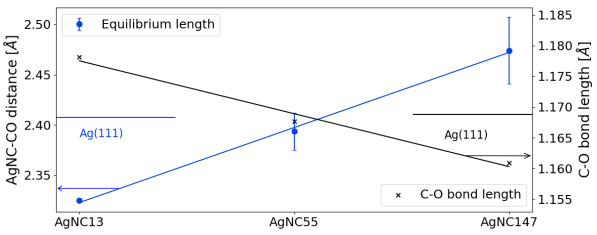

(b) AgNC-CO and C-O distance

Figure 4.15 Interaction of CO with $Ag_{13}/Ag_{55}/Ag_{147}$. The CO adsorption sites are chosen as far as possible from cluster face edges.

In order to describe the influence of CO on the electronic properties of the AgNC/CNT inteface, we will compare three different CO adsorption sites on Ag_{13} and Ag_{55} adsorbed on either (5,5)- or (10,0)-CNTs. The different hollow sites considered for CO adsorption on the AgNC are schematically represented in Figure 4.16. The positions were specifically chosen as to vary the direction of the dipole moment induced by the CO adsorption. The influence of CO adsorption on the adhesion of the AgNCs on the CNTs, the magnitude of the charge transfer, and the resulting dipole moment are summarized in Figure 4.17. The different colours used in the histograms refer to the CO adsorption sites presented in Figure 4.16.

(a) Ag_{13}

(b) Ag_{55}

Figure 4.16 CO adsorption positions used for Ag_{13} and Ag_{55} on CNTs

If we first consider the effects of CO adsorption on Ag_{13}/CNT systems, Figure 4.17a clearly shows that the magnitude of charge transfer to the CNT decreases, no matter the CO adsorption site, nor the electronic character of the CNT. The charge distribution along the CNT does not significantly change between these cases either. The adsorption energy, calculated as:

$$E_{ads} = E_{CO/AgNC/CNT} - E_{CO/AgNC} - E_{CNT}$$

shows that the adsorption of CO weakens the interaction of the particle with the CNT. This result would translate into a less stable system where the AgNC are weakly bound to the CNT, and thus become more mobile.

In the case of Ag_{55}/(5,5)-CNT systems, the magnitude of the charge transfer decreases in all cases except for the side adsorption configuration, where a larger amount of electron charge is transferred to the (5,5)-CNT. Nevertheless, the surplus is very small, and the dipole moment reported in Figure 4.17b remains virtually unchanged. This suggests that CO adsorption in the side configuration induces very few changes. As observed for the Ag_{13} cluster, the Ag_{55} becomes more weakly bound the the CNT when CO is adsorbed on the particle. For Ag_{55}/(10,0)-CNT systems an amount of electron charge is transferred from the CNT to the Ag cluster in absence of CO. CO adsorption seemingly changes the amount of accumulated charge that the CNT donates; when CO adsorbs in a side configuration, the CNT goes from being p-doped to being slightly n-doped! Furthermore, looking at the dipole information in Figure 4.17b, one can see that its norm changes significantly. CO changes both the charge transfer and the charge rearrangement. It is difficult to argue whether or not the modification induced by the CO could be measured in a real device, since a transport calculation is necessary to properly assess such properties [16], notwithstanding the fact that devices present much larger clusters than the ones studied here [133, 15]. Furthermore, given that Ag_{55}/(10,0)-CNT interaction is relatively small, clusters will be nearly free to diffuse among any complex media made of carbon nanotubes, and this particle mobility will be

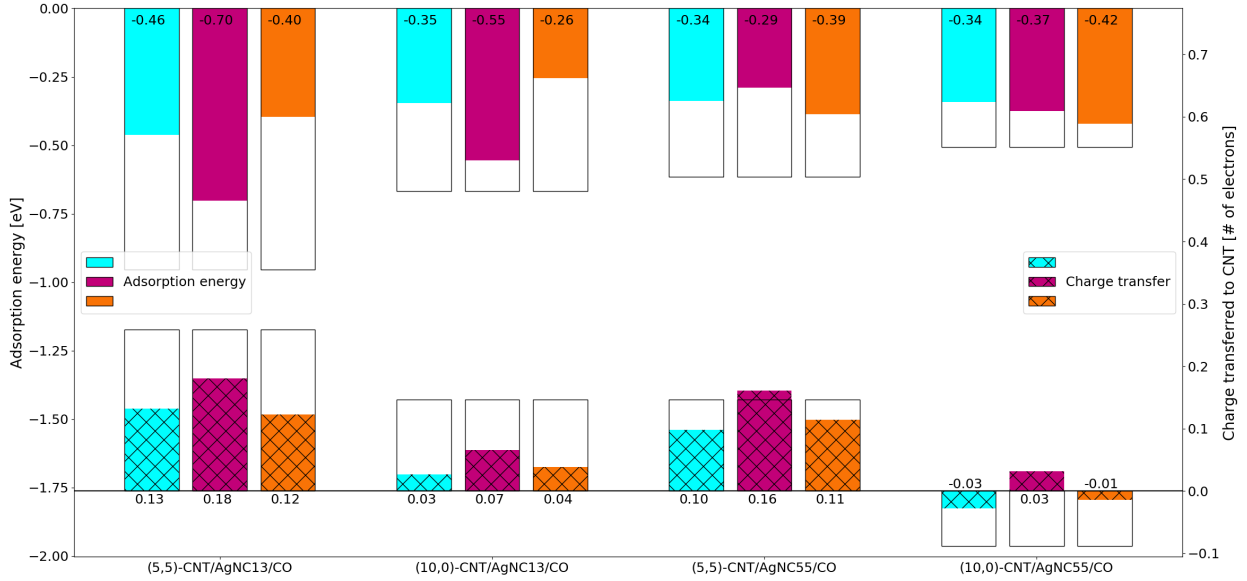

(a) Adsorption energy and charge transfer

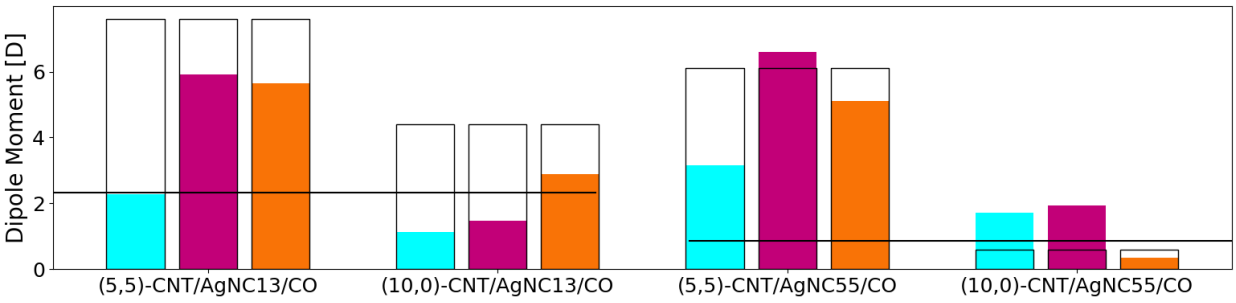

(b) Dipole Moments. The black lines represent the dipole moments of the isolated AgNCs with CO adsorbed on them.

Figure 4.17 Adsorption site dependence of CO interaction with $(Ag_{13}|Ag_{55})/((5,5)|(10,0)$-CNT). The cyan colour bars represent the CO adsorption sites furthest away from the interface. The magenta colour bars represent those that are on the side of the clusters. The orange colour bars represent those that are closest to the interface.

enhanced in the presence of CO.

To summarize, the adsorption of CO on AgNCs modifies the bonding energy and the magnitude of charge transfer to or from the CNT. The Ag_{13} or Ag_{55} particles on CNTs would move more freely in the medium upon CO adsorption. This could facilitate the agglomeration of the AgNCs and contribute to degrade sensor performance.

How do these results impact the potential application of AgNC/CNT networks as gas sensors? More specifically, how do AgNC size effects impact CO sensitivity? Let's retrace the way these sensors work. First off, the way a sensor works is through conductivity changes in the network. The conductivity of the network depends on the conductivity of the constituent CNTs. When metallic nanoclusters are deposited on such networks, the conductivity is improved, due to an additional electron charge available to the CNTs [25, 134]. The modification of the charge transfer from the clusters to the CNTs when CO is adsorbed brings about a change in the network conductivity. The larger the relative variation is, the more sensitive the sensing mechanism. We have seen that smaller clusters present both a larger charge transfer without CO, and a larger relative variation of charge transfer when CO is adsorbed on the cluster. This means that networks with smaller clusters will be more sensitive to low concentrations of CO. Larger clusters do not present as strong a relative charge transfer variation, and so are less intersting for sensor applications. It is clear from Figure 4.17a that the variation of charge transfer to the CNT is stronger when using Ag_{13}. This is due to the difference of the nature of the interaction between the smaller clusters and the CNTs: smaller clusters are chemisorbed to the CNTs whilst larger clusters (starting with Ag_{55}) are physisorbed. Larger clusters interact more weakly with the CNT from the get-go. We have verified that this is not a geometry effect, since we only used icosahedral clusters. Making a sensor with CNTs and AgNCs would therefore benefit from the clusters being kept as small as possible, which would require having the cluster strongly fixed to the CNT. This last point is crucial, because the adsorption of CO weakens the interaction between the cluster and the CNT. How could one attempt to circumvent this issue? Using smaller diameter CNTs would be a first step, since it has been shown that metallic clusters diffuse less easily along smaller diameter CNTs [28]. Using the sensor in low temperature settings could also offset the agglomeration of smaller clusters into larger ones, due to there being lower thermal energy. Creating defects in the CNTs before depositing metallic clusters could also help keep clusters from diffusing along the CNTs since stronger bonds will form between the cluster and the CNT defect [98]. Finally, functionalizing either or both the CNT and the cluster could help keep clusters smaller and more dispersed along the CNTs. It is however important to keep in mind that the actual charge transport properties of such systems should be looked into, since charge transfer alone does not paint a complete picture of a functional device.

CHAPTER 5 CONCLUSION

In this work, we have studied the influence of quantum size effects of small and intermediately sized Ag clusters on the electronic properties of different AgNC-CNT interfaces. More specifically, we considered the interaction of small AgNCs with the metallic (5,5) and the semiconducting (10,0) carbon nanotubes with the help of density functional theory calculations. Restricting our study to icosahedral clusters, we were able to isolate size effects from geometry effects. Instead of arbitrarily setting a certain icosahedral geometry, we took care to relax the cluster systems, and defined a precise method to do so.

For isolated AgNCs, we observed that their electronic properties converged rapidly with the cluster size. For example, the main features of the bulk Ag density of states are nicely reproduced for Ag particles with 55 atoms and more. The electron charge within a cluster is mostly localized on surface atoms and depends on the symmetry and coordination of those surface atoms. The excess of electrons on the surface layer originates from its adjacent layer, while the core atoms have little fluctuation. The electron accumulation on the surface of the cluster makes them highly reactive, suggesting that AgNCs would interact with CNTs as electron donors.

For the AgNC/CNT systems, we have focused on the variation of electronic structure properties (charge transfer, dipole moment, DOS) with the cluster size while considering a well-defined atomic arrangement of the AgNC-CNT interface. The supercell size was carefully chosen to avoid the interaction of the AgNC with its periodic images. To the authors knowledge, such a rigorous convergence study has not been presented in the literature. This has allowed us to evaluate the extent of the charge injection and to maximize the amount of charge transferred between the AgNC and the CNT components.

With the adsorption of AgNCs on CNTs, significant charge transfer occurs and a major electron redistribution happens in the vicinity of the interface. An induced dipole moment appears at the interface, and in most cases electron charge flows from the cluster to the tube. The charge transfer and redistribution of AgNC electrons predominantly occur at their surface, and, as observed for isolated particles, the inner layers are not noticeably perturbed by the interaction with the CNT. Calculated adsorption energies indicate that Ag_4 and Ag_{13} clusters are chemisorbed to the CNTs, while the larger clusters are better described as physisorbed on CNTs. This difference in behaviour clearly shows a transition due to AgNC size which cannot be directly identified when studying isolated clusters. The transition from small clusters to intermediate clusters happens between 13 and 55 Ag atoms per cluster.

By analyzing the charge transfer and the DOS/PDOS of the systems, we have found that the charge neutrality level of a (10,0)-CNT is close to its conduction band minimum. In an attempt to use the phenomenological band lineup model to these last systems, we have found that a contour region along where the band lineup model can be applied. The contours are complex and follow the shape of the distribution of electron density among the molecular systems.

While studying the convergence of the AgNC/CNT unit cell size, we found that the injected electron charges can propagate over 25 Å away from the AgNC. In contrast, the exponential decay rates obtained from the calulated variation of charge density are significantly lower. This discrepancy confirms the existence of two length scales of charge redistribution; a first, slow, logarithmic, decay leads to a propagation length that is larger than the second decay length attributed to exponential charge variation, as pointed out by Léonard and Tersoff [7]. We have observed the presence of MIGS in the bandgap of the (10,0)-CNT for all the icosahedral clusters. The energy-dependant characteristics of the new states formed in the bandgap depend on the AgNC size, and result from the formation of molecular states with an increasing cluster size and also to the nature of the interaction.

Finally, the adsorption of CO on the Ag clusters introduces a profound modification of the interfacial properties of the AgNC/CNT systems, where the cluster adsorption energy decreases as well as the magnitude of the charge transfer. The variation in charge transfer with CO depends on the adsorption site, but is stronger for the smaller cluster studied here. The most striking change remains the systematic decrease in adsorption energy of the particles on the CNT walls. Hence, an adsorption of CO by the particles would weaken their adhesion on the CNT and should thus enhance the diffusion of metallic particles, facilitating the coalescence of small clusters into larger ones. Looking at clusters on either side of the size effect barrier (between 13 and 55 atoms) we had previously defined, we were furthermore able to define which size is prefereable for the fabrication of a CO sensor. It is undeniably beneficial to disperse small clusters along the CNT since charge variation upon CO adsorption is strongest for smaller clusters. Several routes could lead to this desired effect: one could either use smaller diameter CNTs, use the sensor in low temperature environments, or use defects to increase the cluster's bond to the CNT. Of course, one should keep in mind that using CO as an adsorbant skews the study for this specific type of sensor.

Limitations and future works

Although DFT remains one of the most powerful techniques to study the interaction of metal particles with carbon-based materials, there are still some pitfalls. First, the use of the PBE

functional necessarily leads to an underestimation of the band gap for the (10,0)-CNT. This could be an important, albeit not critical, aspect of the behaviour of the semiconducting CNTs that interact with AgNCs since the description depends on the relative energy positions of states from both constituents. The use of a hybrid functional would have been helpful to better model the properties related to the bandgap [119]. Also, the Ag_{55} and Ag_{147} are essentially physisorbed to CNTs, so the inclusion of van der Waals contributions to the energy could improve the accuracy of the results.

We need to emphasize that the present study has exclusively considered icosahedral clusters. This choice can easily be justified because we wanted to isolate size effects from geometry effects. The reality is that there are many different possible structural configurations for the clusters, and geometry effects should also be taken into account when designing devices using metal nanoclusters. The relative size of the AgNCs and CNTs should influence the interaction through interface size effects [28].

Finally, regarding the CO adsorption and subsequent modification of the interface, a more realistic situation should consider additional CO molecules. This is especially true for the case of larger clusters, since much more adsorption sites become available to CO. Non-equilibrium Green functions -based transport calculations would be beneficial to further clarify the effect of CO adsorption on the charge transport properties of the systems, and would help assess the differences in sensitivity between different sensor systems.

REFERENCES

[1] F. Baletto, R. Ferrando, A. Fortunelli, F. Montalenti, and C. Mottet. Crossover among structural motifs in transition and noble-metal clusters. *Journal of Chemical Physics*, 116(9):3856–3863, mar 2002. ISSN 00219606. doi: 10.1063/1.1448484. URL http://aip.scitation.org/doi/10.1063/1.1448484.

[2] J.A. Blackman. Structure of Isolated Clusters. In *Handbook of Metal Physics*, volume 5, pages 143–173. Elsevier, jan 2008. ISBN 9780444512406. doi: 10.1016/S1570-002X(08)00206-1. URL https://www.sciencedirect.com/science/article/pii/S1570002X08002061.

[3] J. W. Mintmire and C. T. White. Universal Density of States for Carbon Nanotubes. *Physical Review Letters*, 81(12):2506–2509, sep 1998. ISSN 0031-9007. doi: 10.1103/PhysRevLett.81.2506. URL https://link.aps.org/doi/10.1103/PhysRevLett.81.2506.

[4] Jean-Christophe Charlier, Xavier Blase, and Stephan Roche. Electronic and transport properties of nanotubes. *Reviews of Modern Physics*, 79(2):677–732, may 2007. ISSN 0034-6861, 1539-0756. doi: 10.1103/RevModPhys.79.677. URL http://link.aps.org/doi/10.1103/RevModPhys.79.677.

[5] Yuki Matsuda, Jamil Tahir-Kheli, and William A Goddard. Definitive Band Gaps for Single-Wall Carbon Nanotubes. *J. Phys. Chem. Lett*, 1:2946–2950, 2010. doi: 10.1021/jz100889u. URL http://www.wag.caltech.edu/publications/sup/pdf/882.pdf.

[6] Francois Leonard and J. Tersoff. Role of Fermi-level pinning in nanotube Schottky diodes. *Physical Review Letters*, 84(20):4693–4696, 2000. ISSN 0031-9007. doi: 10.1103/PhysRevLett.84.4693. URL http://arxiv.org/abs/cond-mat/0003454.

[7] François Léonard and J. Tersoff. Novel length scales in nanotube devices. *Physical Review Letters*, 83(24):5174–5177, dec 1999. ISSN 10797114. doi: 10.1103/PhysRevLett.83.5174. URL https://link.aps.org/doi/10.1103/PhysRevLett.83.5174.

[8] Phaedon Avouris, Zhihong Chen, and Vasili Perebeinos. Carbon-based electronics. *Nature Nanotechnology*, 2(10):605–615, oct 2007. ISSN 1748-3387. doi: 10.1038/nnano.2007.300. URL http://www.nature.com/articles/nnano.2007.300.

[9] Caterina Soldano. Hybrid metal-based carbon nanotubes: Novel platform for multifunctional applications, 2015. ISSN 00796425.

[10] R. Martel, T. Schmidt, H. R. Shea, T. Hertel, and Ph. Avouris. Single- and multi-wall carbon nanotube field-effect transistors. *Applied Physics Letters*, 73(17):2447–2449, oct 1998. ISSN 0003-6951. doi: 10.1063/1.122477. URL http://aip.scitation.org/doi/10.1063/1.122477.

[11] V Gayathri and R Geetha. Carbon nanotube as NEMS sensor - effect of chirality and stone-wales defect intend. *Journal of Physics: Conference Series*, 34(1):824–828, apr 2006. ISSN 1742-6588. doi: 10.1088/1742-6596/34/1/136. URL http://stacks.iop.org/1742-6596/34/i=1/a=136?key=crossref.bb86a0ac3d22cf71ad5a461e929969f9.

[12] Antti Kaskela, Patrik Laiho, Norihiro Fukaya, Kimmo Mustonen, Toma Susi, Hua Jiang, Nikolay Houbenov, Yutaka Ohno, and Esko I. Kauppinen. Highly individual SWCNTs for high performance thin film electronics. *Carbon*, 103:228–234, jul 2016. ISSN 00086223. doi: 10.1016/j.carbon.2016.02.099. URL http://www.sciencedirect.com/science/article/pii/S0008622316301889http://www.sciencedirect.com/science/article/pii/S0008622316301889/pdfft?md5=03aaf4ebf7f90dacb9fa22920dfaa1d5{&}pid=1-s2.0-S0008622316301889-main.pdf.

[13] Ashish Modi, Nikhil Koratkar, Eric Lass, Bingqing Wei, and Pulickel M. Ajayan. Miniaturized gas ionization sensors using carbon nanotubes. *Nature*, 424(6945):171–174, jul 2003. ISSN 0028-0836. doi: 10.1038/nature01777. URL http://www.nature.com/articles/nature01777.

[14] J. Kong, M. G. Chapline, and H. Dai. Functionalized Carbon Nanotubes for Molecular Hydrogen Sensors. *Advanced Materials*, 13(18):1384–1386, sep 2001. ISSN 0935-9648. doi: 10.1002/1521-4095(200109)13:18<1384::AID-ADMA1384>3.0.CO;2-8. URL http://doi.wiley.com/10.1002/1521-4095{%}28200109{%}2913{%}3A18{%}3C1384{%}3A{%}3AAID-ADMA1384{%}3E3.0.CO{%}3B2-8.

[15] Ahmed Abdelhalim, Alaa Abdellah, Giuseppe Scarpa, and Paolo Lugli. Metallic nanoparticles functionalizing carbon nanotube networks for gas sensing applications. *Nanotechnology*, 25(5):055208, feb 2014. ISSN 0957-4484. doi: 10.1088/0957-4484/25/5/055208. URL http://www.ncbi.nlm.nih.gov/pubmed/

24407105http://stacks.iop.org/0957-4484/25/i=5/a=055208?key=crossref.76ae615baee4f088efe69a441895f042.

[16] Zeila Zanolli, Radouane Leghrib, Alexandre Felten, Jean Jacques Pireaux, Eduard Llobet, and Jean Christophe Charlier. Gas sensing with Au-decorated carbon nanotubes. *ACS Nano*, 2011. ISSN 19360851. doi: 10.1021/nn200294h.

[17] L. Balents and R. Egger. Spin Transport in Interacting Quantum Wires and Carbon Nanotubes. *Physical Review Letters*, 85(16):3464–3467, oct 2000. ISSN 0031-9007. doi: 10.1103/PhysRevLett.85.3464. URL https://link.aps.org/doi/10.1103/PhysRevLett.85.3464.

[18] S. A. Chesnokov, V. A. Nalimova, A. G. Rinzler, R. E. Smalley, and J. E. Fischer. Mechanical Energy Storage in Carbon Nanotube Springs. *Physical Review Letters*, 82(2):343–346, jan 1999. ISSN 0031-9007. doi: 10.1103/PhysRevLett.82.343. URL https://link.aps.org/doi/10.1103/PhysRevLett.82.343.

[19] F Kreupl, A.P Graham, G.S Duesberg, W Steinhögl, M Liebau, E Unger, and W Hönlein. Carbon nanotubes in interconnect applications. *Microelectronic Engineering*, 64(1-4): 399–408, oct 2002. ISSN 0167-9317. doi: 10.1016/S0167-9317(02)00814-6. URL https://www.sciencedirect.com/science/article/pii/S0167931702008146.

[20] Caterina Soldano, Saikat Talapatra, and Swastik Kar. *Carbon Nanotubes and Graphene Nanoribbons: Potentials for Nanoscale Electrical Interconnects*, volume 2. 2013. ISBN 3905163985. doi: 10.3390/electronics2030280. URL http://www.mdpi.com/2079-9292/2/3/280/.

[21] A. Naeemi, R. Sarvari, and J.D. Meindl. Performance comparison between carbon nanotube and copper interconnects for gigascale integration (GSI). *IEEE Electron Device Letters*, 26(2):84–86, feb 2005. ISSN 0741-3106. doi: 10.1109/LED.2004.841440. URL http://ieeexplore.ieee.org/document/1386402/.

[22] Calum F McAndrew and Mark Baxendale. High electrical conductance enhancement in Au-nanoparticle decorated sparse single-wall carbon nanotube networks. *Nanotechnology*, 24(30):305202, aug 2013. ISSN 0957-4484. doi: 10.1088/0957-4484/24/30/305202. URL http://stacks.iop.org/0957-4484/24/i=30/a=305202?key=crossref.6b0faaaa12316580a916ee56e383bfa8.

[23] Mark A. Topinka, Michael W. Rowell, David Goldhaber-Gordon, Michael D. McGehee, David S. Hecht, and George Gruner. Charge transport in interpenetrating networks

of semiconducting and metallic carbon nanotubes. *Nano Letters*, 9(5):1866–1871, may 2009. ISSN 15306984. doi: 10.1021/nl803849e. URL http://pubs.acs.org/doi/abs/10.1021/nl803849ehttp://pubs.acs.org/doi/pdf/10.1021/nl803849e.

[24] Xiaojuan Tian, Matthew L Moser, Aron Pekker, Santanu Sarkar, Jason Ramirez, Elena Bekyarova, Mikhail E Itkis, and Robert C Haddon. Effect of atomic interconnects on percolation in single-walled carbon nanotube thin film networks. *Nano Letters*, 14(7): 3930–3937, 2014. ISSN 15306992. doi: 10.1021/nl501212u. URL http://pubs.acs.org/doi/pdfplus/10.1021/nl501212u.

[25] T Ketolainen, V Havu, and M J Puska. Enhancing conductivity of metallic carbon nanotube networks by transition metal adsorption. *The Journal of Chemical Physics*, 142(142), 2015. doi: 10.1063/1.4907205. URL http://dx.doi.org/10.1063/1.4907205http://aip.scitation.org/toc/jcp/142/5.

[26] K H Khoo and James R Chelikowsky. Electron transport across carbon nanotube junctions decorated with Au nanoparticles: Density functional calculations. *Physical Review B*, 79:205422, 2009. doi: 10.1103/PhysRevB.79.205422. URL https://journals.aps.org/prb/pdf/10.1103/PhysRevB.79.205422.

[27] Manuela Scarselli, Luca Camilli, Paola Castrucci, Francesca Nanni, Silvano Del Gobbo, Eric Gautron, Serge Lefrant, and Maurizio De Crescenzi. In situ formation of noble metal nanoparticles on multiwalled carbon nanotubes and its implication in metalâ“nanotube interactions. *Carbon*, 50:875–884, 2012. doi: 10.1016/j.carbon.2011.09.048. URL http://ac.els-cdn.com/S0008622311008037/1-s2.0-S0008622311008037-main.pdf?{_}tid=b523d41c-3e73-11e7-841d-00000aab0f01{&}acdnat=1495405414{_}ba7b9e49814ce7b6b328e767c6b3247f.

[28] Aleksandar Staykov, Yuuki Ooishi, and Tatsumi Ishihara. Immobilizing metal nanoparticles on single wall nanotubes. Effect of surface curvature. *Journal of Physical Chemistry C*, 2014. ISSN 19327455. doi: 10.1021/jp410775n.

[29] M. Penza, R. Rossi, M. Alvisi, G. Cassano, and E. Serra. Functional characterization of carbon nanotube networked films functionalized with tuned loading of Au nanoclusters for gas sensing applications. *Sensors and Actuators, B: Chemical*, 140(1):176–184, 2009. ISSN 09254005. doi: 10.1016/j.snb.2009.04.008.

[30] Syed Mubeen, Jae Hong Lim, Aarti Srirangarajan, Ashok Mulchandani, Marc A. Deshusses, and Nosang V. Myung. Gas sensing mechanism of gold nanoparticles decorated single-walled carbon nanotubes. *Electroanalysis*, 23(11):2687–2692, nov 2011.

ISSN 10400397. doi: 10.1002/elan.201100299. URL http://doi.wiley.com/10.1002/elan.201100299.

[31] Sumio Iijima. Helical microtubules of graphitic carbon. *Nature*, 354(6348):56–58, nov 1991. ISSN 0028-0836. doi: 10.1038/354056a0. URL http://www.nature.com/doifinder/10.1038/354056a0.

[32] François Léonard. The Physics of Carbon Nanotube Devices, 2009. ISSN 1098-6596. URL http://cds.cern.ch/record/1539205http://www.sciencedirect.com/science/article/pii/B9780815515739500100.

[33] C. Thomsen, S. Reich, and J. Maultzsch. *Electronic Properties of Carbon Nanotubes*. Wiley-VCH Verlag GmbH, Weinheim, Germany, 2007. ISBN 9783527618040. doi: 10.1002/9783527618040.ch3. URL http://doi.wiley.com/10.1002/9783527618040.ch3http://dx.doi.org/10.1002/9783527618040.ch3.

[34] J.-C. Charlier and Ph. Lambin. Electronic structure of carbon nanotubes with chiral symmetry. *Physical Review B*, 57(24):R15037–R15039, jun 1998. ISSN 0163-1829. doi: 10.1103/PhysRevB.57.R15037. URL https://link.aps.org/doi/10.1103/PhysRevB.57.R15037.

[35] J.W. Mintmire and C.T. White. Electronic and structural properties of carbon nanotubes. *Carbon*, 33(7):893–902, jan 1995. ISSN 0008-6223. doi: 10.1016/0008-6223(95)00018-9. URL https://www.sciencedirect.com/science/article/pii/0008622395000189.

[36] Jeroen W. G. Wilder, Liesbeth C. Venema, Andrew G. Rinzler, Richard E. Smalley, and Cees Dekker. Electronic structure of atomically resolved carbon nanotubes. *Nature*, 391(6662):59–62, jan 1998. ISSN 00280836. doi: 10.1038/34139. URL http://www.nature.com/doifinder/10.1038/34139.

[37] Teri Wang Odom, Jin-Lin Huang, Philip Kim, and Charles M. Lieber. Atomic structure and electronic properties of single-walled carbon nanotubes. *Nature*, 391(6662):62–64, jan 1998. ISSN 0028-0836. doi: 10.1038/34145. URL http://www.nature.com/articles/34145.

[38] R. Saito and G. Dresselhaus. Trigonal warping effect of carbon nanotubes. *Physical Review B - Condensed Matter and Materials Physics*, 61(4):2981–2990, jan 2000. ISSN 1550235X. doi: 10.1103/PhysRevB.61.2981. URL https://link.aps.org/doi/10.1103/PhysRevB.61.2981.

[39] M Machón, S Reich, C Thomsen, D Sánchez-Portal, and P Ordejón. Ab initio calculations of the optical properties of 4-Å-diameter single-walled nanotubes. *Physical Review B*, 66, 2002. doi: 10.1103/PhysRevB.66.155410. URL https://journals.aps.org/prb/pdf/10.1103/PhysRevB.66.155410.

[40] M. Damnjanović, I. Milošević, T. Vuković, and J Maultzsch. Quantum numbers and band topology of nanotubes. *Journal of Physics A: Mathematical and General*, 36(21):5707–5717, may 2003. ISSN 03054470. doi: 10.1088/0305-4470/36/21/302. URL http://stacks.iop.org/0305-4470/36/i=21/a=302?key=crossref.fabad2d8adc2b5f4820783a55be87a4a.

[41] M. Damnjanovic, T. Vukovic, I. Milosevic, and I Milos. Fermi level quantum numbers and secondary gap of conducting carbon nanotubes. *Solid State Communications*, 116 (5):265–267, sep 2000. ISSN 0038-1098. doi: 10.1016/S0038-1098(00)00319-7. URL https://www.sciencedirect.com/science/article/pii/S0038109800003197.

[42] G Y Sun, J Kurti, M Kertesz, and R H Baughman. Variations of the geometries and band gaps of single-walled carbon nanotubes and the effect of charge injection. *Journal Of Physical Chemistry B*, 107(29):6924–6931, 2003. ISSN 1520-6106. doi: 10.1021/jp022629p. URL https://pubs.acs.org/doi/abs/10.1021/jp022629ppapers2://publication/doi/10.1021/jp022629p.

[43] X Blase, Lorin X Benedict, Eric L Shirley, and Steven G Louie. Hybridization effects and metallicity in small radius carbon nanotubes. *Physical Review Letters*, 72(12): 1878–1881, 1994. ISSN 00319007. doi: 10.1103/PhysRevLett.72.1878. URL https://journals.aps.org/prl/pdf/10.1103/PhysRevLett.72.1878.

[44] Kazume Nishidate and Masayuki Hasegawa. Deformation and transfer doping of a single-walled carbon nanotube adsorbed on metallic substrates. *Physical Review B*, 81(12):125414, mar 2010. ISSN 1098-0121. doi: 10.1103/PhysRevB.81.125414. URL https://link.aps.org/doi/10.1103/PhysRevB.81.125414.

[45] Alberto Roldán, Francesc Viñes, Francesc Illas, Josep Manel Ricart, and Konstantin M. Neyman. Density functional studies of coinage metal nanoparticles: scalability of their properties to bulk. *Theoretical Chemistry Accounts*, 120(4-6):565–573, jul 2008. ISSN 1432-881X. doi: 10.1007/s00214-008-0423-x. URL http://link.springer.com/10.1007/s00214-008-0423-x.

[46] Alberto Roldán, Silvia González, Josep Manel Ricart, and Francesc Illas. Critical size for O_2 dissociation by Au nanoparticles. *ChemPhysChem*, 10(2):348–351, feb 2009.

ISSN 14394235. doi: 10.1002/cphc.200800702. URL http://doi.wiley.com/10.1002/cphc.200800702.

[47] Jose A. Lopez-Sanchez, Nikolaos Dimitratos, Ceri Hammond, Gemma L. Brett, Lokesh Kesavan, Saul White, Peter Miedziak, Ramchandra Tiruvalam, Robert L. Jenkins, Albert F. Carley, David Knight, Christopher J. Kiely, and Graham J. Hutchings. Facile removal of stabilizer-ligands from supported gold nanoparticles. *Nature Chemistry*, 3 (7):551–556, jul 2011. ISSN 1755-4330. doi: 10.1038/nchem.1066. URL http://www.nature.com/articles/nchem.1066.

[48] N.D. Lang and W. Kohn. Theory of Metal Surfaces: Charge Density and Surface Energy. *Physical Review B*, 1(12), 1970. URL http://jpkc.fudan.edu.cn/picture/article/90/64657339-a919-423f-b5ff-425cd2983d2d/bfdbbced-32ca-427b-ac38-45f14788547d.pdf.

[49] N.D. Lang and W. Kohn. Theory of Metal Surfaces: Work Function. *Physical Review B*, 3(4), 1971. URL https://journals.aps.org/prb/pdf/10.1103/PhysRevB.3.1215.

[50] Robert G. Parr, Robert A. Donnelly, Mel Levy, and William E. Palke. Electronegativity: The density functional viewpoint. *The Journal of Chemical Physics*, 68(8):3801–3807, apr 1978. ISSN 0021-9606. doi: 10.1063/1.436185. URL http://aip.scitation.org/doi/10.1063/1.436185.

[51] J.A. Blackman. Shell Models of Isolated Clusters. In *Handbook of Metal Physics*, volume 5, pages 17–47. Elsevier, jan 2008. ISBN 9780444512406. doi: 10.1016/S1570-002X(08)00202-4. URL https://www.sciencedirect.com/science/article/pii/S1570002X08002024.

[52] Nobuhisa Fujima and Tsuyoshi Yamaguchi. Shell Structure of Electronic State of Icosahedral Al and Cu Clusters. *Journal of the Physical Society of Japan*, 58(4):1334–1346, apr 1989. ISSN 0031-9015. doi: 10.1143/JPSJ.58.1334. URL http://journals.jps.jp/doi/10.1143/JPSJ.58.1334.

[53] F D Kiss, R Miotto, and A C Ferraz. Size effects on silver nanoparticles' properties. *Nanotechnology*, 22(27):275708, jul 2011. ISSN 0957-4484. doi: 10.1088/0957-4484/22/27/275708. URL http://stacks.iop.org/0957-4484/22/i=27/a=275708?key=crossref.1dce844f97469c0b7e1cf2995c5c1ec8.

[54] K. Michaelian, N. Rendón, and I. L. Garzón. Structure and energetics of ni, ag, and au nanoclusters. *Physical Review B - Condensed Matter and Materials Physics*, 60

(3):2000–2010, jul 1999. ISSN 1550235X. doi: 10.1103/PhysRevB.60.2000. URL https://link.aps.org/doi/10.1103/PhysRevB.60.2000.

[55] J. Oviedo and R. E. Palmer. Amorphous structures of Cu, Ag, and Au nanoclusters from first principles calculations. *The Journal of Chemical Physics*, 117(21):9548–9551, dec 2002. ISSN 0021-9606. doi: 10.1063/1.1524154. URL http://aip.scitation.org/doi/10.1063/1.1524154.

[56] Hannu Häkkinen, Michael Moseler, Oleg Kostko, Nina Morgner, Margarita Astruc Hoffmann, and Bernd V. Issendorff. Symmetry and electronic structure of noble-metal nanoparticles and the role of relativity. *Physical Review Letters*, 93(9):093401, aug 2004. ISSN 00319007. doi: 10.1103/PhysRevLett.93.093401. URL http://www.ncbi.nlm.nih.gov/pubmed/15447098https://link.aps.org/doi/10.1103/PhysRevLett.93.093401.

[57] Filipp Furche, Reinhart Ahlrichs, Patrick Weis, Christoph Jacob, Stefan Gilb, Thomas Bierweiler, and Manfred M. Kappes. The structures of small gold cluster anions as determined by a combination of ion mobility measurements and density functional calculations. *Journal of Chemical Physics*, 117(15):6982–6990, oct 2002. ISSN 00219606. doi: 10.1063/1.1507582. URL http://aip.scitation.org/doi/10.1063/1.1507582.

[58] Yuannan Xie and John A Blackman. Transferable tight-binding model for palladium and silver. *Physical Review B - Condensed Matter and Materials Physics*, 64(19), 2001. ISSN 1550235X. doi: 10.1103/PhysRevB.64.195115. URL https://journals.aps.org/prb/pdf/10.1103/PhysRevB.64.195115.

[59] Hannu Häkkinen and Michael Moseler. 55-Atom clusters of silver and gold: Symmetry breaking by relativistic effects. In *Computational Materials Science*, volume 35, pages 332–336. Elsevier, mar 2006. doi: 10.1016/j.commatsci.2004.08.017. URL https://www.sciencedirect.com/science/article/pii/S0927025605001552.

[60] Mukul Kabir, Abhijit Mookerjee, and A. K. Bhattacharya. Structure and stability of copper clusters: A tight-binding molecular dynamics study. *Physical Review A - Atomic, Molecular, and Optical Physics*, 69(4):043203, apr 2004. ISSN 10502947. doi: 10.1103/PhysRevA.69.043203. URL https://link.aps.org/doi/10.1103/PhysRevA.69.043203.

[61] Eva M. Fernández, José M. Soler, Ignacio L. Garzón, and Luis C. Balbás. Trends in the structure and bonding of noble metal clusters. *Physical Review B*, 70(16):

7–8, oct 2004. ISSN 1098-0121. doi: 10.1103/PhysRevB.70.165403. URL https://link.aps.org/doi/10.1103/PhysRevB.70.165403.

[62] H.-Ch. Weissker and C. Mottet. Optical properties of pure and core-shell noble-metal nanoclusters from TDDFT: The influence of the atomic structure. *Physical Review B*, 84(16):165443, oct 2011. ISSN 1098-0121. doi: 10.1103/PhysRevB.84.165443. URL https://link.aps.org/doi/10.1103/PhysRevB.84.165443.

[63] John T. Titantah and Mikko Karttunen. Ab initio calculations of optical properties of silver clusters: cross-over from molecular to nanoscale behavior. *European Physical Journal B*, 89(5), 2016. ISSN 14346036. doi: 10.1140/epjb/e2016-70065-y. URL https://pure.tue.nl/ws/files/32873922/rana16{_}07.pdf.

[64] Yi He and Taofang Zeng. First-Principles Study and Model of Dielectric Functions of Silver Nanoparticles. *The Journal of Physical Chemistry C*, 114(42):18023–18030, 2010. ISSN 1932-7447. doi: 10.1021/jp101598j. URL https://pubs.acs.org/doi/abs/10.1021/jp101598j{%}40proofinghttp://pubs.acs.org/doi/abs/10.1021/jp101598j.

[65] André Fielicke, Philipp Gruene, Gerard Meijer, and David M. Rayner. The adsorption of CO on transition metal clusters: A case study of cluster surface chemistry. *Surface Science*, 603(10-12):1427–1433, jun 2009. ISSN 0039-6028. doi: 10.1016/J.SUSC.2008.09.064. URL https://www.sciencedirect.com/science/article/pii/S0039602809000636.

[66] Alexandre A. Shvartsburg, Robert R. Hudgins, Philippe Dugourd, and Martin F. Jarrold. Structural information from ion mobility measurements: applications to semiconductor clusters. *Chemical Society Reviews*, 30(1):26–35, jan 2001. ISSN 03060012. doi: 10.1039/a802099j. URL http://xlink.rsc.org/?DOI=a802099j.

[67] Patrick Weis. Structure determination of gaseous metal and semi-metal cluster ions by ion mobility spectrometry, aug 2005. ISSN 13873806. URL https://www.sciencedirect.com/science/article/pii/S1387380605001612.

[68] Detlef Schooss, Martine N. Blom, Joel H. Parks, Bernd V. Issendorff, Hellmut Haberland, and Manfred M. Kappes. The structures of Ag 55+ and Ag 55-: Trapped ion electron diffraction and density functional theory. *Nano Letters*, 5(10):1972–1977, 2005. ISSN 15306984. doi: 10.1021/nl0513434. URL https://pubs.acs.org/doi/abs/10.1021/nl0513434.

[69] Xiaopeng Xing, Bokwon Yoon, Uzi Landman, and Joel H. Parks. Structural evolution of Au nanoclusters: From planar to cage to tubular motifs. *Physical Review B - Condensed Matter and Materials Physics*, 74(16):165423, oct 2006. ISSN 10980121. doi: 10.1103/PhysRevB.74.165423. URL https://link.aps.org/doi/10.1103/PhysRevB.74.165423.

[70] Jun Li, Xi Li, Hua Jin Zhai, and Lai Sheng Wang. Au20: A tetrahedral cluster. *Science*, 299(5608):864–867, feb 2003. ISSN 00368075. doi: 10.1126/science.1079879. URL http://www.ncbi.nlm.nih.gov/pubmed/12574622.

[71] Da Hye Kim, Kihyun Shin, and Hyuck Mo Lee. CO Oxidation on Positively and Negatively Charged Ag ₁₃ Nanoparticles. *The Journal of Physical Chemistry C*, 115(50):24771–24777, dec 2011. ISSN 1932-7447. doi: 10.1021/jp207338w. URL http://pubs.acs.org/doi/10.1021/jp207338w.

[72] Hans Lüth. Electronic Surface States. pages 253–335. 2015. doi: 10.1007/978-3-319-10756-1_6. URL http://link.springer.com/10.1007/978-3-319-10756-1{_}6.

[73] Raymond T. Tung. The physics and chemistry of the Schottky barrier height. *Applied Physics Reviews*, 1(1):011304, mar 2014. ISSN 1931-9401. doi: 10.1063/1.4858400.

[74] Winfried Mönch. Explanation of the barrier heights of graphene Schottky contacts by the MIGS-and-electronegativity concept. *Journal of Applied Physics*, 120(10):104501, sep 2016. ISSN 10897550. doi: 10.1063/1.4962310. URL http://aip.scitation.org/doi/10.1063/1.4962310.

[75] John Bardeen. Surface states and rectification at a metal semi-conductor contact. *Physical Review*, 71(10):717–727, may 1947. ISSN 0031899X. doi: 10.1103/PhysRev.71.717. URL https://link.aps.org/doi/10.1103/PhysRev.71.717.

[76] S. Kurtin, T. C. McGill, and C. A. Mead. Fundamental transition in the electronic nature of solids. *Physical Review Letters*, 22(26):1433–1436, jun 1969. ISSN 00319007. doi: 10.1103/PhysRevLett.22.1433. URL https://link.aps.org/doi/10.1103/PhysRevLett.22.1433.

[77] L. J. Brillson, S. Chang, J. Shaw, and R. E. Viturro. Interface states at metal-compound semiconductor junctions. *Vacuum*, 41(4-6):1016–1020, may 1990. ISSN 0042207X. doi: 10.1016/0042-207X(90)93849-E. URL http://stacks.iop.org/0034-4885/62/i=5/a=203?key=crossref.5aa2366096721044a0586cd7facad9e4.

[78] Volker Heine. Theory of surface states. *Physical Review*, 138(6A):A1689–A1696, jun 1965. ISSN 0031899X. doi: 10.1103/PhysRev.138.A1689. URL https://link.aps.org/doi/10.1103/PhysRev.138.A1689.

[79] A. M. Cowley and S. M. Sze. Surface States and Barrier Height of Metal-Semiconductor Systems. pages 74–82. Springer, Dordrecht, 1999. doi: 10.1007/978-94-009-0657-0_8. URL http://www.springerlink.com/index/10.1007/978-94-009-0657-0{_}8.

[80] Raymond T. Tung. Chemical Bonding and Fermi Level Pinning at Metal-Semiconductor Interfaces. *Physical Review Letters*, 84(26), 2000. URL https://journals.aps.org/prl/pdf/10.1103/PhysRevLett.84.6078.

[81] T. Thonhauser, Valentino R. Cooper, Shen Li, Aaron Puzder, Per Hyldgaard, and David C. Langreth. Van der Waals density functional: Self-consistent potential and the nature of the van der Waals bond. *Physical Review B - Condensed Matter and Materials Physics*, 76(12):125112, sep 2007. ISSN 10980121. doi: 10.1103/PhysRevB.76.125112. URL https://link.aps.org/doi/10.1103/PhysRevB.76.125112.

[82] P. A. Khomyakov, G. Giovannetti, P. C. Rusu, G. Brocks, J. Van Den Brink, and P. J. Kelly. First-principles study of the interaction and charge transfer between graphene and metals. *Physical Review B - Condensed Matter and Materials Physics*, 79(19):195425, may 2009. ISSN 10980121. doi: 10.1103/PhysRevB.79.195425. URL https://link.aps.org/doi/10.1103/PhysRevB.79.195425.

[83] Xavier Crispin, Victor Geskin, Annica Crispin, Jérôme Cornil, Roberto Lazzaroni, William R. Salaneck, and Jean-Luc Brédas. Characterization of the Interface Dipole at Organic/ Metal Interfaces. *Journal of the American Chemical Society*, 124(27):8131–8141, 2002. ISSN 0002-7863. doi: 10.1021/ja025673r. URL http://dx.doi.org/10.1021/ja025673r{%}5Cnhttp://pubs.acs.org/doi/full/10.1021/ja025673r{%}5Cnhttp://pubs.acs.org/doi/pdfplus/10.1021/ja025673r.

[84] Paul S. Bagus, Volker Staemmler, and Christof Wöll. Exchangelike Effects for Closed-Shell Adsorbates: Interface Dipole and Work Function. *Physical Review Letters*, 89 (9):096104, aug 2002. ISSN 10797114. doi: 10.1103/PhysRevLett.89.096104. URL https://link.aps.org/doi/10.1103/PhysRevLett.89.096104.

[85] Gregor Witte, Simon Lukas, Paul S. Bagus, and Christof Wöll. Vacuum level alignment at organic/metal junctions: "cushion" effect and the interface dipole. *Applied Physics Letters*, 87(26):1–3, dec 2005. ISSN 00036951. doi: 10.1063/1.2151253. URL http://aip.scitation.org/doi/10.1063/1.2151253.

[86] Paul C. Rusu, Gianluca Giovannetti, Christ Weijtens, Reinder Coehoorn, and Geert Brocks. First-principles study of the dipole layer formation at metal-organic interfaces. *Physical Review B - Condensed Matter and Materials Physics*, 81(12):125403, mar 2010. ISSN 10980121. doi: 10.1103/PhysRevB.81.125403. URL https://link.aps.org/doi/10.1103/PhysRevB.81.125403.

[87] Masayuki Hasegawa and Kazume Nishidate. Transfer doping of a metallic carbon nanotube and graphene on metal surfaces. *Physical Review B - Condensed Matter and Materials Physics*, 83(15):155435, apr 2011. ISSN 10980121. doi: 10.1103/PhysRevB.83.155435. URL https://link.aps.org/doi/10.1103/PhysRevB.83.155435.

[88] Bin Shan and Kyeongjae Cho. Ab initio study of Schottky barriers at metal-nanotube contacts. *Physical Review B - Condensed Matter and Materials Physics*, 70(23):1–4, dec 2004. ISSN 10980121. doi: 10.1103/PhysRevB.70.233405. URL https://link.aps.org/doi/10.1103/PhysRevB.70.233405.

[89] Yu He, Jinyu Zhang, Shimin Hou, Yan Wang, and Zhiping Yu. Schottky barrier formation at metal electrodes and semiconducting carbon nanotubes. *Applied Physics Letters*, 94(9):093107, mar 2009. ISSN 00036951. doi: 10.1063/1.3093677. URL http://aip.scitation.org/doi/10.1063/1.3093677.

[90] Johannes Svensson and Eleanor E. B. Campbell. Schottky barriers in carbon nanotube-metal contacts. *Journal of Applied Physics*, 110(11):111101, dec 2011. ISSN 0021-8979. doi: 10.1063/1.3664139. URL http://aip.scitation.org/doi/10.1063/1.3664139.

[91] Susumu Okada, Susumu Okada, Atsushi Oshiyama, and Atsushi Oshiyama. Electronic structure of semiconducting nanotubes adsorbed on metal surfaces. *Physical Review Letters*, 95(November):206804, nov 2005. ISSN 0031-9007. doi: 10.1103/PhysRevLett.95.206804. URL http://www.ncbi.nlm.nih.gov/pubmed/16384083https://link.aps.org/doi/10.1103/PhysRevLett.95.206804http://journals.aps.org/prl/abstract/10.1103/PhysRevLett.95.206804.

[92] Vincenzo Vitale, Alessandro Curioni, and Wanda Andreoni. MetalCarbon Nanotube Contacts: The Link between Schottky Barrier and Chemical Bonding. *Journal of the American Chemical Society*, 130(18):5848–5849, may 2008. ISSN 0002-7863. doi: 10.1021/ja8002843. URL http://pubs.acs.org/doi/abs/10.1021/ja8002843.

[93] Wenguang Zhu and Efthimios Kaxiras. The nature of contact between Pd leads and semiconducting carbon nanotubes. *Nano Letters*, 6(7):1415–1419, 2006. ISSN 15306984. doi: 10.1021/nl0604311. URL https://pubs.acs.org/doi/abs/10.1021/nl0604311.

[94] Gregory G. Wildgoose, Craig E. Banks, and Richard G. Compton. Metal Nanoparticles and Related Materials Supported on Carbon Nanotubes: Methods and Applications. *Small*, 2(2):182–193, feb 2006. ISSN 1613-6810. doi: 10.1002/smll.200500324. URL http://doi.wiley.com/10.1002/smll.200500324.

[95] Hiroaki Ozawa, Xun Yi, Tsuyohiko Fujigaya, Yasuro Niidome, Tanemasa Asano, and Naotoshi Nakashima. Supramolecular Hybrid of Gold Nanoparticles and Semiconducting Single-Walled Carbon Nanotubes Wrapped by a Porphyrin–Fluorene Copolymer. *Journal of the American Chemical Society*, 133(37):14771–14777, sep 2011. ISSN 0002-7863. doi: 10.1021/ja2055885. URL http://pubs.acs.org/doi/abs/10.1021/ja2055885.

[96] Tsuyohiko Fujigaya, Minoru Okamoto, and Naotoshi Nakashima. Design of an assembly of pyridine-containing polybenzimidazole, carbon nanotubes and Pt nanoparticles for a fuel cell electrocatalyst with a high electrochemically active surface area. *Carbon*, 47(14):3227–3232, nov 2009. ISSN 0008-6223. doi: 10.1016/J.CARBON.2009.07.038. URL https://www.sciencedirect.com/science/article/pii/S0008622309004606?via{%}3Dihub.

[97] Benedetta Cornelio, Graham A. Rance, Marie Laronze-Cochard, Antonella Fontana, Janos Sapi, and Andrei N. Khlobystov. Palladium nanoparticles on carbon nanotubes as catalysts of cross-coupling reactions. *Journal of Materials Chemistry A*, 1(31):8737, jul 2013. ISSN 2050-7488. doi: 10.1039/c3ta11530e. URL http://xlink.rsc.org/?DOI=c3ta11530e.

[98] Douglas R. Kauffman and Alexander Star. Chemically induced potential barriers at the carbon nanotube-metal nanoparticle interface. *Nano Letters*, 2007. ISSN 15306984. doi: 10.1021/nl070330i.

[99] Douglas R. Kauffman, Dan C. Sorescu, Daniel P. Schofield, Brett L. Allen, Kenneth D. Jordan, and Alexander Star. Understanding the sensor response of metal-decorated carbon nanotubes. *Nano Letters*, 2010. ISSN 15306984. doi: 10.1021/nl903888c.

[100] Mengning Ding, Yifan Tang, and Alexander Star. Understanding interfaces in metal-graphitic hybrid nanostructures, 2013. ISSN 19487185.

[101] Louis-Philippe Simoneau, Jérémie Villeneuve, Carla M. Aguirre, Richard Martel, Patrick Desjardins, and Alain Rochefort. Influence of statistical distributions on the electrical properties of disordered and aligned carbon nanotube networks. *Journal of Applied Physics*, 114(11):114312, sep 2013. ISSN 0021-8979. doi: 10.1063/1.4821885. URL http://aip.scitation.org/doi/10.1063/1.4821885.

[102] George Blyholder. Molecular Orbital View of Chemisorbed Carbon Monoxide. *The Journal of Physical Chemistry*, 68(10):2772–2777, oct 1964. ISSN 0022-3654. doi: 10.1021/j100792a006. URL http://pubs.acs.org/doi/abs/10.1021/j100792a006.

[103] Wenping Zeng, Jian Tang, Pu Wang, and Yong Pei. Density functional theory (DFT) studies of CO oxidation reaction on M ₁₃ and Au ₁₈ M clusters (M = Au, Ag, Cu, Pt and Pd): the role of co-adsorbed CO molecule. *RSC Advances*, 6(61):55867–55877, jun 2016. ISSN 2046-2069. doi: 10.1039/C6RA07566E. URL http://xlink.rsc.org/?DOI=C6RA07566E.

[104] C. M. Chang, C. Cheng, and C. M. Wei. CO oxidation on unsupported Au55, Ag55, and Au25Ag30 nanoclusters. *The Journal of Chemical Physics*, 128(12):124710, mar 2008. ISSN 0021-9606. doi: 10.1063/1.2841364. URL http://aip.scitation.org/doi/10.1063/1.2841364.

[105] Michael P. Marder. Density Functional Theory. In *Condensed Matter Physics*, chapter Electron-Electron Interactions. John Wiley & Sons, Inc., 2nd edition, 2010.

[106] Pierre Hohenberg and Walter Kohn. Inhomogeneous electron gas. *Physical Review B*, 7(5):1912–1919, nov 1973. ISSN 01631829. doi: 10.1103/PhysRevB.7.1912. URL https://link.aps.org/doi/10.1103/PhysRev.136.B864.

[107] W. Kohn and L. J. Sham. Self-consistent equations including exchange and correlation effects. *Physical Review*, 140(4A):A1133–A1138, nov 1965. ISSN 0031899X. doi: 10.1103/PhysRev.140.A1133. URL https://link.aps.org/doi/10.1103/PhysRev.140.A1133.

[108] Volker Eyert. The Full Hamiltonian. In *Electronic Structure of Crystalline Materials*, chapter Reduction of the ionic degrees of freedom, pages 5–7. Institut für Physik, Universität Augsburg, Augsburg, 2008.

[109] Richard M. Martin. *Electronic Structure*. Cambridge University Press, Cambridge, 2004. ISBN 9780511805769. doi: 10.1017/CBO9780511805769. URL http://ebooks.cambridge.org/ref/id/CBO9780511805769.

[110] Jorge. Kohanoff. *Electronic structure calculations for solids and molecules : theory and computational methods*. Cambridge University Press, 2006. ISBN 9780521815918. URL http://www.cambridge.org/ca/academic/subjects/physics/condensed-matter-physics-nanoscience-and-mesoscopic-physics/

electronic-structure-calculations-solids-and-molecules-theory-and-computational-met
format=HB{&}isbn=9780521815918.

[111] Volker Eyert. The Kohn–Sham equations. In *Electronic Structure of Crystalline Materials*, chapter Density Functional Theory. Institut für Physik, Universität Augsburg, Augsburg, 2008.

[112] José M Soler, Emilio Artacho, Julian D Gale, Alberto García, Javier Junquera, Pablo Ordejón, and Daniel Sánchez-Portal. The SIESTA method for *ab initio order-N* materials simulation. *Journal of Physics: Condensed Matter*, 14(11):2745–2779, mar 2002. doi: 10.1088/0953-8984/14/11/302. URL http://stacks.iop.org/0953-8984/14/i=11/a=302?key=crossref.8ed2406c09184bcd143191af26e9f492.

[113] Pablo Rivero, Víctor Manuel García-Suárez, David Pereñiguez, Kainen Utt, Yurong Yang, Laurent Bellaiche, Kyungwha Park, Jaime Ferrer, and Salvador Barraza-Lopez. Systematic pseudopotentials from reference eigenvalue sets for DFT calculations. *Computational Materials Science*, 98:372–389, feb 2015. ISSN 09270256. doi: 10.1016/j.commatsci.2014.11.026. URL http://linkinghub.elsevier.com/retrieve/pii/S0927025614007940.

[114] D. D. Johnson. Modified Broyden's method for accelerating convergence in self-consistent calculations. *Physical Review B*, 38(18):12807–12813, dec 1988. ISSN 0163-1829. doi: 10.1103/PhysRevB.38.12807. URL https://link.aps.org/doi/10.1103/PhysRevB.38.12807.

[115] Célia Fonseca Guerra, Jan-Willem Handgraaf, Evert Jan Baerends, and F. Matthias Bickelhaupt. Voronoi deformation density (VDD) charges: Assessment of the Mulliken, Bader, Hirshfeld, Weinhold, and VDD methods for charge analysis. *Journal of Computational Chemistry*, 25(2):189–210, jan 2004. ISSN 0192-8651. doi: 10.1002/jcc.10351. URL http://www.ncbi.nlm.nih.gov/pubmed/14648618http://doi.wiley.com/10.1002/jcc.10351.

[116] Javier Junquera, Morrel H Cohen, and Karin M Rabe. Nanoscale smoothing and the analysis of interfacial charge and dipolar densities. *Journal of Physics: Condensed Matter*, 19(21):213203, may 2007. ISSN 0953-8984. doi: 10.1088/0953-8984/19/21/213203. URL http://stacks.iop.org/0953-8984/19/i=21/a=213203?key=crossref.4e6d1089f46314f07771d0a4a2472a06.

[117] Javier Junquera, Magali Zimmer, Pablo Ordejón, and Philippe Ghosez. First-principles calculation of the band offset at $BaO/BaTiO_3$ and $SrO/SrTiO_3$ interfaces. *Physical*

Review B, 67(15):155327, apr 2003. ISSN 0163-1829. doi: 10.1103/PhysRevB.67.155327. URL https://link.aps.org/doi/10.1103/PhysRevB.67.155327.

[118] Ask Hjorth Larsen, Jens Jørgen Mortensen, Jakob Blomqvist, Ivano E Castelli, Rune Christensen, Marcin Dułak, Jesper Friis, Michael N Groves, Bjørk Hammer, Cory Hargus, Eric D Hermes, Paul C Jennings, Peter Bjerre Jensen, James Kermode, John R Kitchin, Esben Leonhard Kolsbjerg, Joseph Kubal, Kristen Kaasbjerg, Steen Lysgaard, Jón Bergmann Maronsson, Tristan Maxson, Thomas Olsen, Lars Pastewka, Andrew Peterson, Carsten Rostgaard, Jakob Schiøtz, Ole Schütt, Mikkel Strange, Kristian S Thygesen, Tejs Vegge, Lasse Vilhelmsen, Michael Walter, Zhenhua Zeng, and Karsten W Jacobsen. The atomic simulation environment—a Python library for working with atoms. *Journal of Physics: Condensed Matter*, 29(27):273002, jul 2017. ISSN 0953-8984. doi: 10.1088/1361-648X/aa680e. URL http://stacks.iop.org/0953-8984/29/i=27/a=273002?key=crossref.20f9751653d872507bf6c0cc5737032c.

[119] Raffaella Demichelis, Yves Noel, Philippe D'Arco, Michel Rerat, Claudio M. Zicovich-Wilson, and Roberto Dovesi. Properties of Carbon Nanotubes: An ab Initio Study Using Large Gaussian Basis Sets and Various DFT Functionals. *The Journal of Physical Chemistry C*, 115(18):8876–8885, may 2011. ISSN 1932-7447. doi: 10.1021/jp110704x. URL http://pubs.acs.org/doi/abs/10.1021/jp110704x.

[120] Sandra García-Gil, Alberto García, Nicolás Lorente, and Pablo Ordejón. Optimal strictly localized basis sets for noble metal surfaces. doi: 10.1103/PhysRevB.79.075441. URL https://journals.aps.org/prb/pdf/10.1103/PhysRevB.79.075441.

[121] Eva M. Fernández, José M. Soler, Ignacio L. Garzón, and Luis C. Balbás. Trends in the structure and bonding of noble metal clusters. *Physical Review B*, 70(16): 165403, oct 2004. ISSN 1098-0121. doi: 10.1103/PhysRevB.70.165403. URL https://link.aps.org/doi/10.1103/PhysRevB.70.165403.

[122] X. Gonze, F. Jollet, F. Abreu Araujo, D. Adams, B. Amadon, T. Applencourt, C. Audouze, J.-M. Beuken, J. Bieder, A. Bokhanchuk, E. Bousquet, F. Bruneval, D. Caliste, M. Côté, F. Dahm, F. Da Pieve, M. Delaveau, M. Di Gennaro, B. Dorado, C. Espejo, G. Geneste, L. Genovese, A. Gerossier, M. Giantomassi, Y. Gillet, D.R. Hamann, L. He, G. Jomard, J. Laflamme Janssen, S. Le Roux, A. Levitt, A. Lherbier, F. Liu, I. Lukačević, A. Martin, C. Martins, M.J.T. Oliveira, S. Poncé, Y. Pouillon, T. Rangel, G.-M. Rignanese, A.H. Romero, B. Rousseau, O. Rubel, A.A. Shukri, M. Stankovski, M. Torrent, M.J. Van Setten, B. Van Troeye, M.J. Verstraete, D. Waroquiers, J. Wiktor, B. Xu, A. Zhou, and J.W. Zwanziger. Recent

developments in the ABINIT software package. *Computer Physics Communications*, 205:106–131, aug 2016. ISSN 0010-4655. doi: 10.1016/J.CPC.2016.04.003. URL https://www.sciencedirect.com/science/article/pii/S0010465516300923.

[123] GGA Pseudopotential Database. URL https://departments.icmab.es/leem/siesta/Databases/Pseudopotentials/periodictable-gga-abinit.html.

[124] Gustavo E. Scuseria, Michael D. Miller, Frank Jensen, and Jan Geertsen. The dipole moment of carbon monoxide. *The Journal of Chemical Physics*, 94(10):6660–6663, may 1991. ISSN 0021-9606. doi: 10.1063/1.460293. URL http://aip.scitation.org/doi/10.1063/1.460293.

[125] Michael S. Strano, Stephen K. Doorn, Erik H. Haroz, Carter Kittrell, Robert H. Hauge, and Richard E. Smalley. Assignment of (n, m) Raman and optical features of metallic single-walled carbon nanotubes. *Nano Letters*, 3(8):1091–1096, 2003. ISSN 15306984. doi: 10.1021/nl034196n. URL https://pubs.acs.org/doi/10.1021/nl034196n.

[126] R. Bruce Weisman and Sergei M. Bachilo. Dependence of optical transition energies on structure for single-walled carbon nanotubes in aqueous suspension: An empirical Kataura plot. *Nano Letters*, 3(9):1235–1238, 2003. ISSN 15306984. doi: 10.1021/nl034428i. URL https://pubs.acs.org/doi/10.1021/nl034428i.

[127] C. N. Berglund and W. E. Spicer. Photoemission studies of copper and silver: Experiment. *Physical Review*, 136(4A):A1044–A1064, nov 1964. ISSN 0031899X. doi: 10.1103/PhysRev.136.A1044. URL https://link.aps.org/doi/10.1103/PhysRev.136.A1044.

[128] C. N. Berglund and W. E. Spicer. Photoemission Studies of Copper and Silver: Theory. *Physical Review*, 136(4A):A1030–A1044, nov 1964. ISSN 0031-899X. doi: 10.1103/PhysRev.136.A1030. URL https://link.aps.org/doi/10.1103/PhysRev.136.A1030.

[129] A. W. Dweydari and C. H. B. Mee. Work function measurements on (100) and (110) surfaces of silver. *Physica Status Solidi (a)*, 27(1):223–230, jan 1975. ISSN 00318965. doi: 10.1002/pssa.2210270126. URL http://doi.wiley.com/10.1002/pssa.2210270126.

[130] Chloé Archambault and Alain Rochefort. States Modulation in Graphene Nanoribbons through Metal Contacts. *ACS Nano*, 7(6):5414–5420, jun 2013. ISSN 1936-0851. doi: 10.1021/nn401357p. URL http://pubs.acs.org/doi/10.1021/nn401357p.

[131] Winfried Mönch. *Semiconductor Surfaces and Interfaces*, volume 26 of *Springer Series in Surface Sciences*. Springer Berlin Heidelberg, Berlin, Heidelberg, 1995. ISBN 978-3-540-58625-8. doi: 10.1007/978-3-662-03134-6. URL http://link.springer.com/10.1007/978-3-662-03134-6.

[132] Eric Jones, Travis Oliphant, Pearu Peterson, et al. SciPy: Open source scientific tools for Python, 2001–. URL https://docs.scipy.org/doc/scipy/reference/generated/scipy.optimize.leastsq.html#scipy.optimize.leastsq. [Online; accessed 18.02.2019].

[133] Eduard Llobet. Gas sensors using carbon nanomaterials: A review, 2013. ISSN 09254005.

[134] Elise Y Li and Nicola Marzari. Improving the Electrical Conductivity of Carbon Nanotube Networks: A First-Principles Study. 5(12):9726–9736, 2011. doi: 10.1021/nn2032227. URL www.acsnano.org.

APPENDIX A CHARGE DISTRIBUTION

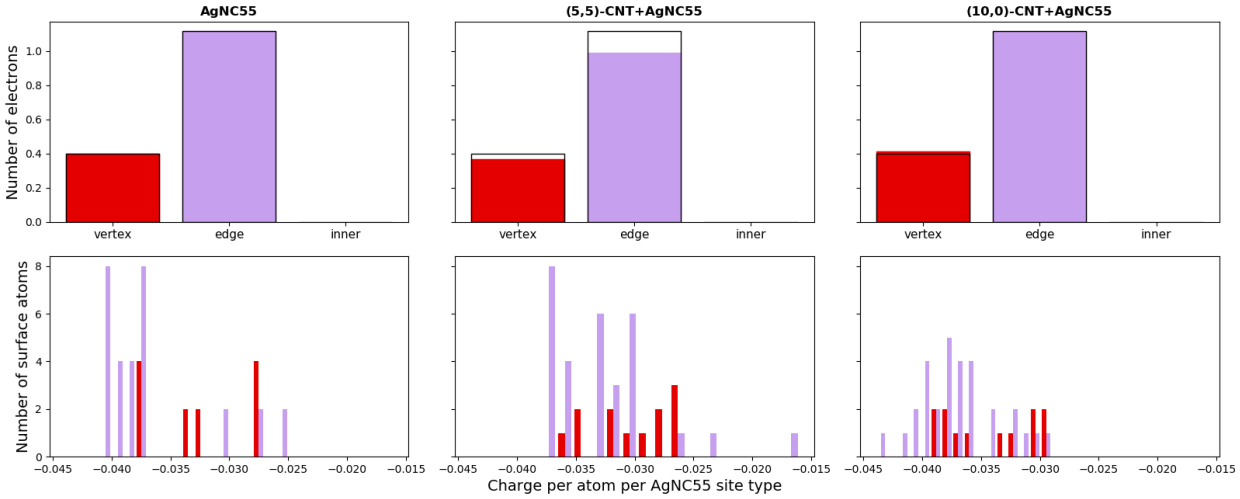

Figure A.1 Charge transfer populations of AgNC55

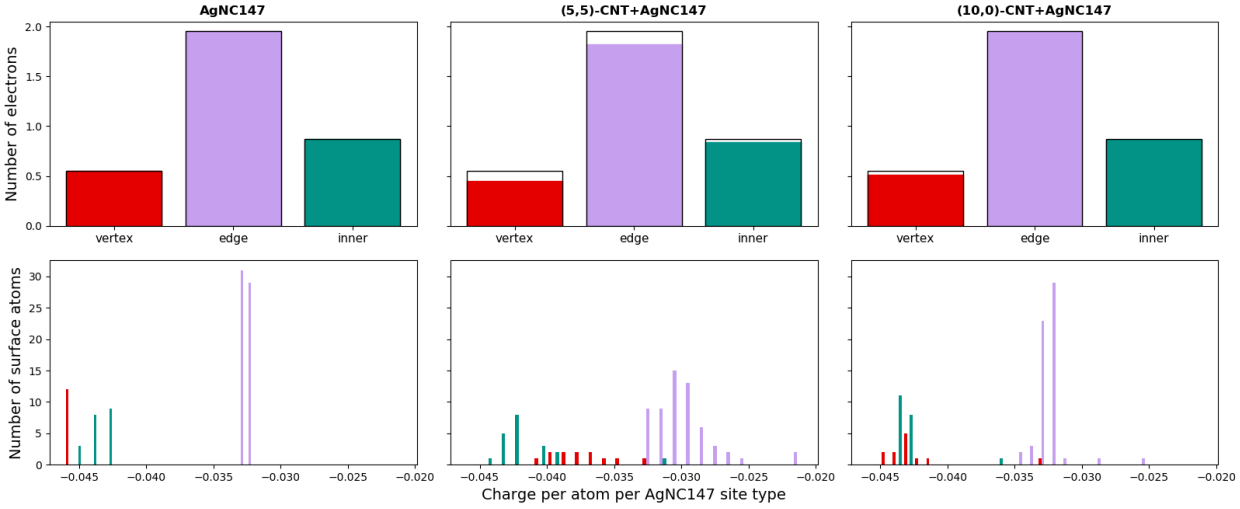

Figure A.2 Charge transfer populations of AgNC147

APPENDIX B ELECTROSTATICS

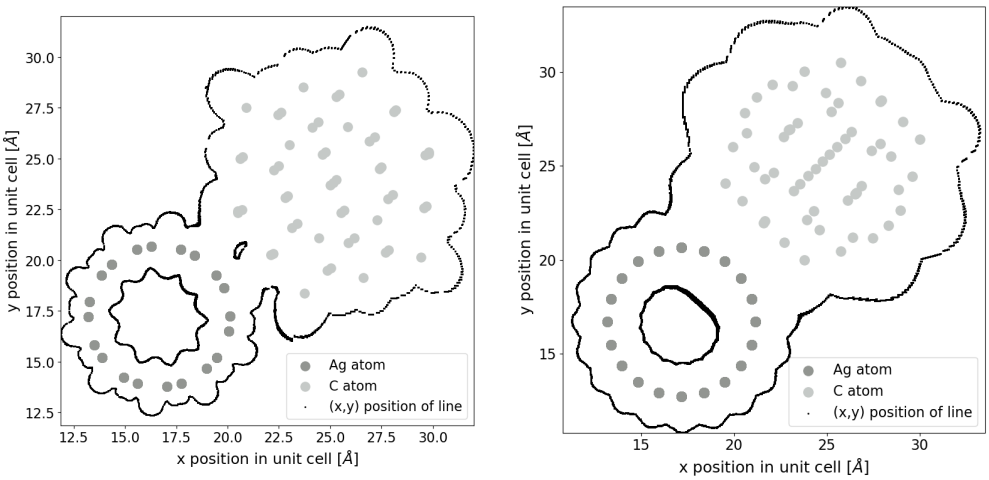

(a) (5,5)-CNT / AgNC55

(b) (10,0)-CNT / AgNC55

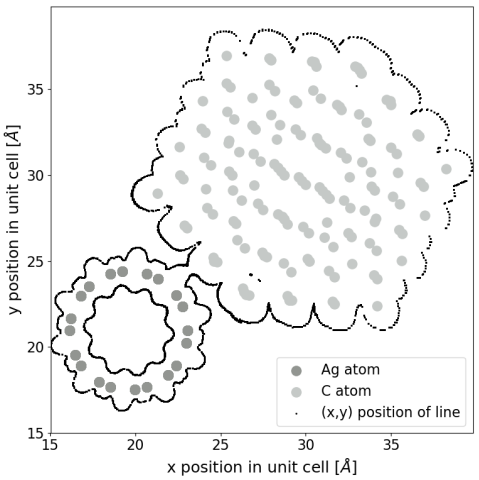

(c) (5,5)-CNT / AgNC147

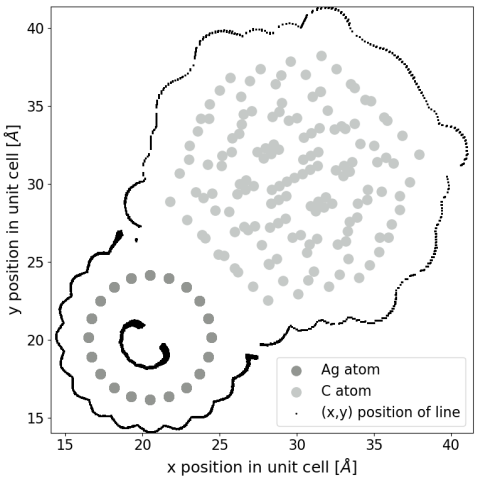

(d) (10,0)-CNT / AgNC147

Figure B.1 Profile of lines along the CNT-axis that fit whithin the band line-up picture